Technische Universität München
TUM School of Computation, Information and Technology

Printing Technologies for Implantable Neural Interfaces

Korkut Terkan

Vollständiger Abdruck der von der TUM School of Computation, Information and Technology der Technischen Universität München zur Erlangung eines

Doktors der Ingenieurwissenschaften

genehmigten Dissertation.

Vorsitz: Prof. Dr. rer. nat. Eva Weig

Prüfer der Dissertation:

1. Prof. Dr. rer. nat. Bernhard Wolfrum
2. Prof. Dr.-Ing. Werner Hemmert

Die Dissertation wurde am 13.02.2023 bei der Technischen Universität München eingereicht und durch die TUM School of Computation, Information and Technology am 05.07.2023 angenommen.

ZUSAMMENFASSUNG

Elektroden zum Koppeln implantierbarer Elektronik und neuronalem Gewebe spielen eine bedeutende Rolle beim Erlangen eines besseren Verständnisses über das Nervensystem und beim Helfen von Menschen, die aufgrund von Nervenläsionen oder verlorenen Organen an körperlich beeinträchtigten Funktionen leiden. Dabei sind insbesondere Neurostimulationstechniken für die bioelektronische Medizin auf die Entwicklung von mechanisch als auch elektrochemisch stabilen Elektroden angewiesen. Während die heutigen implantierbaren Elektroden meistens auf Metallen basieren, werden neue Materialien entworfen, um die mechanischen und elektrochemischen Eigenschaften von neuroelektronischen Schnittstellen zu verbessern. Des Weiteren beruht die Herstellung von metallischen Elektroden meist auf konventionelle Mikrofabrikationstechniken, welche Reinräume erfordern. Der Fortschritt in Druckverfahren allerdings hat das Rapid Prototyping neuer Elektrodenarraydesigns mit konventionellen als auch mit neuartigen Materialien ermöglicht.

In dieser Arbeit wurde die Herstellung weicher und dehnbarer Nervenschnittstellen mit mechanisch und elektrochemisch stabilen Elektroden mittels Druckverfahren untersucht. Das Tintenstahldruckverfahren wurde verwendet, um im ersten Ansatz Leiterbahnen und Elektroden aus Silvernanopartikeln direkt auf Silikonsubstraten aufzutragen und im zweiten Ansatz eine Wachsmaske auf eine Filtermembran aufzubringen, welche daraufhin zur selektiven Vakuumfiltration verwendet wurde. Das Muster, das nach der Filtration auf der Membran zurückblieb, bestand ausschließlich aus Kohlenstoffnanoröhrchen und wurde im nächsten Herstellungsschritt in einen Silikonträger eingebettet. Kohlenstoffnanoröhrchen wurden aufgrund ihrer im Vergleich zu herkömmlichen metallischen Elektroden überlegenen elektrochemischen Eigenschaften verwendet. Während der erste Ansatz bezüglich der Stabilität der Leiterbahnen und Elektroden verschiedene Schwierigkeiten darstellte, konnten mit dem zweiten Ansatz funktionsfähige Leiterbahnen und Elektroden hergestellt werden, welche die gewünschten mechanischen und elektrochemischen Stabilitätsanforderungen erfüllen konnten. Die Funktionalität der in Silikon eingebetteten Kohlenstoffnanoröhrchenelektroden wurde anhand von extrazellulärer Stimulation eines Nerven in einem Blutegel demonstriert. Mittels 3D-Druckverfahren

fabrizierter Formen wurden Silikonteile hergestellt, welche widerum dazu verwendet wurden um die Kohlenstoffnanoröhrchenelektroden herum einen manschettenartigen Schließmechanismus zu realisieren. Zusammenfassend wurde das Rapid Prototyping von implantierbaren periphären Nervenschnittstellen aus neuartigen und vielversprechenden Elektodenmaterialien mittels 2D- und 3D-Druckverfahren gezeigt.

ABSTRACT

Electrodes for interfacing implantable electronics and neural tissue are of great importance to gain a better understanding of the nervous system and to help people suffering from impaired body functions due to nerve lesions or lost organs. In particular, neurostimulation techniques for bioelectronic medicine rely on the development of mechanically and electrochemically stable electrodes. While contemporary implantable electrodes are based mainly on metals, new materials are being designed to enhance the mechanical and electrochemical properties of the neuroelectonic interface. Furthermore, the manufacturing of metallic electrodes is mainly based on conventional microfabrication techniques operating in cleanroom facilities. The advance in printing technologies, however, enabled the rapid prototyping of new electrode array designs with contemporary as well as novel materials.

In this work, the fabrication of soft and stretchable nerve interfaces with mechanically and electrochemically stable electrodes by using printing technologies was investigated. Inkjet printing was used in the first approach for direct deposition of Ag nanoparticle conductors and electrodes on silicone substrates and in the second approach for the deposition of a wax mask on a filter membrane which was then used for selective vacuum filtration. The pattern obtained on the membrane after filtration consisted of carbon nanotubes solely and was embedded into a silicone carrier in the next fabrication step. Carbon nanotubes were used due to their superior electrochemical properties compared to implantable metal electrodes. While the first approach posed several challenges in the stability of the conductors as well as the electrodes, the second approach yielded functional conductors and electrodes complying with the desired mechanical and electrochemical stability aspect. The functionality of the carbon nanotubes electrodes embedded into silicone was demonstrated by extracellular stimulation of a nerve in a horse leech. By using 3D printing, molds were fabricated into which silicone parts were prepared to realize a cuff closing mechanism around the carbon nanotubes electrodes. In conclusion, the rapid prototyping of implantable peripheral nerve interfaces made of an emerging and promising electrode material by using 2D and 3D printing methods was shown.

CONTENTS

LIST OF SYMBOLS

A	area in m^2
α	transfer coefficient used in describing the energy in transition states during redox reactions
α_H	specific filter resistance of the cake in vacuum filtration in m^{-2}
α_p	light adsorption coefficient of a resin in m^{-1}
β	filter resistance in vacuum filtration in m^{-1}
δ_N	Nernst diffusion layer
ϵ	permittivity of a solution in $\mathrm{C\,V^{-1}\,m^{-1}}$
ϵ_p	void fraction of the porous medium in vacuum filtration
ϵ_s	strain in $\%$
η	viscosity in $\mathrm{Pa\,s}$
η_o	overpotential in V
η_off	reached overpotential in V during a constant stimulation current when the current is turned off
θ_eq	contact angle in °, the angle between the liquid/gas and the liquid/solid interface lines
λ_D	Debye length in m
$\mu_{\mathrm{e^-,Me}}$	chemical potential of electrons in metal in $\mathrm{J\,mol^{-1}}$
$\mu^0_{\mathrm{e^-,Me}}$	concentration independent part of $\mu_{\mathrm{e^-,Me}}$
$\mu_{\mathrm{e^-,S}}$	chemical potential of electrons in solution in $\mathrm{J\,mol^{-1}}$
$\mu^0_{\mathrm{e^-,S}}$	concentration independent part of $\mu_{\mathrm{e^-,S}}$
ξ	distance from a point inside the solution to the outer Helmholtz layer in m
ρ	fluid density in $\mathrm{kg\,m^{-3}}$
ρ_E	local charge density in $\mathrm{C\,m^{-3}}$
ρ_out	resistivity of the extracellular medium in $\Omega\mathrm{m}$
ρ_in	resistivity of the intracellular medium in $\Omega\mathrm{m}$
σ	surface tension in $\mathrm{N\,m^{-1}}$

φ	potential of an electrode against a reference value in V
$\varphi(x)$	local potential inside the solution at a distance of x from the electrode surface in a 1-D case, unit in V
φ_0	equilibrium potential of an electrode against a reference value in V
φ_{00}	standard equilibrium potential of an electrode against a reference value in V
$\varphi_0^{\mathrm{Ag/Ag^+}}$	equilibrium potential of a silver ion electrode in V
$\varphi_{00}^{\mathrm{Ag/Ag^+}}$	standard equilibrium potential of a silver ion electrode in V
$\varphi_0^{\mathrm{Ag/AgCl/Cl^-}}$	equilibrium potential of a silver chloride electrode in V
$\varphi_{00}^{\mathrm{Ag/AgCl/Cl^-}}$	standard equilibrium potential of a silver chloride electrode in V
φ_{out}	extracellular potential in V
φ_{el}	electrical potential in the electrode in V
φ_{i}	equilibrium potential of ion i in V
φ_{in}	intracellular potential in V
φ_{Me}	electrical potential in the metal inV
φ_{m}	membrane potential in V
φ_{n}	reduced potential at node n in V
$\varphi_{\mathrm{o.H.}}$	electrical potential in the outer Helmholtz layer in V
φ_{r}	membrane resting potential in V
φ_{S}	electrical potential in solution in V
$\Delta\varphi$	potential difference measured between two electrodes in V
$\Delta\varphi_0$	galvani or equilibrium potential between an electrode and a solution in V
$\Delta\varphi_{00}$	standard equilibrium potential between an electrode and a solution in V
$\Delta\varphi_{\mathrm{el}}$	potential drop at the electrode in V, $\eta_{\mathrm{o}} + \Delta\varphi_0$
$\Delta\varphi_{\mathrm{diffusive}}$	electrical potential difference between the outer Helmholtz layer and the solution in V
$\Delta\varphi_{\mathrm{s}}$	potential drop across the solution resistance in V
$\Delta\varphi_{\mathrm{static}}$	electrical potential difference between the electrode and the outer Helmholtz layer in V
$\Delta\varphi_{\mathrm{tot}}$	overpotential + potential drop across the solution resistance in V
ψ	sum of the three energies determined by the surface tension times surface area at the three interfaces between solid, liquid, and gas for a drop of liquid on a solid surface, unit in J
ω	angular frequency in $\mathrm{rad\,s^{-1}}$
a	diameter of solvated ions in m
$a_{\mathrm{Ag^+}}$	activity of Ag^+ ions in solution
$a_{\mathrm{Cl^-}}$	activity of Cl^- ions in solution

$a_{\mathrm{e^-,Me}}$	activity of electrons in metal
$a_{\mathrm{e^-,S}}$	activity of electrons in solution
$a_{\mathrm{H_3O^+}}$	activity of protons in solution
a_{ox}	activity of the oxidized species
a_{red}	activity of the reduced species
$C_{\mathrm{diffusive}}$	diffusive double layer capacitance in F
C_{dl}	double layer capacitance in F
$C_{\mathrm{H.H.}}$	Helmholtz double layer capacitance F
C_{m}	membrane capacitance of a certain length of an axon in F
c_{i}	concentration of ion i in $\mathrm{mol\,m^{-3}}$
$c_{\mathrm{i,in}}$	concentration of ion i inside the cell in $\mathrm{mol\,m^{-3}}$
$c_{\mathrm{i,out}}$	concentration of ion i outside the cell in $\mathrm{mol\,m^{-3}}$
$c_{\mathrm{i},\infty}$	concentration of an ion inside the solution in $\mathrm{mol\,m^{-3}}$
c_{m}	specific membrane capacitance in $\mathrm{F\,m^{-2}}$
c_{ox}	concentration of oxidized species at the electrode surface in $\mathrm{mol\,m^{-3}}$
c_{red}	concentration of reduced species at the electrode surface in $\mathrm{mol\,m^{-3}}$
c_{s}	specific electrode capacitance in $\mathrm{F\,m^{-2}}$
c^0	ion concentration inside the solution in $\mathrm{mol\,m^{-3}}$
c^{s}	ion concentration at the electrode surface in $\mathrm{mol\,m^{-3}}$
D	diffusion coefficient in $\mathrm{m^2\,s^{-1}}$
D_{c}	critical dose of light during photopolymerization in $\mathrm{W\,s\,m^{-2}}$
D_{i}	diffusion coefficient of ion i in $\mathrm{m^2\,s^{-1}}$
d	light penetration depth during photopolymerization in m
d_{a}	axon diameter in m
d_{c}	characteristic length in m (typically the diameter of the nozzle or the drop in inkjet printing)
d_{p}	depth inside resin until where solidification has reached during photopolymerization in m
d_{S}	Sauter diameter describing the average diameter of the particle size distribution in vacuum filtration, unit in m
$\vec{E}$	electric field in $\mathrm{V\,m^{-1}}$
E_0	electromotive force in V
F	Faraday constant, $96\,485\,\mathrm{C\,mol^{-1}}$
f_{n}	activating function in $\mathrm{V\,m^{-2}}$
G_{a}	axonal conductance in S
G_{m}	ionic/membrane conductance in S

g_i	cell membrane's permeability to ion i in $\mathrm{S\,m^{-2}}$
h	cake thickness in vacuum filtration in m
h_a	characteristic polymerization depth for a resin in m
I	light intensity in $\mathrm{W\,m^{-2}}$
I_0	light intensity at the horizontal plane where the light hits the resin during photopolymerization, unit in $\mathrm{W\,m^{-2}}$
i	current in A
i_anod	anodic current flowing through an electrode in A
i_c	capacitive current flowing through an electrode in A
i_cath	cathodic current flowing through an electrode in A
i_f	Faradaic current flowing through an electrode in A
i_ionic	net ionic current flowing through the cell membrane in A
i_stim	constant stimulation current in A
i^+	oxidation current part of Faradaic current in A
i^-	reduction current part of Faradaic current in A
$\vec{J}_\mathrm{diff}$	diffusive flux in $\mathrm{mol\,m^{-2}\,s^{-1}}$
$\vec{J}_\mathrm{elec}$	electrophoretically inducec flux in $\mathrm{mol\,m^{-2}\,s^{-1}}$
j	current density in $\mathrm{A\,m^{-2}}$
j_0	exchange current density in $\mathrm{A\,m^{-2}}$
j_anod	anodic current density in $\mathrm{A\,m^{-2}}$
j_c	capacitive current density in $\mathrm{A\,m^{-2}}$
j_cath	cathodic current density in $\mathrm{A\,m^{-2}}$
j_i	current density of ion or leakage current density in $\mathrm{A\,m^{-2}}$
$j^+(\varphi_0)$	anodic exchange current density while the electrode is at its equilibrium potential, unit in $\mathrm{A\,m^{-2}}$
$j^-(\varphi_0)$	cathodic exchange current density while the electrode is at its equilibrium potential, unit in $\mathrm{A\,m^{-2}}$
K_a	equilibrium constant
$K_\mathrm{a}^\mathrm{AgCl}$	equilibrium constant of silver chloride while defining the equilibrium potential of a silver chloride electrode
k_0^+	heterogeneous oxidation rate constant in $\mathrm{m\,s^{-1}}$
k_0^-	heterogeneous reduction rate constant in $\mathrm{m\,s^{-1}}$
L	length of the active membrane part in m
m	slope of the middle section of the logarithmic impedance curve in the examplary electrochemical impedance spectroscopy graph
n	number of electrons transferred during a reaction

Oh	Ohnesorge number, dimensionless value to determine whether a liquid is printible or not in inkjet printing
P_i	permeability for an ion i in $\mathrm{m\,s^{-1}}$
p	pressure in $\mathrm{kg\,m^{-1}\,s^{-2}}$
Q	electrical charge in C
R	molar gas constant, $8.314\,\mathrm{J\,K^{-1}\,mol^{-1}}$
Re	Reynolds number, ratio between inertial and viscous forces in liquids
R_ct	charge transfer resistance in Ω
r	distance between an electrode and a compartment for which the extracellular potentials along an axon are computed, unit in m
S_ox	oxidized substance
S_red	reduced substance
$R_\mathrm{re-ce}$	solution resistance between reference electrode and counter electrode in Ω
R_s	solution resistance in Ω
$R_\mathrm{re-ce}$	solution resistance between working electrode and reference electrode in Ω
T	thermodynamic temperature in K
T_f	fundamental period of an ink chamber in an piezoelectric transducer in s
t_c	critical exposure time during photopolymerization for I_0 to reach the polymerization of the resin at $d = 0$, unit in s
t_p	light exposure time during photopolymerization for I_0 to reach the polymerization of the resin until a depth d_p, unit in s
t_*	durations of different sections of a biphasic jetting pulse in inkjet printing, unit in s where * stands for either dQ, fQ, fR, rQ, rR, wQ, or wR
v	velocity in $\mathrm{m\,s^{-1}}$
$\dot{v}$	volumetric flow rate in $\mathrm{m^3\,s^{-1}}$
v_s	scan rate in cyclic voltammetry measurement, unit in $\mathrm{V\,s^{-1}}$
We	Weber number, the ration between inertia and surface tension
x	distance to the electrode surface in m
Δx	distance between two adjacent nodes at which the potentials along an unmyelinated axon are computed, for myelinated axons, it is the pitch between two adjacent nodes of Ranvier, unit in m
Z	overall impedance in Ω, $R_\mathrm{s} + Z_\mathrm{el}$
$Z_\mathrm{C_{dl}}$	impedance of the double layer capacitance in Ω
Z_el	electrode impedance in Ω
Z_W	Warburg impedance in Ω
z	charge number of ions

CHAPTER 1

INTRODUCTION

In the beginning of the 20th century, Santiago Ramón y Cajal discovered that the neuron is the smallest information processing unit in our nervous system [1]. Since then, many scientists put a lot of effort to better understand the working principles of neurons and the way how they interact [2–6]. They did this by placing electrodes inside or outside, in the vicinity of neurons $in\ vivo$, or by placing slices of rodent brains or by growing neuronal clusters on electrode arrays to record their electrical activity or to stimulate them $in\ vitro$ [7–20]. Electrical interfacing with neurons served not only research purposes, but also for treatment of chronic pain [21], several neuronal and other physiologic diseases [22–24] and the more advanced the technology of implantable electronics and electrodes became to the development of neuroprosthetic devices [25]. With the latter, the aim is to the restore the functionality of lost sensory organs [26, 27], regain control of limbs and other organs for paralyzed people [28–30] or provide control over electromechanic actuators replacing lost body parts of amputees [31].

In order to electrically interface neurons in the central nervous system or axons in the peripheral nervous system, various nerve interface designs were developed. Electrode leads which can be implanted deep into the brain [32] or electrode arrays which can be positioned onto the cortex [33] are available for recording and stimulating neurons in the brain. For gaining electrical access to axons in peripheral nerves, several interfacing strategies were demonstrated with all having a different degree of invasiveness. Cuff electrodes can be wrapped around nerves and can record from or stimulate axons inside different fascicles only from the surface of the nerve [34–36]. A variant of cuff electrodes is the flat interface nerve electrode which reshapes a peripheral nerve into its flat cross-section [37]. Thereby, the electrodes can achieve better access to the fascicles inside the nerve which are then aligned next to each other instead of being bundled in a circular fashion. Another type of nerve interfaces are penetrating electrode arrays. The longitudinal intrafascicular nerve interface is implanted parallel to the axons inside the nerve and

its electrodes are aligned along the length of the nerve [38, 39]. The transverse intrafascicular nerve interface is implanted orthogonally to the length of the axons and its electrodes are aligned transverse to the length of the nerve [39–41]. A third variant of peripheral nerve interfaces are sieve electrodes [42, 43] and renegerative microchannel electrode arrays [44, 45]. In these two approaches, the nerve is severed and sutured to the interface so that the axons can grow through the holes of the sieve or the microchannels. However, a reliable regeneration remains an issue to be solved. While the degree of spatial selectivity increases in the order the interface variants are mentioned, so does their invasiveness and thereby the traumatic reaction they induce in the tissue during implantation.

For providing a high degree of control for neuroprosthetic devices, a high spatial selectivity between the electrodes of the nerve interface and the neurons in the brain or the axons in peripheral nerves is of importance. Therefore, the electrodes are designed as close as possible to each other which brings the necessity of fabricating small electrodes. This, however, brings the drawback of having electrodes with high impedance, making electrical nerve signal recording and simulation more difficult. To cope with this, various surface modifications to increase the desired electrochemical properties of electrodes are demonstrated. Electrodes made out of platinum or other biocompatible metals are coated with platinum-iridium [46], conducting polymers like poly(3,4-ethylenedioxythiophene) [47] and carbon nanotubes (CNTs) [48]. Other strategies are inducing porosity by nanostructured platinum [49] or oxide layer formations [50]. These surface alterations lower the electrode impedance and achieve higher capacities of the electrodes to inject charge. Consequently, higher signal-to-noise ratios can be obtained during recording and higher currents can be injected into the tissue through the electrode without reaching potentials at the electrode-electrolyte interface that might cause damage to the tissue or the electrodes by irreversible Faradaic reactions [51, 52].

Another important aspect for nerve interfaces is that the substrate of the nerve interface should have similar mechanical properties as the tissue to which it is in contact. Soft and flexible interfaces conform better to neural tissue [53] and elicit less neuronal damage during relative movements inside the body. In particular, such soft interfaces initiate less foreign body response compared to more rigid ones when implanted [54]. This aspect is of special importance as an inflammatory response can lead to fibrous capsule formation around the electrode, which in turn decreases the signal-to-noise ratio for recording devices or induces higher current thresholds to reach the target tissue when stimulating. Two main routes of providing flexible neural interfaces are currently being employed: One is based on the fabrication on extremely thin substrate films made, for example, of polyimide [40, 36] or parylene [55, 45]. The second approach employs soft and stretchable substrates made of, e.g., silicones such as polydimethylsiloxane (PDMS) [56–58]. While the integration of metallic conductors on flexible substrates is not a problem

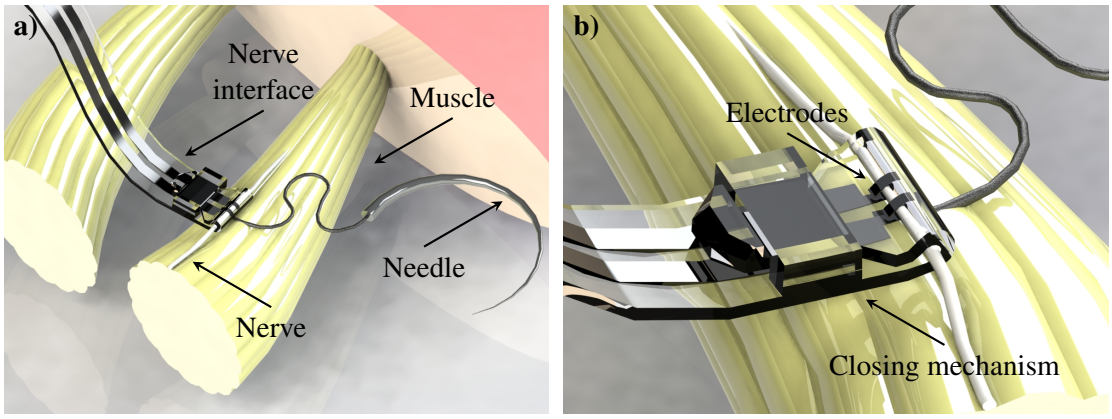

Figure 1.1: Schematic illustation of a cuff closing mechanism for interfacing electrodes with a peripheral nerve. **a)** The cuff is wrapped around the nerve innervating a muscle inside a limb of an animal. The needle is used to pull the electrodes through the nerve and the muscle. **b)** The electrodes are located on the inner surface of the part which is wrapped around the nerve.

in general, it turns out to be a challenge on soft and stretchable substrates due to the potential electrical connection breakage upon strain application. However, by structuring the electrical connections in a meandering fashion [59], patterning intrinsically stretchable polymeric composites [60], or making use of microcracks in thin metal films [61], elastomeric substrates can be stretched up to tens of percent while sustaining sufficient electrical conductivity. These conductors are manufactured mainly using photolithographic microfabrication techniques in cleanroom facilities which is not ideal for rapid prototyping due to the associated high cost of masks and devices. Furthermore, photolithographic fabrication methods produce a lot of waste material during etching processes which is an aspect to be considered with regard to environmental pollution. Inkjet printing presents an alternative manufacturing method for the rapid prototyping of new electrode array designs. By providing the possibility to directly print a large variety of conductive and dielectric materials on substrates, the above mentioned issues can be circumvented [57, 62–66].

A further approach to realize soft and stretchable neural interfaces is embedding high-aspect ratio nanomaterials, e.g. gold-coated titanium oxide nanowires, inside the PDMS matrix [67]. As another material with a high-aspect ratio, CNTs have been succesfully embedded in PDMS [68–72]. Typically, electrodes made out of CNTs exhibit a large specific surface area and, therefore, a high specific double layer capacitance when used in contact with electrolyte solutions [73]. This property in combination with their wider water window compared to metal electrodes, enables CNTs to store more charge [51, 74], making them a promising candidate for stimulation electrodes.

In this work, two rapid prototyping approaches to fabricate soft and stretchable peripheral

nerve stimulation electrodes were investigated. The first strategy tested inkjet printing to realize conductors with a Ag nanoparticle ink on an elastomeric substrate. To render the electrodes biocompatible and mechanically stable, surface coatings such as Au deposition or a CNT comprising silicone composite were tested. The challenges faced with this manufacturing method are presented. The second strategy was to use CNTs as the sole conducting material inside a PDMS matrix. The CNT conductors were structured using a printed wax pattern on a filter membrane for pattern-assisted vacuum filtration, as introduced by Tybrand and Vörös for the fabrication of silver nanowire conductors [75]. Afterward, the CNT pattern was embedded into a PDMS body. The CNT/PDMS electrodes' electrochemical and mechanical stability was evaluated and their functionality was validated by extracellular stimulation inside a horse leech (Haemopis sanguisuga). The stimulation was performed between two adjacent ganglia on its main ventral nerve cord, and its muscle contraction was correlated with the applied stimulation signals. Finally, a further rapid prototyping method based on 3D printed molds was demonstrated. Silicone parts, fabricated by these molds, were bonded onto the silicone body of the electrode array to realize a cuff mechanism around the electrodes for a stable interfacing with peripheral nerves similar as illustrated in Figure 1.1.

CHAPTER 2

FUNDAMENTALS

The present chapter first describes the working principles of the methods with which the soft interfaces were fabricated. Among those inkjet printing, stereolithography and wax pattern-assisted vacuum filtration will be explained. Next, the electrochemical theories will be given to understand the physical and electrical relations between an electrode and a conducting liquid medium. This is followed by electrophysiology to explain the electricity in an electrogenic cell and its interaction with an electrode. In the end, a short overview of emerging electrode materials is given.

2.1 FABRICATION METHOD I: INKJET PRINTING

The concept of inkjet printing refers to the ejection of droplets from a nozzle and their subsequent deposition on a surface to yield a desired pattern or structure. The printed pattern can be formed by depositing the droplets in different ways such as square or hexagonal lattices. By adjusting the center-to-center distance of adjacent droplets, the amount of material per unit area can be determined. This distance for subsequently jetted droplets within one line is defined by the ejection frequency and the driving velocity of the printhead. The width of a "single-splat line" depends on this drop spacing and on the wetting properties between the ink and the printed surface. By printing several consecutive such lines next to each other a certain pattern can be printed. Figure 2.1 shows an example of how single droplets are deposited and thereby form a layer.

There are two different main technologies in inkjet printing, which are "continuous inkjet" (CIJ) and "drop on demand" (DoD) printing. In CIJ a continuous flow of droplets is generated. Using, for instance, electrostatic forces, these droplets are then either directed onto the substrate or into a so-called gutter. In contrast to this, DoD printing only ejects droplets when they are

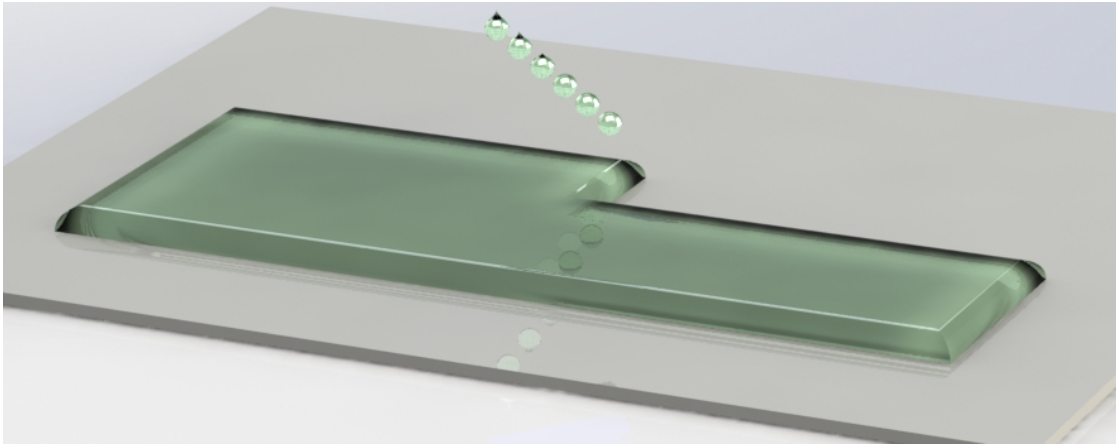

Figure 2.1: Lines are deposited by consecutive droplets and layers are formed by consecutive lines.

needed. For the ejection of droplets in DoD inkjet printing, there are mainly two techniques utilized. One of them is called "thermal inkjet" (TIJ), in which the ink in the reservoir is heated up rapidly over its boiling point and the thereby generated pressure wave forces the ink through the nozzle. Since it is not desirable for every ink to be heated up to its boiling point, the usage of this technique is limited. In "piezoelectric DoD" on the other hand, this pressure wave is generated by a piezoelectric transducer. The application of an electrical pulse to this transducer leads to a deformation of the chamber walls and thereby generates the necessary pressure wave. The latter technique is employed in the printer which was used throughout this work. In Figure 2.2 the schematic of a voltage driven piezoelectric transducer is depicted.

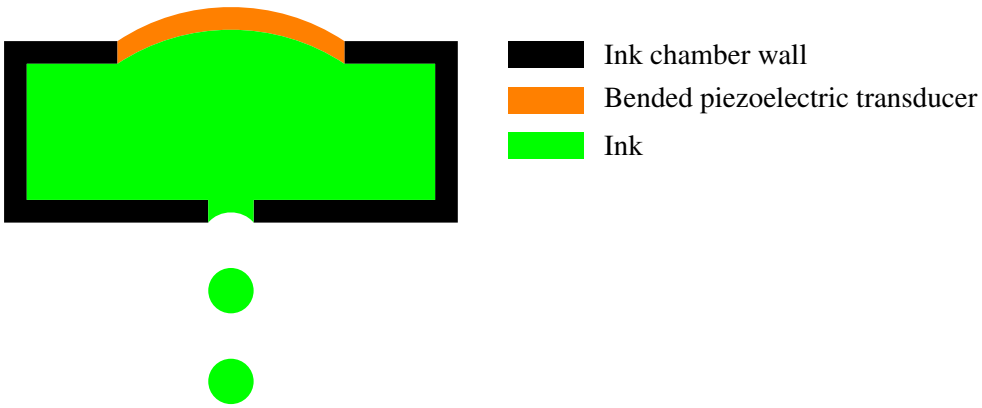

Figure 2.2: Schematic of a piezoelectric DoD inkjet printing. The application of an electrical pulse leads to deformation of the piezoelectric transducer. The bended transducer induces a pressure wave into the ink which is thereupon forced out of the nozzle.

In the following, the basic underlying principles of inkjet printing are given starting from the ink ejection until how to render the ink functional on the deposited surface as described in recent literature on this topic [76].

2.1.1 DROPLET EJECTION

Upon applying a pressure on the ink chamber, a certain amount of liquid is pushed out of the nozzle. This amount is at the beginning still connected to the ink in the ink channel through a tail as can be seen in Figure 2.3 a. At some point this tail detaches from the ink in the reservoir and flows together with the droplet head towards the substrate. During the flight, the tail shortens and either coalesces with the head or breaks off. The former scenario happens when the ink in the tail is faster than the ink in the head, while the latter scenario happens when this is vice versa. If the tail breaks off, it forms a second and smaller droplet, a so-called "satellite". This is an undesired phenomenon since it yields to an extra droplet on the surface which can corrupt the printed pattern. Whether satellites are generated or not depends on how the droplet is ejected and on the physical properties of the liquid such as its temperature, surface tension or viscosity. In Figure 2.3, well ejected droplets from three adjacent nozzles are depicted and how their tails coalesce with their heads with advancing time.

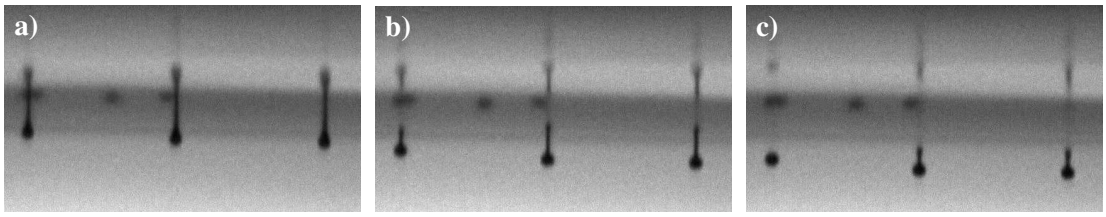

Figure 2.3: Droplet formation with advancing time. Droplets are ejected out of three adjacent nozzles which have a spacing of $254\,\mu\mathrm{m}$. **a)**: $4\,\mu$s after ejection. **b)**: $13\,\mu$s after ejection. **c)**: $19\,\mu$s after ejection. Images are from the printer used in this work.

2.1.2 WAVEFORM FOR DRIVING THE PIEZOELECTRIC TRANSDUCER

In a DoD piezoelectric inkjet printhead, a voltage waveform is required which is applied at the piezoelectric transducer to propel the fluid out of the ink channel. A well-developed waveform is of substantial importance for a good and consistent droplet ejection. During the waveform development, attention must be paid on a physical phenomenon called "residual oscillations" in the ink chamber.

When the piezoelectric transducer is actuated, a pressure wave is induced into the liquid. This pressure forces a little amount of liquid to be ejected out of the nozzle, forming the droplet. Yet, the induced pressure wave still runs through the ink chamber, attenuates and terminates after some time. If the next droplet is ejected before these residual oscillations have entirely decayed, they affect the behavior of the subsequent droplet such that variations in ejection velocity and volume compared to the previous drop can occur. There is also the interference of neighboring ink chambers affecting each others droplet ejection. However, this is less significant compared to the residual oscillations between subsequent droplets within one channel. One solution would be to wait until the liquid within the ink chamber has reached its steady state. However, in this case the jetting frequency has to be decreased, which in turn would increase the printing time. Another solution is to tune the driving waveform such that it damps the residual oscillations and thereby increases the drop consistency.

Two different waveforms are introduced here with which the residual oscillations can be dampen out. One of them is the unipolar waveform and the other is the bipolar waveform, depicted in Figure 2.4. The first trapezoidal pulse seen in both waveforms is the jetting pulse which ejects the droplet and causes the residual oscillations. The second pulse is the quenching pulse which damps them. The unipolar waveform is easier to realize with regard to the driving electronics, while with the bipolar waveform higher jetting frequencies can be achieved, since the residual oscillations can be damped earlier.

One approach to determine the optimal waveform parameters is to conduct numerical analysis when the geometry of the ink chamber and the piezoelectric transducer is known. If this is not the case, experiments can be performed and the waveform can be tuned iteratively. In order to have a waveform to start with, the fundamental period T_f ($1/T_\mathrm{f}$ is the frequency of the ink chamber's fundamental resonance mode) of the ink chamber has to be determined. An empirical way of finding this value is to adjust the dwell time of the jetting pulse, which is approximately $T_\mathrm{f}/2$ when the droplet velocity has reached its maximum. When the fundamental period is known, the waveform parameters in Figure 2.4 can be defined with following equations:

$$t_\mathrm{rR} = t_\mathrm{fR} = t_\mathrm{rQ} = t_\mathrm{fQ} = \frac{T_\mathrm{f}}{8} \tag{2.1}$$

$$t_\mathrm{wR} = t_\mathrm{wQ} = \frac{T_\mathrm{f}}{2} - (t_\mathrm{rR} + t_\mathrm{fR}) \tag{2.2}$$

$$t_\mathrm{dQ} = \frac{T_\mathrm{f}}{2} \text{ for bipolar waveform, } t_\mathrm{dQ} = T_\mathrm{f} \text{ for unipolar waveform} \tag{2.3}$$

The velocity of the ejected droplets is proportional to the amplitude of the jetting pulse V_R and the damping of the ink channel depends on the amplitude of the quenching pulse V_Q. All these parameters can later slightly be altered to adjust the droplet velocity or volume. In general,

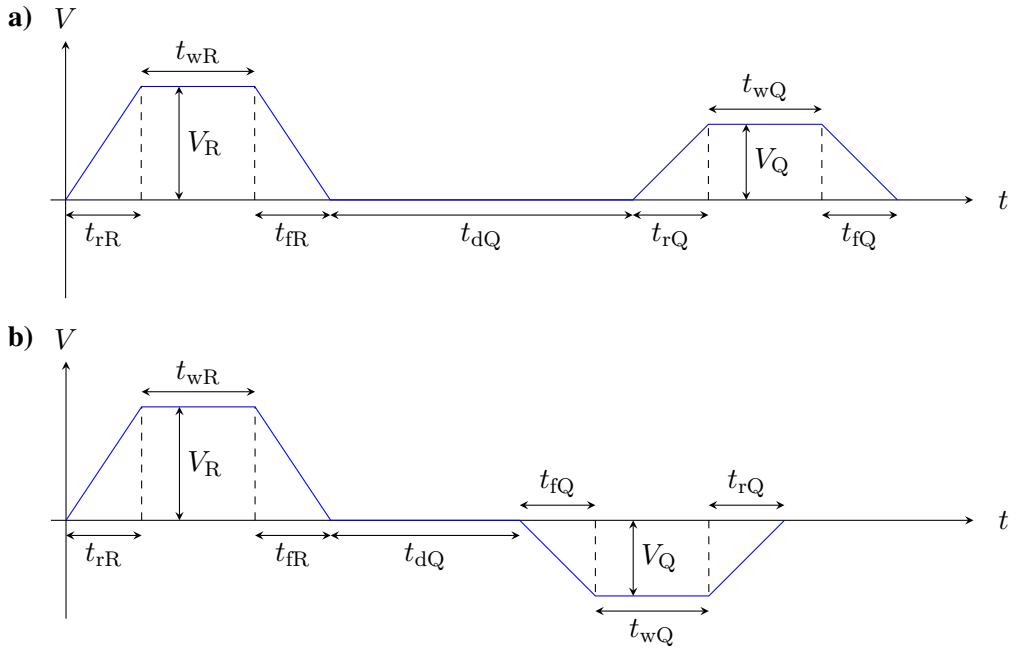

Figure 2.4: Parameters for jetting (first) pulse and quenching (second) pulse. **a)** Unipolar waveform. **b)** Bipolar waveform. Adapted from [76].

droplets can be ejected reliably with this approach and undesired effects such as a long tail breaking off the head droplet and causing satellites can be avoided.

2.1.3 PHYSICAL PARAMETERS AFFECTING THE FLUID BEHAVIOR

In order to be able to eject droplets out of a nozzle at all, several physical properties of the used liquid need to be within the right ranges. These properties can be listed as the surface tension, the velocity and the viscosity.

Surface tension is built up at the interface between two immiscible fluids. At this interface, an asymmetric attractive force comprising cohesion and adhesion acts on the molecules. Cohesion is an intermolecular force between the same molecules of a liquid, holding the liquid together. Whereas adhesion is a force between unlike molecules, enabling a liquid to stick to another body. The molecules inside the liquid volume surrounded by molecules of the same kind are in a lower energy state than the ones at the interface. In order to minimize its energy state the liquid tries to have as less molecules as possible at the interface, thus keeping its surface area as small as possible. This puts the surface of the liquid under tension whose direction is parallel to the interface.

Viscosity is the resistance of a fluid to shear deformation. When adjacent layers of a fluid are in relative motion as they slide past one another friction occurs between them. This resistance is caused due to the cohesive intermolecular force in that fluid. If the ratio of shear stress and shear deformation is constant, the fluid is referred to as a "Newtonian fluid". However, when the relationship between the shear stress and shear deformation is not linear, i.e. the liquid does not have a constant viscosity, it is referred to as "non-Newtonian fluid".

The surface tension, as well as the viscosity of a liquid depend on temperature. With increasing temperature, the molecules of the liquid become more energetic and the intermolecular cohesive force decreases. Therefore, the viscosity and the surface tension decrease as well, whereas the decrease in surface tension is comparatively slight.

Having explained these important properties of liquids, the so-called "Reynolds number" Re and the "Weber number" We, which are both dimensionless numbers, can be defined as follows.

$$Re = \frac{\rho v d_\mathrm{c}}{\eta} \quad \text{and} \quad We = \frac{\rho v^2 d_\mathrm{c}}{\sigma} \tag{2.4}$$

Here, ρ is the fluid density in $\mathrm{kg\,m^{-3}}$, v is the velocity of the fluid in $\mathrm{m\,s^{-1}}$, η is its viscosity in $\mathrm{Pa\,s}$, σ is the surface tension in $\mathrm{N\,m^{-1}}$ and d_c is the characteristic length in m, which is typically the diameter of the jet, nozzle, or drop. The Reynolds number is the ratio between inertial and viscous forces, while the Weber number represents the ratio between inertia and surface tension.

Out of these two important quantities, which give essential information about the fluid behavior, another number can be defined, namely the "Ohnesorge number" Oh.

$$Oh = \frac{\sqrt{We}}{Re} = \frac{\eta}{\sqrt{\sigma \rho d_\mathrm{c}}} \tag{2.5}$$

This is the value used in inkjet printing to determine whether a liquid is printable or not. To this end, the Ohnesorge number needs to be a value in the range of 0.1–1 . If the Ohnesorge number is >1, viscous forces will dominate and the droplet will not be able to separate from the ink in the ink chamber. When its value is <0.1, satellites will be generated during ejection. There might be no information about the velocity of the fluid included in the Ohnesorge number directly. However, it must be considered that the liquid must exhibit a certain kinetic energy which is sufficiently high such that the ink can be ejected out of the nozzle at all. In Figure 2.5 the ranges are given, in which fluids can be printed reliably.

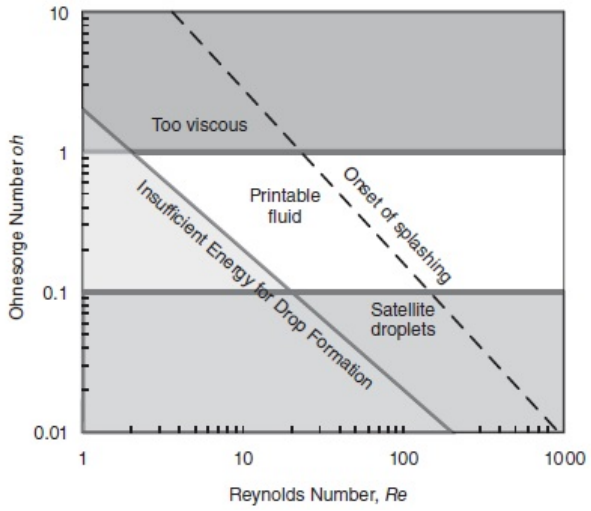

Figure 2.5: Graph showing the behavior of inks, in terms of the Ohnesorge and the Reynolds number. Adopted from [76].

2.1.4 DROPLET BEHAVIOR ON SURFACES

Once a droplet is ejected towards a surface, the behavior of this droplet on the surface is of interest. Due to this translational movement of the printhead, the droplets do not only have a velocity component in vertical direction, but also in horizontal direction, so that their flight is along a curve. This additional horizontal velocity component might lead to splashing in one direction upon impact, which is an undesired phenomenon. Whether this happens or not is a question of the physical properties of the ink in terms of the Ohnesorge and the Reynolds number. It can be determined by looking at the operation regime of printable inks which is depicted in Figure 2.5.

The next important aspect is the steady-state of the droplet on the surface and here, the term "contact angle" (θ_{eq}) plays a crucial role. It is defined as the angle between the liquid/gas and the liquid/solid interface lines, when a droplet has taken its steady-state shape on a surface as depicted in Figure 2.6. In this shape, the Gibbs free energy of the system is minimized by minimizing the sum (ψ) of the three energies contributed by the three interfaces liquid-gas(LG), solid-gas(SG) and liquid-solid(LS).

$$\psi = \sigma_{\mathrm{LG}} A_{\mathrm{LG}} + \sigma_{\mathrm{SG}} A_{\mathrm{SG}} + \sigma_{\mathrm{LS}} A_{\mathrm{LS}} \tag{2.6}$$

In the equation above, σ_{i} is the surface tension and A_{i} is the area at the interfaces. Minimizing

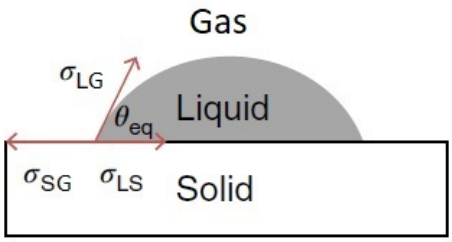

Figure 2.6: A liquid drop on a solid surface with an ideal contact angle. Adapted from [76].

this equation, yields the so-called Young's equation:

$$cos(\theta_{\mathrm{eq}}) = \frac{\sigma_{\mathrm{SG}} - \sigma_{\mathrm{LS}}}{\sigma_{\mathrm{LG}}} \tag{2.7}$$

The contact angle is strongly affected by the adhesive forces between the molecules of the liquid and the molecules of the surface, and by the cohesive intermolecular forces of the liquid. When the adhesive force dominates, the liquid will be pulled onto the surface, resulting in a smaller contact angle and a larger drop diameter. This is also referred as a better wetting. If the cohesive force dominates, the liquid will show a bad wetting behavior with a greater contact angle. It will "bead up" on the surface, which is an undesired condition. With this behavior, single droplets tend to coalesce into bigger droplets, forming inhomogeneously distributed islands on the surface and leaving gaps in the pattern. A smaller contact angle and thereby a better wetting is always preferable such that a well-coalesced pattern can be generated. In general this can be obtained when the surface tension of the solid is higher than the surface tension of the liquid. The wetting behavior can be increased by several techniques such as exposing the surface to O_2 plasma or UV light or by corona treatment.

Another important aspect is the drying of the printed structure on top of the surface. Since it is usually desired to obtain a consistent amount of ink per unit area, a homogeneous drying of the deposited layer must be ensured. Most of the times, the functional material is dissolved or suspended in a carrier liquid, which evaporates after deposition. Depending on where the solvent starts to evaporate and how fast this happens, the drying inevitably results in an either homogeneous or inhomogeneous surface. For instance, due to a higher surface area to volume ratio at the edges, the solvent in the ink evaporates faster at the edges than in the center of any deposited structure. This induces a capillary flow (self-driven flow caused by intermolecular forces between the solid and the liquid) such that the liquid at the center and the particles dispersed in it are attracted towards the edges of the structure, resulting in a pattern which is referred to as

the "coffee-ring effect". The prerequisite for a coffee-ring effect is a pinned contact line, i.e. the edges of a printed structure have to stop sliding across the solid surface.

The evaporation gradient at the surface leads to a surface tension gradient, with the surface tension at the edges being higher than that in the center. Since the area with a higher surface tension pulls more strongly on the surrounding liquid, an internal recirculating flow along the liquid/vapor interface from the center towards the edges occurs which is one type of a so-called "Marangoni flow" (solutal flow, the other type is thermal flow caused by temperature gradients inside the liquid). An inhomogeneous material deposition caused by these effects can have essential disadvantages for the fabrication of for example printed electronics.

Several attempts were reported on how to control this evaporation gradient [77, 78]. Surfactants can be added to enhance surface gradients and thereby the Marangoni flow. In the case that this flow is strong enough, it can counteract the coffee-ring effect and redistribute the ink in the layer. Another approach is to add solvents with lower or higher boiling points to the ink in such that the drying time can be decreased or increased. It was shown that by adding a solvent with a lower boiling point the evaporation gradient and the drying time can be reduced [77]. A further important parameter that affects the drying time is the substrate temperature. With a higher temperature, the drying time can be reduced as well. However, higher temperatures can also enhance outwards convective flow inside the printed layer. Thus an optimized set of parameters needs to be determined in order to obtain a homogeneous layer.

2.1.5 POST-PROCESSING OF THE DEPOSITED MATERIALS

Once a functional ink is deposited, it is not ready to provide its functionality without further processing. In some cases post-processing is also necessary such that a subsequent layer can be printed on top. The post-processing step explained in the following is with regard to the silver nanoparticle ink used in this work.

For printing the conductive tracks, a silver nanoparticle dispersion was used. The nanoparticles are coated with a stabilizing agent and suspended in a carrier liquid. This stabilizing agent prevents the nanoparticles to coagulate into greater particles and thereby clog the nozzles. The carrier liquid provides the ink with an optimal density, viscosity and surface tension such it can be reliably printed. After deposition of the ink, the carrier liquid has to evaporate entirely. Therefore, the printed structure is heated with a certain temperature for a certain duration. In order to reduce the fabrication time as well, the print can be performed directly on a heated surface. However, after the deposited structure has dried, the stabilizing agent is still around the nanoparticles. In this condition the silver particles are not close enough to each other to carry

electrons. In order to provide good conductivity of the structure, these stabilizing shells need to be broken up and the particles have to merge. This can be done for example by heating the structure up to a certain temperature or by exposing the silver pattern to high energy loaded photons. This process is called "sintering". After having applied a certain dose of energy the conductivity cannot be increased further unless very high temperatures (several hundred °C) are used. Most sintering conditions for inks are adapted to the polymer substrates used in printing applications.

2.2 FABRICATION METHOD II: STEREOLITHOGRAPHIC 3D PRINTING

This technique was used in this thesis to fabricate various structures which were used for molding silicone and establishing electrical connections. In the following the working principles of stereolithographic printing, the dynamic photomask generation and the principes of photopolymerization will be explained as described in [79].

2.2.1 BASIC WORKING PRINCIPLES

In this technique, a three dimensional computer aided design (CAD) file is sliced into layers of equal height by a software which are then subsequently fed to the printer during the printing process. The three dimensional object is generated by the subsequent photopolymerization of two dimensional layers inside a precursor solution.

Stereolithographic 3D printers comprise a resin tank with a UV-curable resin, a light source and a moving stage. The printing process is slightly different for the two approaches available. In one of them, the so-called free surface approach (Figure 2.7 a), the moving stage resides directly below the surface of the resin in the beginning. The light source, a laser beam, illuminates the pattern of the first layer into the resin on top of the moving stage. The illumination is performed by scanning the pattern in subsequent rows at a certain velocity. When the scan is finished the stage moves down by the height of the layer and the pattern of the next layer is illuminated into the resin on top of the first layer. This continues until the last layer is illuminated and the print has finished. In the other, the so-called constrained surface approach (Figure 2.7 b), the stage resides directly above the bottom of the tank in the beginning. The bottom of the tank is a transparent plastic foil sitting on a transparent glass through which the subsequent patterns are illuminated into the resin. The pattern of the first layer is illuminated as a dynamic mask by digital light processing technology (DLP®). After a certain illumination time the stage moves

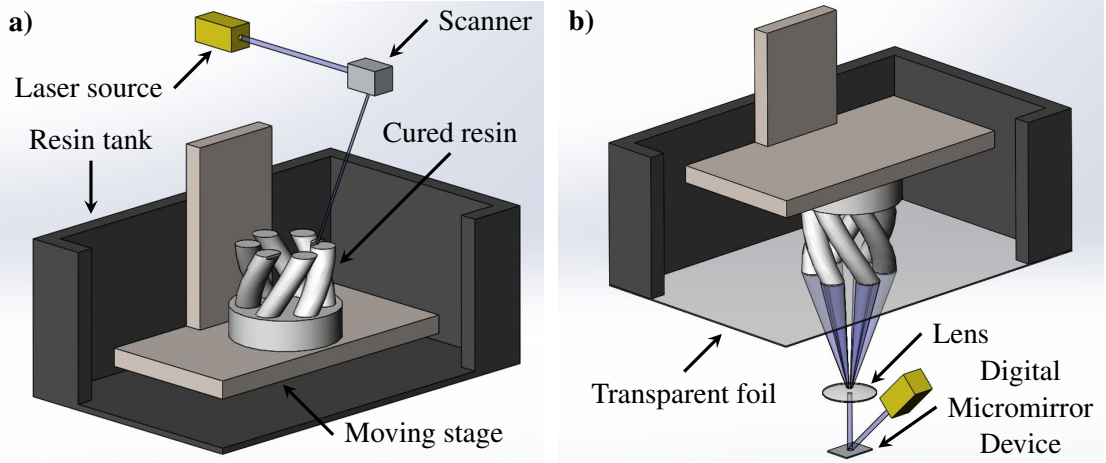

Figure 2.7: Schematic illustration of stereolithographic 3D printing approaches. In both images the resin tank is filled with resin. **a)** Free surface approach, where the tank is filled with resin until the currently printed layer. The moving stage moves downwards after each printed layer. **b)** Constrained surface approach, where the moving stage is moving upwards after each printed layer.

upwards by the height of the layer and the pattern of the next layer is illuminated into the resin directly below the first layer. This process is repeated until the last layer is printed and the process has finished.

The printer used during this thesis uses a constrained surface approach which has a few advantages compared to the free surface approach. First of all, the maximum height of the structure to be printed is not limited by the depth of the tank but by the distance the stage can move in the z-direction. Next, since the presence of oxygen may prevent the photopolymerization, there cannot be such an issue for the constrained surface approach. Another advantage is the higher throughput since the entire pattern of a layer can be illuminated at once instead of scanning the pattern row by row. Furthermore, the fact that the currently illuminated layer is in direct contact with the plastic foil at the bottom of the tank, a higher surface smoothness can be achieved. This fact however, can cause at the same time issues such that the illuminated layer sticks to the foil instead of polymerizing to the previously printed layer and thereby might lead to an unsuccessful print.

2.2.2 DIGITAL LIGHT PROCESSING TECHNOLOGY

The DLP technology is based on a digital micromirror device (DMD) which is a microelectromechanical system (MEMS). It was invented in 1987 at Texas Instruments [80] and comprises an array of $16\,\mu\mathrm{m}$ square aluminum micromirrors each positioned on top of an individually

controllable complementary metal-oxide-semiconductor (CMOS) static random access memory (SRAM) element as shown in Figure 2.8. The mirror is connected to an underlying yoke which is connected along the diagonal of the mirror via torsion hinges to support posts. The support posts are fixed to the underlying silicon substrate and the overall geometry of the device determines the maximum degree the micromirror can be tiltet in either direction which is mainly $+10°$ to $-10°$ with respect to the horizontal plane. The tilt in either direction is realized by generating an electric field between the micromirror and the electrodes placed on the CMOS element. The electrodes are positioned beneath the two corners of the micromirror along the diagonal which is orthogonal to the tilting diagonal. Depending on the polarity of the signal applied at the electrodes and thus the tilting direction of the mirrors, incident light is either directed to a projector lens ("ON" state of the pixel) or outside the lens aperture ("OFF" state of the pixel). The overall tilting degree of $20°$ of the mirror causes an overall tilting degree of $40°$ of the incident light. The light shines on the mirrors along a plane orthogonal to the tilting diagonal. By setting individual pixels to the "ON" state, a light pattern defined by these pixels, is directed via the lens through the transparent glass and the plastic foil into the resin.

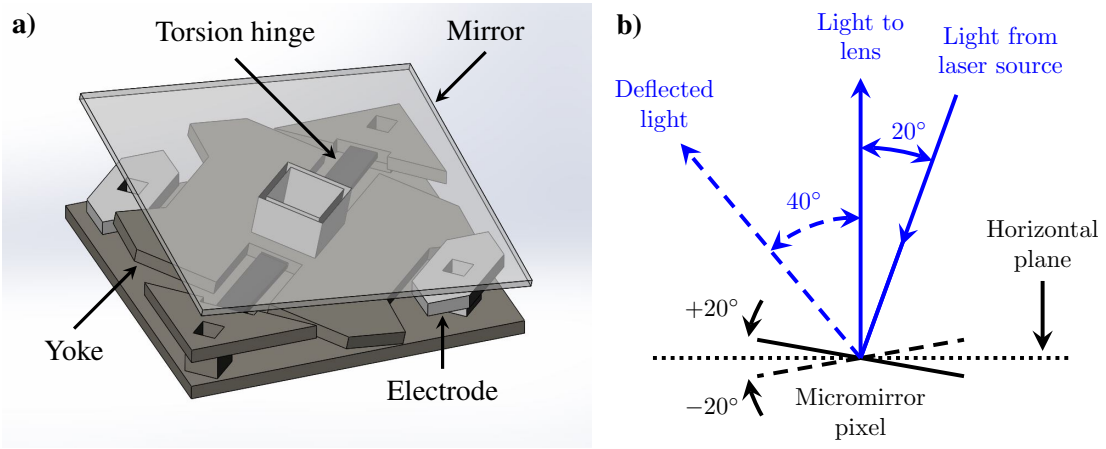

Figure 2.8: a) CAD image of one digital micromirror pixel. In the image the mirror is tilted $10°$ in one of the two possible direction. **b)** Illustration how the incident light is either reflected to the lens or away from it depending on the actual tilt of the individual micromirror pixel. Images were adapted from [80].

The pattern in the sliced layer might not be perfectly overlapping with the grid structure defined by the pixel dimensions of the DMD array. When a feature of the pattern is only partially covering a pixel, the amount of coverage is expressed as a gray scale value encoded in an eight or ten bit representation. The bit code is then used to rapidly switch the respective DMD pixel between its "ON" and "OFF" states during the illumination time of the layer. This is called DMD binary pulse width modulation where a higher value in bit representation equals a longer "ON" time of the individual pixel. In this way, features of the pattern covering a pixel not entirely are

only cured for a time proportional to their optical coverage.

The pixel array of stererolithographic printers can be arranged in either an orthogonal or in a $45°$ tilted diamond grid. The grid structure and the pixel dimensions should be known when designing the 3D object and positioning it in the printer's software. This and the information given in the previous paragraph is of special importance when a precise lateral resolution of certain features is required.

2.2.3 PHOTOPOLYMERIZATION PROCESS

The creation of three-dimensional objects from a mixture of monomers by the exposure to light is called photopolymerization. The process is initiated upon the absorption of light with a specific wavelength emission range which overlaps with the wavelength absorption range (UV range) of the photoinitiator inside the resin. This leads the photoinitiator to form free radicals $\mathrm{R}^{\cdot}$ which in turn leads to a chain polymerization reaction of functionalized monomers and oligomers.

$$\mathrm{Initiator} \longrightarrow \mathrm{R}^{\cdot} \tag{2.8}$$

Once the free radicals are created they react with the monomers of the resin and form active monomers $\mathrm{RM}^{\cdot}$.

$$\mathrm{R}^{\cdot} + \mathrm{M} \longrightarrow \mathrm{RM}^{\cdot} \tag{2.9}$$

These active monomers interact with the reactive bounds of oligomers $\mathrm{M_n}$ and form a polymer chain radical $\mathrm{RM_{n+1}}^{\cdot}$ which continues to grow.

$$\mathrm{RM}^{\cdot} + \mathrm{M_n} \longrightarrow \mathrm{RM_{n+1}}^{\cdot} \tag{2.10}$$

The growth of the polymer chain terminates upon the reaction of two chain radicals or when a hydrogen atom is transferred to another chain radical and two polymer chains are created.

$$\mathrm{RM_n}^{\cdot} + {}^{\cdot}\mathrm{M_mR} \longrightarrow \mathrm{RM_{n+m}R} \tag{2.11}$$

$$\textit{or} \tag{2.12}$$

$$\mathrm{RM_n}^{\cdot} + {}^{\cdot}\mathrm{M_mR} \longrightarrow \mathrm{RM_n} + \mathrm{M_mR} \tag{2.13}$$

The presence of oxygen can lead to inhibition of the chain growth by the formation of less reactive oxygen radicals. In order to ensure a throughout polymerization, the process should

take place in an atmosphere with inert gases. The photopolymers are developed such that there is as less shrinkage in volume as possible upon polymerization since it is desired that the printed 3D object has the same dimensions as in the CAD file.

An adaptation of Lambert Beer's law can be used to explain the photopolymerization rates mathematically.

$$I(d) = I_0 e^{-\alpha_\mathrm{p} d} \tag{2.14}$$

In the above equation $I(d)$ is the applied light intensity as a function of the light penetration depth inside the resin in $\mathrm{W\,m^{-2}}$, d is the light penetration depth in the direction of light propagation in m, α_p is the light absorption coefficient of the resin in $\mathrm{m^{-1}}$, and I_0 is the light intensity at $d = 0$, which is the horizontal plane where the light hits the resin. A critical dose D_c in $\mathrm{W\,s\,m^{-2}}$ can be defined for a light exposure time t_p, where the solidification has reached inside the resin until a depth d_p.

$$D_\mathrm{c} = t_\mathrm{p} I_0 e^{-d_\mathrm{p}/h_\mathrm{a}} \tag{2.15}$$

The light absorption coefficient is expressed here via the characteristic polymerization depth $h_\mathrm{a} = 1/\alpha_\mathrm{p}$. The critical exposure time t_c is defined as the time which is required by the light intensity I_0 to reach the polymerization of the resin at $d = 0$.

$$t_\mathrm{c} = \frac{D_\mathrm{c}}{I_0} \tag{2.16}$$

Combining the equation for the critical dose (Equation 2.15) and for the critical exposure time (Equation 2.16) and solving for the polymerization depth leads to Equation 2.17.

$$d_\mathrm{p} = h_\mathrm{a} \ln \frac{t_\mathrm{p}}{t_\mathrm{c}} \tag{2.17}$$

It describes for a resin whose critical exposure time and the characteristic polymerization depth are known how deep into the resin the polymerization reaches when it is exposed to light for a certain time. When these parameters are calibrated for a certain resin the effect of underexposure and overexposure must be considered. In case a layer is underexposed it might not be able to form a sufficiently strong connection to the previously printed layer and thereby cause the formation of erroneous structures. If the exposure is too high, the lateral dimensions might be larger than in the target file due to the undesired polymerization of areas adjacent to the exposed ones. Therefore, a trade-off between a stable connection between subsequent layers and the lateral resolution must be found for the successful print of a three dimensional object.

2.3 FABRICATION METHOD III: PATTERN-ASSISTED VACUUM FILTRATION

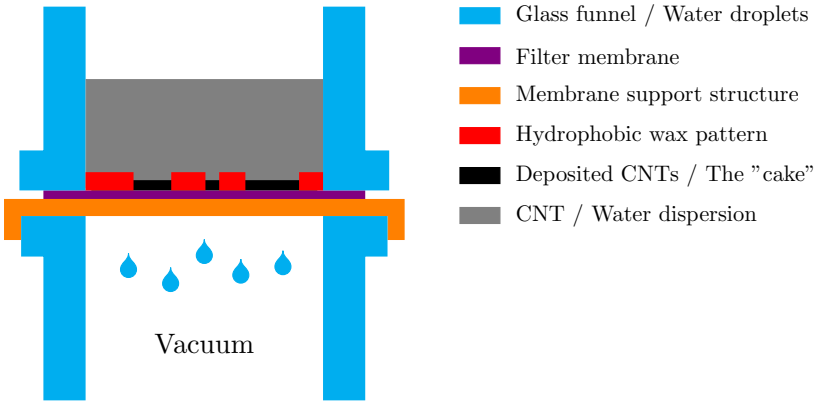

Figure 2.9: Working principle of pattern-assisted vacuum filtration. The filter membrane is patterned with a hydrophobic wax pattern. This ensured the CNT deposition only on the wax-free areas of the membrane. The membrane is placed on a support structure with a rough grid so that it does not influence the liquid flow. The dispersion is pulled through the membrane by applying vacuum from the glass funnel beneath.

Vacuum filtration is used to for distillation, extraction and purification of dispersions in chemistry. The dispersion is passed through a filter membrane by applying a vacuum from the other side of the membrane. Thereby, solid particles are separated from the liquid and are deposited on top of the filter. In pattern-assisted vacuum filtration the membrane is patterned with the negative of a desired structure so that the particles are deposited into the voids of the negative pattern. In this work, the pattern is printed with wax and the filtered medium is a homogeneous carbon nanotube dispersion. The hydrophobic surface of the negative wax pattern ensures that the carbon nanotubes are deposited solely on the wax-free areas of the filter membrane (Figure 2.9).

In vacuum filtration, the porous structure formed by the deposited material on the filter membrane is named as "cake". The resistance the dispersion is facing during its flow through the cake and the membrane is described by Darcy's law and the pressure drop of this flow, given in $\mathrm{kg\,m^{-1}\,s^{-2}}$, is described as follows:

$$\Delta p = \left(\frac{\dot{v}}{A}\right) h\eta\alpha_{\mathrm{H}} \tag{2.18}$$

Above, $\dot{v}$ is the volumetric flow rate in $\mathrm{m^3\,s^{-1}}$, A is the wax free area in $\mathrm{m^2}$, and the fraction $\dot{v}/A$ is the specific flow rate or the filtration velocity in $\mathrm{m\,s^{-1}}$. h is the cake thickness in m, η is the viscosity of the liquid in $\mathrm{Pa\,s}$, and α_H is the specific filter resistance of the cake in $\mathrm{m^{-2}}$. α_H depends on the porous structure and the number of pores of the cake and according to [81], it can be approximated (for a spherical particle system) by a form of the Kozeny-Carman equation as follows:

$$\alpha_\mathrm{H} \approx 150 \frac{(1-\epsilon_\mathrm{p})^2}{\epsilon_\mathrm{p}^3 d_\mathrm{S}^2} \tag{2.19}$$

In Equation 2.19, ϵ_p is the porosity or the void volume fraction of the porous medium and d_S is called the Sauter diameter which is an average diameter of the particle size distribution. The total pressure Δp_tot for a filtration system composed out of a cake and a filter membrane is the sum of the pressure drop across the cake Δp_1 and the pressure drop across the filter membrane Δp_2:

$$\Delta p_\mathrm{tot} = \Delta p_1 + \Delta p_2 = \left(\frac{\dot{v}}{A}\right) h\eta\alpha_\mathrm{H} + \left(\frac{\dot{v}}{A}\right)\eta\beta \tag{2.20}$$

where β is the filter resistance of the filter membrane in $\mathrm{m^{-1}}$.

2.4 ELECTROCHEMISTRY

In this chapter, the basics in electrochemistry about electrode potentials in equilibrium (no net current flow through the electrode) and when a net current is flowing through the electrode are explained. It gives an insight on the relation between the current flowing through an electrode and the electrical potential at the electrode. Also the physics of the interface between an electrode and the solution it is immersed in is described. The content of this chapter is based on [82, 83].

2.4.1 EQUILIBRIUM POTENTIAL OF REDOX ELECTRODES

The chemical potential μ characterizes the ability of a substance to react with other substances (chemical reaction), to change its form (phase transformation) or to distribute in space (diffusion). When a metal is immersed into a solution which comprises substances that can lose or gain electrons, the chemical potential of the electrons inside the metal and in the solution are not equal. Therefore, an electron transfer takes place which leads to the formation of an electrical potential difference between the metal and the solution. This process continues until the electrical potential difference between the metal and the solution is high enough to counteract the electron transfer and a state of electrochemical equilibrium is reached which is expressed as

follows:

$$\mu_{\mathrm{e}^-,\mathrm{S}} + zF\varphi_{\mathrm{S}} = \mu_{\mathrm{e}^-,\mathrm{Me}} + zF\varphi_{\mathrm{Me}} \tag{2.21}$$

or

$$\mu^0_{\mathrm{e}^-,\mathrm{S}} + RT\ln a_{\mathrm{e}^-,\mathrm{S}} + zF\varphi_{\mathrm{S}} = \mu^0_{\mathrm{e}^-,\mathrm{Me}} + RT\ln a_{\mathrm{e}^-,\mathrm{Me}} + zF\varphi_{\mathrm{Me}} \tag{2.22}$$

The incides e^-,S and e^-,Me stand for electrons in the solution and electrons in the metal, respectively. The sum $\mu + zF\varphi$ is named as the electrochemical potential and has the unit of $\mathrm{J\,mol^{-1}}$. φ_{S} and φ_{Me} are the electrical potentials in the solution and in the metal in the unit of V. The chemical potential μ consists of the concentration independent part μ^0 and the concentration dependent part $RT\ln a$. z is the valence, or the charge number of the metal. F is the Faraday constant and has the value of $96\,485\,\mathrm{C\,mol^{-1}}$. R is the molar gas constant and has the value of $8.314\,\mathrm{J\,K^{-1}\,mol^{-1}}$ and T is the temperature in K. The activity of the electrons in the metal is $a_{\mathrm{e}^-,\mathrm{Me}} = 1$. When $z = -1$, the equilibrium potential, also called as the Galvani potential, between the electrode and the solution is:

$$\Delta\varphi_0 = \varphi_{\mathrm{Me}} - \varphi_{\mathrm{S}} = \frac{\mu^0_{\mathrm{e}^-,\mathrm{Me}} - \mu^0_{\mathrm{e}^-,\mathrm{S}}}{F} - \frac{RT}{F}\ln a_{\mathrm{e}^-,\mathrm{S}} \tag{2.23}$$

The electron transfer process is a so-called redox reaction where the transfer of an electron from a redox active substance to the electrode is named as oxidation and the transfer in the other direction as reduction. In the simplest case it can be expressed as follows:

$$S_{\mathrm{ox}} + n\mathrm{e}^- \rightleftharpoons S_{\mathrm{red}} \tag{2.24}$$

Above, S_{ox} is the oxidized substance, S_{red} the reduced substance and n is the number of electrons transferred during the reaction. When the law of mass action is applied to the activity of the substances in the solution, the equilibrium constant K_{a} can be obtained as follows:

$$K_{\mathrm{a}} = \frac{a_{\mathrm{ox}}(a_{\mathrm{e}-,\mathrm{S}})^n}{a_{\mathrm{red}}} \tag{2.25}$$

or if rearranged:

$$a_{\mathrm{e}-,\mathrm{S}} = \left(K_{\mathrm{a}}\frac{a_{\mathrm{red}}}{a_{\mathrm{ox}}}\right)^{\frac{1}{n}} \tag{2.26}$$

When the expression found in Equation 2.26 in placed in Equation 2.23, the equilibrium potential for a redox electrode, which is referred to as the Nernst Equation, is obtained as:

$$\Delta\varphi_0 = \Delta\varphi_{00} + \frac{RT}{nF}\ln\frac{a_{\mathrm{ox}}}{a_{\mathrm{red}}} \tag{2.27}$$

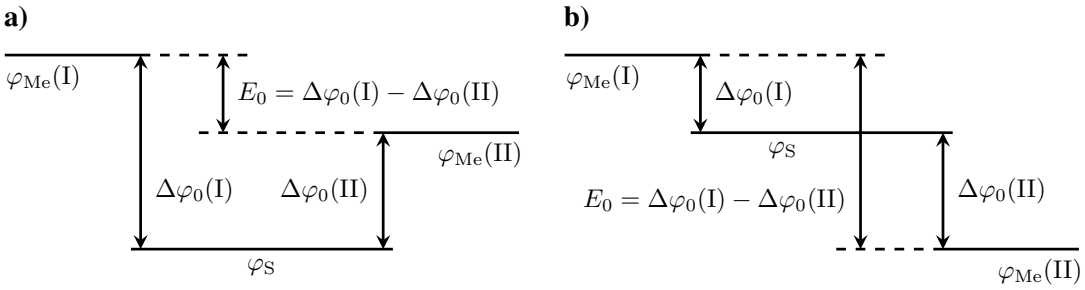

Figure 2.10: The potential difference between two electrodes which are in an equilibrium state inside the same solution. The potential differences between φ_{Me} and φ_{S} are illustrated only schematically. The actual potential curve between an electrode and the solution is shown in Figure 2.11. **a)** $\Delta\varphi_0(\mathrm{I}) > 0$, $\Delta\varphi_0(\mathrm{II}) > 0$. **b)** $\Delta\varphi_0(\mathrm{I}) > 0$, $\Delta\varphi_0(\mathrm{II}) < 0$. Figure was adapted from [82].

where $\Delta\varphi_{00}$ is the standard equilibrium potential and can be written as follows:

$$\Delta\varphi_{00} = \frac{\mu^0_{\mathrm{e}^-,\mathrm{Me}} - \mu^0_{\mathrm{e}^-,\mathrm{S}}}{F} - \frac{RT}{nF} \ln K_{\mathrm{a}} \tag{2.28}$$

When the potentials are given against a reference value which is defined later in this section, the equilibrium potential is given as:

$$\varphi_0 = \varphi_{00} + \frac{RT}{nF} \ln \frac{a_{\mathrm{ox}}}{a_{\mathrm{red}}} \tag{2.29}$$

In order to measure the potential difference between an electrode and the solution, the electrode can be contacted outside of the solution to an electronic measurement system directly, however, when the other contact of the device is immersed into the solution another equilibrium potential will be generated between that contact and the solution. Therefore a direct measurement of the equilibrium potential between an electrode and the solution is not possible. Only a measurement between two electrodes which are in an electrochemical equilibrium state can be performed. During the measurement both electrodes are immersed into the same solution and there is no net current flow between the contacts of the device. The potential difference between the equilibrium potentials $\Delta\varphi_0(\mathrm{I})$ and $\Delta\varphi_0(\mathrm{II})$ gives the electromotive force (emf) E_0 generated by the two electrodes (shown in Figure 2.10).

Since only the potential difference between two electrodes can be measured, the equilibrium potential of one electrode should be used as a common reference among experiments. This reference is the normal hydrogen electrode (NHE) which is a gas electrode and consists of a platinum plate residing in an acidic solution which comprises protons with the activity of 1 ($a_{\mathrm{H_3O^+}} = 1$) and is flushed with hydrogen gas at a pressure of $1013.25\,\mathrm{mbar}$. At this electrode

the following reaction takes place:

$$2\,\mathrm{H_3O^+} + 2\,\mathrm{e^-} \rightleftharpoons \mathrm{H_2} + 2\,\mathrm{H_2O} \tag{2.30}$$

The equilibrium potential of the hydrogen electrode is given as:

$$\varphi_0 = \varphi_{00} + \frac{RT}{F} \ln\left(\frac{a_{\mathrm{H_3O^+}}}{\sqrt{p_{\mathrm{H_2}}}}\right) \tag{2.31}$$

The standard equilibrium potential φ_{00} of Equation 2.31 is defined as zero. So the potential difference measured between an electrode and the NHE is the taken as the potential of the electrode.

Due to practical reasons (providing a precisely defined proton activity and pure hydrogen gas and getting rid of contamination on the platinum electrode) not the NHE electrode, but the silver chloride (Ag/AgCl) electrode is mainly used as a reference electrode. This is a metal ion electrode which consists of a silver wire that is coated with a silver chloride layer and resides in a solution in which a salt of the chloride is dissolved (mainly NaCl or KCl). The salt solution is inside a glass tube which is immersed into another solution where the other electrode resides whose potential is of interest. Both solutions are connected by a small glass frit inside the glass tube. For metal ion electrodes, which are electrodes immersed into a solution comprising the same metal's ions, the equilibrium potential is defined by the activity of the metal ion. In the case of the silver ion electrode by $a_{\mathrm{Ag^+}}$. The reaction is given by:

$$\mathrm{Ag} \rightleftharpoons \mathrm{Ag^+} + \mathrm{e^-} \tag{2.32}$$

The equilibrium potential for a silver ion electrode is given by:

$$\varphi_0^{\mathrm{Ag/Ag^+}} = \varphi_{00}^{\mathrm{Ag/Ag^+}} + \frac{RT}{F} \ln a_{\mathrm{Ag^+}} \tag{2.33}$$

The Ag^+ ions' activity is in equilibrium with the AgCl coating on the Ag wire. This coating has a low solubility which is why the Ag^+ ions' activity and therefore the equilibrium potential of the electrode is defined by the equilibrium constant $K_\mathrm{a} = a_{\mathrm{Ag^+}} a_{\mathrm{Cl^-}}$. Hence, the equilibrium potential of the silver chloride electrode can be stated as follows:

$$\varphi_0^{\mathrm{Ag/AgCl/Cl^-}} = \varphi_{00}^{\mathrm{Ag/Ag^+}} + \frac{RT}{F} \ln K_\mathrm{a}^{\mathrm{AgCl}} - \frac{RT}{F} \ln a_{\mathrm{Cl^-}} \tag{2.34}$$

In the equation above, the standard equilibrium potential of the silver chloride electrode is de-

fined as follows:

$$\varphi_{00}^{\mathrm{Ag/AgCl/Cl^-}} = \varphi_{00}^{\mathrm{Ag/Ag^+}} + \frac{RT}{F} \ln K_{\mathrm{a}}^{\mathrm{AgCl}} \tag{2.35}$$

The equilibrium potential of a silver chloride electrode depends on the activity of the chloride ions as stated in Equation 2.34. The salt of the Cl^- ions is highly soluble which is why the equilibrium potential can be controlled by the controlling the salt concentration of the solution is which the Ag wire resides. For example in a saturated KCl solution ($a_{\mathrm{Cl^-}} = 1$), with a standard equilibrium potential of $\varphi_{00}^{\mathrm{Ag/Ag^+}}$ =0.7996 V vs NHE for the silver ion electrode and an equilibrium constant of $K_{\mathrm{a}}^{\mathrm{AgCl}} = 1.78 \times 10^{-10}$, the equilibrium potential of the silver chloride reference electrode is $0.2224\,\mathrm{V}$ vs NHE.

2.4.2 ELECTRICAL DOUBLE LAYER BETWEEN THE ELECTRODE AND THE SOLUTION

When an electrode is charged and a potential difference is generated between the electrode and the solution, ions inside the solution with the opposite charge will be attracted to the electrode surface. A double layer is built where one side is presented by the electrode surface and the other by the plane on which the solvated ions' center of charge is residing (Figure 2.11). The distance between both layers is $a/2$, where a is the diameter of the solvated ions. This can be compared to a capacitor with a distance of $a/2$ between its conducting plates and is named as the static Helmholtz double layer [84]. The plane formed by the center of the ions is named as the outer Helmholtz layer. There is also an inner Helmholtz layer, residing between the electrode surface and the outer Helmholtz layer. It is formed by the center of charge of different ions which were for example stripped off their solvate shell and adsorbed to the electrode surface. This layer is not considered during the following description of the electrical double layer. The relation between potential and charge in space is given by Poisson's equation as follows:

$$\nabla^2 \varphi = -\frac{\rho_{\mathrm{E}}}{\epsilon} \tag{2.36}$$

When only an one-dimensional case is considered it can be written as follows:

$$\frac{\partial^2 \varphi}{\partial x^2} = -\frac{\rho_{\mathrm{E}}}{\epsilon} \tag{2.37}$$

In the equation above, φ is the electrode potential in V, ρ_{E} is the local charge density in $\mathrm{C\,m^{-3}}$ and ϵ is the solution's electric permittivity in $\mathrm{C\,V^{-1}\,m^{-1}}$. There is no charge in between both

layers. Therefore the integration of equation Equation 2.37 between both layers yields:

$$\frac{\partial \varphi}{\partial x} = const \tag{2.38}$$

This means, that there is a linear slope between the electrode potential φ_{el} and the outer Helmholtz layer $\varphi_{\mathrm{o.H.}}$ (Figure 2.11). The static electrochemical double layer model of Helmholtz does not entirely describe the real charge distribution in the solution in front of the electrode. According to Gouy-Chapman [85, 86], the charge distribution is modeled by a diffusive double layer due to the thermal movement energy of the ions. The description of this diffusive distribution considers the local concentration and the electrode potential. The local concentration of an ion with increasing distance from the electrode surface can be described by Boltzmann statistics and depends on its potential energy as follows:

$$c_{\mathrm{i}}(x) = c_{\mathrm{i},\infty} e^{\frac{-z_{\mathrm{i}} F \varphi(x)}{RT}} \tag{2.39}$$

In the equation above, $c_{\mathrm{i}}(x)$ is the local concentration of an ion i in $\mathrm{mol\,m^{-3}}$, x is the distance to the electrode surface in m, $c_{\mathrm{i},\infty}$ is the concentration of the ion i inside the solution (in theoretically infinite distance to the electrode surface), z_{i} is the valence of the ion i and $\varphi(x)$ is the local potential with respect to the potential of the solution φ_{S}. The local net charge density depends on the local ion concentration as follows:

$$\rho_{\mathrm{E}}(x) = \sum_i z_{\mathrm{i}} F c_{\mathrm{i}}(x) = \sum_i z_{\mathrm{i}} F c_{\mathrm{i},\infty} e^{\frac{-z_{\mathrm{i}} F \varphi(x)}{RT}} \tag{2.40}$$

Combining equation Equation 2.40 with Poisson's equation for the one-dimensional case gives the Poisson-Boltzmann equation, describing the course of the local potential in the solution with increasing distance from the electrode surface:

$$\nabla^2 \varphi(x) = -\frac{F}{\epsilon} \sum_i z_{\mathrm{i}} c_{\mathrm{i},\infty} e^{\frac{-z_{\mathrm{i}} F \varphi(x)}{RT}} \tag{2.41}$$

Solving the Poisson-Boltzmann equation gives the following dependence of the local potential $\varphi(x)$ from the electrode potential $\Delta\varphi_0(\varphi_{\mathrm{el}} - \varphi_{\mathrm{S}})$:

$$\varphi(x) = \frac{2RT}{zF} \ln \left(\frac{1 + \tanh\left(\frac{zF\Delta\varphi_0}{4RT}\right) e^{-\frac{x}{\lambda_{\mathrm{D}}}}}{1 - \tanh\left(\frac{zF\Delta\varphi_0}{4RT}\right) e^{-\frac{x}{\lambda_{\mathrm{D}}}}} \right) \tag{2.42}$$

For small potentials $\left(\Delta\varphi_0 < \frac{RT}{zF}\right)$, the Poisson-Boltzmann equation can be linearized. Solving it results in the following:

$$\varphi(x) = \Delta\varphi_0 e^{-\frac{x}{\lambda_\mathrm{D}}} \tag{2.43}$$

In both, the non-linearized and the linearized case, λ_D is a solution intrinsic property. It is named as the Debye length and is defined as follows:

$$\lambda_\mathrm{D} = \sqrt{\frac{\epsilon RT}{F^2 \sum\limits_i c_{\mathrm{i},\infty} z_\mathrm{i}^2}} \tag{2.44}$$

The Debye length is the distance from the electrode surface where the local potential with respect to the solution potential falls to the value $1/e$ of $\Delta\varphi_0$ for the linear Poisson-Boltzmann equation. According to Stern [87], however, charge carriers cannot approach the electrode surface closer than the radius of the solvated ion. Therefore, the double layer is actually a sum of the static double layer described by Helmholtz and the diffusive double layer. As can be seen in Figure 2.11, the local potential has a linear slope from the electrode surface until the outer Helmholtz layer and an exponential slope (for the linearized Poisson-Boltzmann equation) between the outer Helmholtz layer and the solution. Therefore, the equilibrium potential between the electrode and the solution $\Delta\varphi_0$ can be defined as follows:

$$\Delta\varphi_0 = (\varphi_\mathrm{el} - \varphi_\mathrm{o.H.}) + (\varphi_\mathrm{o.H.} - \varphi_\mathrm{S}) = \Delta\varphi_\mathrm{static} + \Delta\varphi_\mathrm{diffusive} \tag{2.45}$$

When ξ is used for the distance from a point inside the solution to the outer Helmholtz layer ($\xi = 0$ for $x = a/2$), the local potential inside the diffusive double layer in the combined model (Helmholtz plus the linearized version of the Poisson-Boltzmann equation) can be rewritten as follows:

$$\varphi(\xi) = (\varphi_\mathrm{o.H.} - \varphi_\mathrm{S}) e^{-\frac{\xi}{\lambda_\mathrm{D}}} + \varphi_\mathrm{S} \tag{2.46}$$

The potential difference $\varphi_\mathrm{o.H.} - \varphi_\mathrm{S}$ is referred to as the zeta potential. The radius of solvated ions are in the order of a few $0.1\,\mathrm{nm}$ and the thickness of the diffusive double layer (evaluated from the outer Helmholtz layer until $\xi = \lambda_\mathrm{D}$) is in the order of a few nm for diluted solutions. For concentrations around $c = 0.1\,\mathrm{mol\,l^{-1}}$ the thickness of the diffusive double layer is in the same order as the static Helmholtz double layer. For higher concentrations the diffusive double layer thickness can be neglected, so the entire double layer consists of only $\Delta\varphi_\mathrm{static}$. The capacitance of the electrical double layer is a serial connection of the Helmholtz double layer capacitance

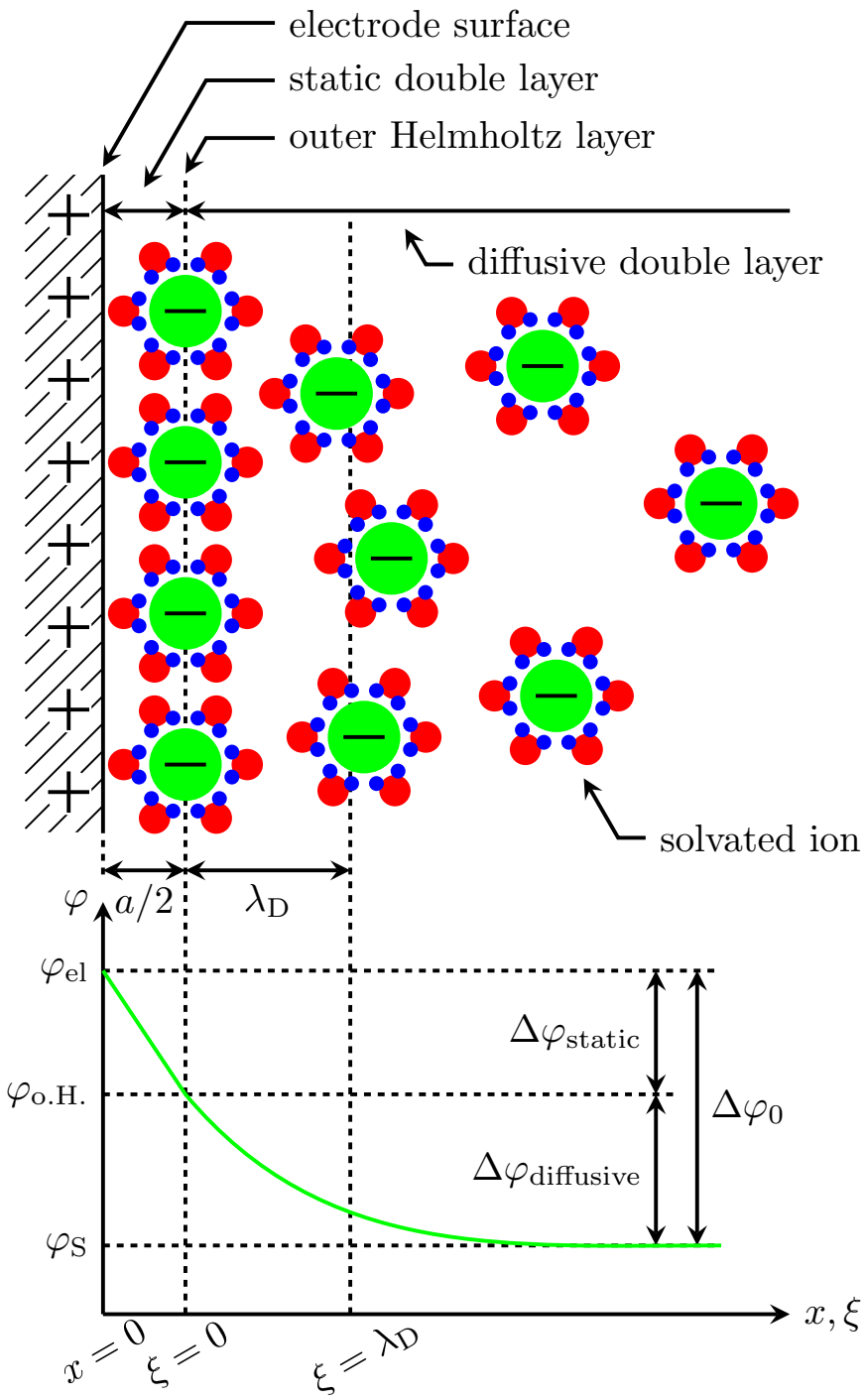

Figure 2.11: The course of the potential between an electrode and the solution. el: Electrode, o.H.: outer Helmholtz layer, S:solution, $\Delta\varphi_0$: equilibrium potential. $\xi = 0$ for $x = a/2$, a: diameter of the solvated ion. λ_D: Debye length. Figure was adapted from [82].

and the diffusive double layer capacitance and can be expressed as follows:

$$\frac{1}{C_{\mathrm{dl}}} = \frac{1}{C_{\mathrm{H.H.}}} + \frac{1}{C_{\mathrm{diffusive}}}, \quad C_{\mathrm{H.H.}} = \frac{\epsilon}{a/2} \quad \text{and} \quad C_{\mathrm{diffusive}} = \frac{\epsilon}{\lambda_{\mathrm{D}}} \tag{2.47}$$

2.4.3 ELECTRODE POTENTIAL DURING CURRENT FLOW

Until now, the equilibrium state of electrodes during which no net current flow takes place was considered. When a current is passed through an electrode its potential shifts from its equilibrium potential, the electrode polarizes. The difference between the new obtained potential φ and the equilibrium potential φ_0 is defined as the overpotential η_{o}. Such an overpotential develops at both the electrodes through which the current passes. Therefore, the overpotential for one electrode cannot be determined by using only two electrodes. Hence, a three electrode setup is used which consists of a working electrode, which is the electrode of interest, a counter electrode and a reference electrode. An electrical equivalent circuit for such a setup is shown in Figure 2.12. The current flowing through the working electrode equals the sum of the currents flowing through the reference and the counter electrode, where the current through the reference electrode is very small. While both the working electrode and the counter electrode polarize, the reference electrode maintains its equilibrium potential. So the potential difference measured between the working electrode and the reference electrode is the difference between the equilibrium potentials of both electrodes plus the polarization at the working electrode and the ohmic voltage drop across the solution between the working electrode and the reference electrode:

$$\Delta\varphi = (\Delta\varphi_{0,\mathrm{we}} - \Delta\varphi_{0,\mathrm{re}}) + \eta_{\mathrm{o}} + iR_{\mathrm{we-re}} \tag{2.48}$$

The current flowing through the electrode and the electrolyte can be either a capacitive current i_{c} in A, flowing through the double layer capacitance C_{dl} in F, a Faradaic current i_{f}, flowing thorugh the charge transfer resistance R_{ct} in Ω, or the sum of both $i_{\mathrm{total}} = i_{\mathrm{c}} + i_{\mathrm{f}}$. In case of a capacitive current only the double layer capacitance C_{dl} is charged which causes a redistribution of ions in the electrolyte. For a Faradaic current, an electron transfer occurs between the electrode and the electrolyte by either reducing or oxidizing species inside the solution. The capacitive current depends on the change rate of the overpotential as follows:

$$i_{\mathrm{c}} = C_{\mathrm{dl}} \frac{\mathrm{d}\eta_{\mathrm{o}}}{\mathrm{d}t} \tag{2.49}$$

The Faradaic current depends on the magnitude of the overpotential and is described by the

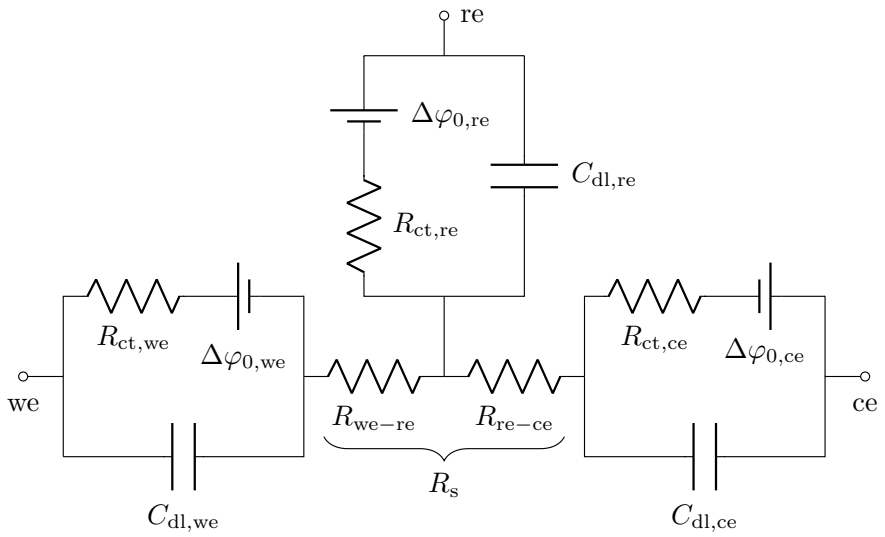

Figure 2.12: Electrical equivalent circuit of a three electrode setup consisting of a working (we), a counter (ce) and a reference (re) electrode. R_{ct}: charge transfer resistance, C_{dl} : double layer capacitance. $\Delta\varphi_0$: equilibrium potential. The solution resistance R_{s} is separated into a series connection a of solution resistance between the working electrode and and the reference electrode and another solution resistance between the reference electrode and the counter electrode. Figure was adapted from [83].

Butler-Volmer equation as follows:

$$i = i^+ + i^- = Aj_0 \left(e^{\frac{\alpha nF}{RT}\eta_{\mathrm{o}}} - e^{-\frac{(1-\alpha)nF}{RT}\eta_{\mathrm{o}}} \right) \tag{2.50}$$

In Equation 2.50 the overall current i is the sum of the partial currents i^+ and i^-, which are the oxidation and the reduction currents in A, respectively. The first exponential term belongs to the oxidation current and second to the reduction current. A is the real electrode area in m^2, j_0 is the exchange current density in $\mathrm{A\,m^{-2}}$, α is the transfer coefficient ($0 < \alpha < 1$, when the electrode potential is changed by $\Delta\varphi$, the energy of the transition state during a redox reaction is changed by $\alpha nF\Delta\varphi$ for a reaction flowing in the anodic direction). The exchange current density flows while the electrode potential is at its equilibrium potential (φ_0) and has the same magnitude in both, the anodic and cathodic direction, so that the net current is zero. The anodic exchange current density is defined as follows:

$$j^+(\varphi_0) = j_0 = nFc_{\mathrm{red}}k_0^+ e^{\frac{\alpha nF\varphi_0}{RT}} \tag{2.51}$$

The cathodic exchange current density is defined as follows:

$$j^-(\varphi_0) = -j_0 = -nFc_{\mathrm{ox}}k_0^- e^{-\frac{(1-\alpha)nF\varphi_0}{RT}} \tag{2.52}$$

In the equations above, $c_{\mathrm{red}}, c_{\mathrm{od}}$ are the concentrations of the reduced and oxidized species at the electrode surface in $\mathrm{mol\,m^{-3}}$, respectively. k_0^+, k_0^- are the heterogeneous rate constants in $\mathrm{m\,s^{-1}}$ for oxidation and reduction, respectively.

At the onset of the polarization, the current through the electrode is mainly a capacitive current charging the double layer. This leads to an increase in the overpotential which in turn leads to a rapid increase in the magnitude of the Faradaic current due to the exponential term in Equation 2.50. At higher overpotentials the current flowing through the Faradaic branch is dominating the overall current. When the double layer capacitance is fully charged, the electrode does not polarize any further and only a Faradaic current flows between the electrode and the electrolyte. While the capacitive current is a reversible current, the Faradaic current can be either reversible or irreversible. When after an electron transfer during a Faradaic process, the direction of the current is changed fast enough before the reduced or oxidized species have diffused away from the electrode surface, the electrochemical reaction at the surface can be reversed. Such a type of charge transfer is called a reversible Faradaic charge injection and the process is modeled by a capacitance, also named as a pseudocapacitance. When, however, the reduced or oxidized species diffuse away from the electrode surface, the charge during the redox reaction is lost. This is referred to as an irreversible Faradaic charge injection.

In a further case, where the concentration of substances exchanging electrons at the electrode surface becomes very low ($c_{\mathrm{ox}}, c_{\mathrm{red}} \rightarrow 0$) due to Faradaic reactions and the substances from the bulk solution cannot diffuse fast enough to the electrode surface, the system becomes mass transport limited. The Faradaic current cannot increase any further and the applied charge continues to charge the double layer capacitance. When the polarization is sufficiently high, the electrode potential will start to split water, which is another type of Faradaic current and not mass transport limited. At negative potentials, water is reduced and hydrogen gas is generated by the following reaction:

$$2\,\mathrm{H_2O} + 2\,\mathrm{e^-} \longrightarrow \mathrm{H_2}\uparrow + 2\,\mathrm{OH^-} \tag{2.53}$$

When the polarization is in the positive direction, water is oxidized and oxygen gas evolves by the following reaction:

$$2\,\mathrm{H_2O} \longrightarrow \mathrm{O_2}\uparrow + 4\,\mathrm{H^+} + 4\,\mathrm{e^-} \tag{2.54}$$

Since the gases diffuse away from the electrode surface, in both cases the amount of charge leading to the formation of the gases is lost. Therefore, both reactions are irreversible processes. The potentials at which water is split are named the water window. While passing current through an electrode the electrode potential should not pass these limits, since the formation of gas is harmful for both the stimulated tissue and the electrode. These limits are determined

using cyclic voltammetry (subsection 2.5.2).

2.4.4 ELECTRODE POTENTIAL DURING ELECTRICAL STIMULATION

Electrical stimulation of excitable tissue can be performed either by controlling the current (galvanostatic pulsing) or by controlling the potential (potentiostatic pulsing) between electrodes. Reference electrodes are not used in implantable systems due to the potential leakage of Ag^+ ions which can have toxic effects on tissue [88]. So the current or the potential is applied only between the working and the counter electrode in a two electrode setup. In nerve stimulation, usually the current is controlled because the activation of nerve tissue (eliciting an action potential) depends on the current magnitude and duration which both can vary among experiments when instead the voltage is controlled. This is due to changes in tissue or electrode properties after implantation. Therefore, the electrode polarization upon the application of biphasic current controlled stimulation pulses is described in the following.

In extracellular stimulation the electrode which is close to the targeted nerve tissue, the working electrode, is small (a few tens to hundreds of micrometer in diameter), the other electrode, the counter electrode, is located farther away and has a larger size. Due to its size, the counter electrode has a lower impedance (subsection 2.5.1) and its polarization upon current flow is small or negligible compared to the polarization of the working electrode. Hence, the polarization between both electrodes is mainly the polarization of the working electrode. For simplicity, the polarization of one electrode only (η_o) plus the potential drop across the solution resistance ($\Delta\varphi_\mathrm{s}$) is depicted in Figure 2.13. The first phase of a biphasic stimulation pulse, which mainly is a cathodic (negative) pulse applied at the working electrode (which is an anodic pulse for the counter electrode with the same magnitude and duration) is used to elicit nerve activation (action potentials). The second phase, which is in this case an anodic (positive) pulse, is used to reverse the effects of the first pulse. These are the charging of the double layer and any reversible electrochemical processes that might have occurred. If the charge transfer resistance is infinitely high ($R_\mathrm{ct} = \infty$), which means that no Faradaic currents occur and only the double layer capacitance is charged, the polarization has a linear slope (Figure 2.13 a). Upon reversal of the current, the charge stored between the electrode and the electrolyte can be canceled. The reached electrode potential during the first phase can thereby be brought back to its equilibrium potential. This model can also be applied if reversible Faradaic reactions are involved which are described with a pseudocapacitance as mentioned above. However, when the charge transfer resistance has a finite value ($R_\mathrm{ct} \neq \infty$), the polarization slope is not linear due to the irreversible current flowing

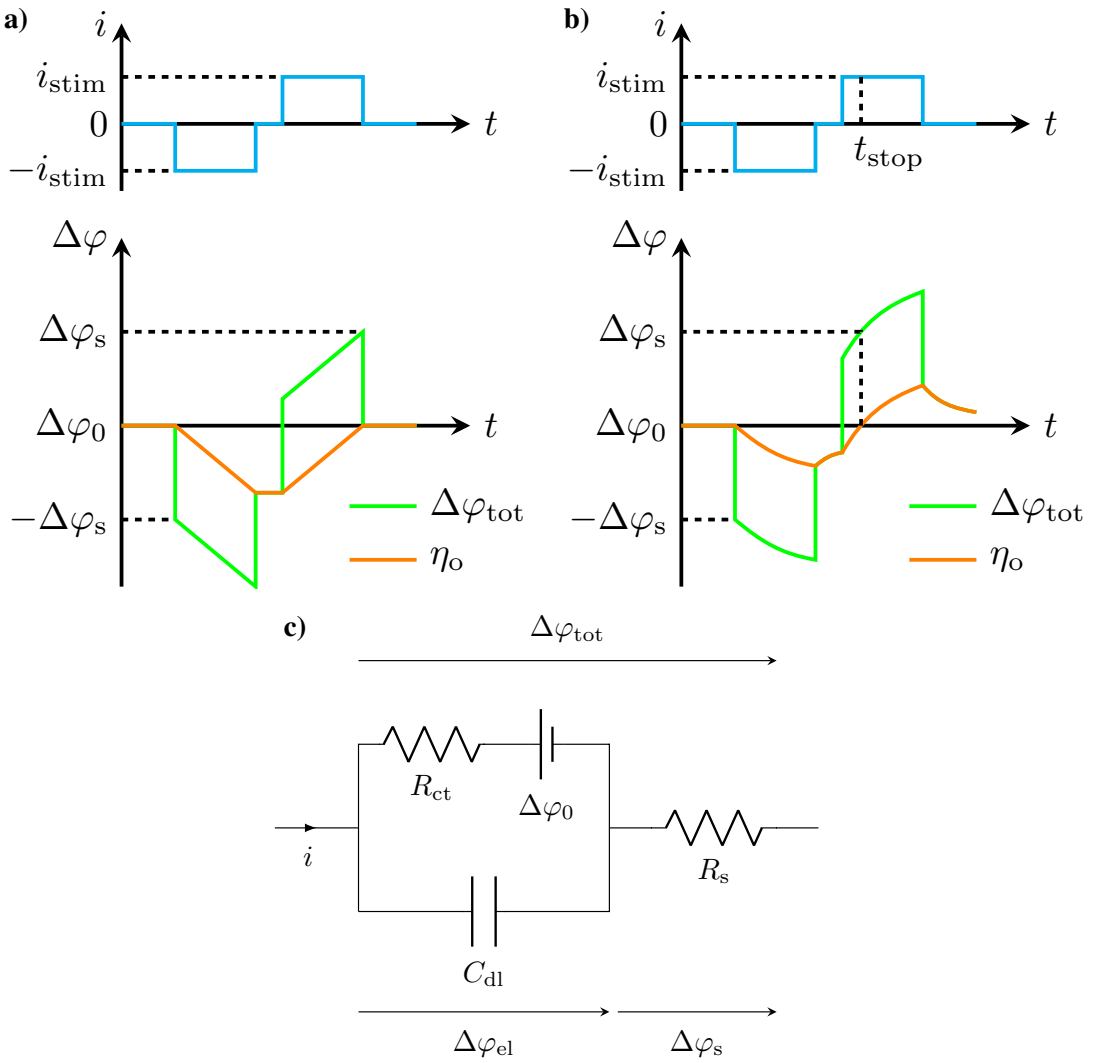

Figure 2.13: Polarization of an electrode upon current flow. i_{stim}: amplitude of the stimulation current, η_{o}: polarization across the electrode, $\Delta\varphi_{\mathrm{s}}$: potential drop across the solution resistance, $\Delta\varphi_{\mathrm{tot}} = \eta_{\mathrm{o}} + \Delta\varphi_{\mathrm{s}}$: overall polarization, $\Delta\varphi_0$: equilibrium potential at the electrode which is not zero. $\Delta\varphi_{\mathrm{el}} = \eta_{\mathrm{o}} + \Delta\varphi_0$. **a)** Polarization when $R_{\mathrm{ct}} = \infty$. **b)** Polarization when $R_{\mathrm{ct}} \neq \infty$. **c)** Electrical equivalent circuit of one electrode plus the solution resistance. Figure was adapted from [89].

through R_{ct} (Figure 2.13 b). The slope can be described by the following equation:

$$\eta_{\mathrm{o}}(t) = i(t)R_{\mathrm{ct}}(1 - e^{-\frac{t}{R_{\mathrm{ct}}C_{\mathrm{dl}}}}) \tag{2.55}$$

In case of a charge balanced waveform, the charge in both phases is the same. During the first phase only a fraction of the applied charge is used to charge the double layer capacitance while the other fraction is lost in irreversible Faradaic reactions. In order to bring the electrode potential back to its equilibrium value only the charge stored at the double layer capacitance needs to be reversed. So the charge applied in the second phase is more than what would be sufficient to achieve this. Hence, the excess charge polarizes the electrode towards a more positive value (Figure 2.13 b). Additionally, during both phases and during two biphasic stimulation pulses, when no current is applied, the charge stored at the double layer capacitance discharges through R_{ct} which also leads to a shift in the electrode potential. The discharging of the overpotential while no current is applied can be described by the following equation:

$$\eta_{\mathrm{o}}(t) = \eta_{\mathrm{off}} e^{-\frac{t}{R_{\mathrm{ct}}C_{\mathrm{dl}}}} \tag{2.56}$$

In Equation 2.56, η_{off} is the reached overpotential when the current is turned off. When a second biphasic pulse is applied before the electrode potential has reached its equilibrium value, the reached potential after the second pulse will be even higher than the potential after the first biphasic pulse. In the case of multiple such consecutive pulses, the electrode potential could reach a value high enough to split water which is an undesired situation. One measure to prevent this, is to use charge imbalanced pulses where the second phase is stopped as soon as the electrode potential has reached its equilibrium value (Figure 2.13 b). In this case, the difference between the duration of the cathodic phase and the anodic phase multiplied with the current amplitude would be a measure of the amount of lost charge during irreversible Faradaic currents. This method has the advantage that there is no reference electrode required and it can be carried out with implanted electrodes as well.

2.5 ELECTROCHEMICAL CHARACTERIZATION TECHNIQUES

In the following, three electrochemical characterization techniques are explained. These techniques were used throughout this study and give information regarding the essential properties of stimulation electrodes which must be considered during the system design of stimulation applications. At the end, a short introduction about an electrode surface modification technique is given.

2.5.1 ELECTRODE CHARACTERIZATION TECHNIQUE I: ELECTROCHEMICAL IMPEDANCE SPECTROSCOPY

An important property of electrodes is their impedance. In implantable stimulation devices, it determines the voltage drop across the electrode for a desired stimulation current range. This is a value of high interest when for example considering the power requirements of the stimulation device during its design. It is determined using a technique called electrochemical impedance spectroscopy (EIS). The electrical equivalent circuit of an electrode is shown in Figure 2.13 c. In the following, the battery indicating the equilibrium potential of the electrode is neglected and such a circuit is called a simplified version of Randles circuit (R_s included). Since the impedance of a capacitor is frequency dependent, the overall electrode impedance is frequency dependent as well. In order to determine the magnitude of the electrode impedance for a frequency spectrum of interest (1 Hz-1 MHz), a alternating voltage signal with a small amplitude ($V_\mathrm{A} = 10\,\mathrm{mV}$) at different frequencies is applied at the electrode mainly while it at its equilibrium potential. The signal can also be applied while there is an overpotential at the electrode. For the following considerations, $\eta_\mathrm{o} \ll \frac{RT}{nF}$. At the same time, the current flowing through the electrode is measured. The measurement is performed in a three electrode setup. The voltage and the current will have the same frequency, however, due to the capacitor, there will be a different phase shift (θ) between the signals for each frequency. The division of both signals gives the impedance Z of the electrode (or rather system, electrode plus solution resistance). Even though the voltage current relationship is not linear at an electrode, for small potentials used in EIS, it can be considered as linear. Therefore the following equations can be stated:

$$Z = \frac{V(t)}{i(t)} = \frac{V_\mathrm{A} e^{j\omega t}}{i_\mathrm{A} e^{j(\omega t - \theta)}} = |Z| e^{j\theta} = |Z|(\cos\theta + j\sin\theta) \tag{2.57}$$

As can be seen in the equation above, the impedance Z is a complex number. The overall impedance in terms of the parallel connection of the charge transfer resistance R_ct and the double layer capacitance C_dl in series to the solution resistance R_s can be stated as follows:

$$Z = R_\mathrm{s} + Z_\mathrm{el}, \quad \frac{1}{Z_\mathrm{el}} = \frac{1}{R_\mathrm{ct}} + \frac{1}{Z_{\mathrm{C_{dl}}}} = \frac{1}{R_\mathrm{ct}} + j\omega C_\mathrm{dl}, \quad Z_{\mathrm{C_{dl}}} = -j\frac{1}{\omega C_\mathrm{dl}} \tag{2.58}$$

$$Z = R_\mathrm{s} + \frac{R_\mathrm{ct}}{1 + (\omega R_\mathrm{ct} C_\mathrm{dl})^2} - j\frac{\omega R_\mathrm{ct}^2 C_\mathrm{dl}}{1 + (\omega R_\mathrm{ct} C_\mathrm{dl})^2} \tag{2.59}$$

$$|Z| = \sqrt{Re(Z)^2 + Im(Z)^2}, \quad \theta = \arctan\left(\frac{|Im(Z)|}{Re(Z)}\right) \tag{2.60}$$

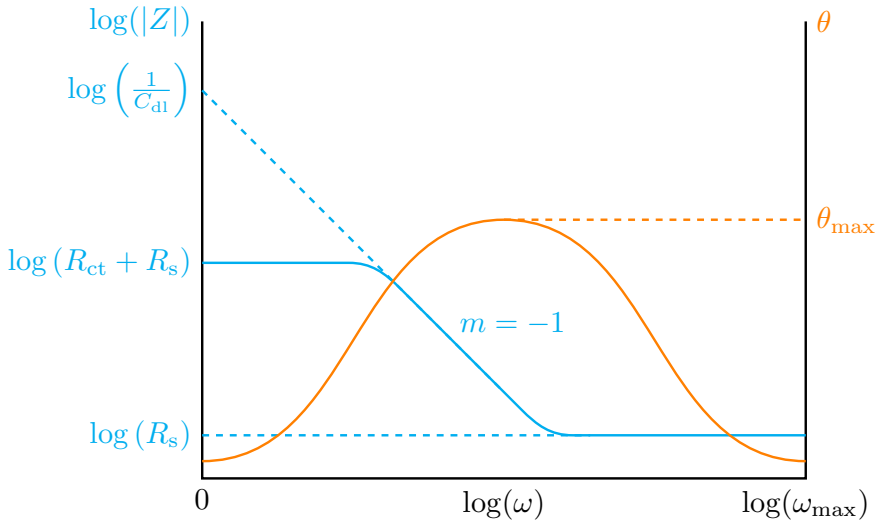

Figure 2.14: Bode plot obtained during an electrochemical impedance spectroscopy measurement. The cyan curve represent the logarithm of the impedance $|Z|$. The orange curve represents the phase shift between the voltage and the current signal θ. ω is the circular frequency. R_s is the solution resistance, R_ct is the charge transfer resistance, C_dl is the double layer capacitance. m is the slope of the impedance curve in the middle of the graph. Figure was adapted from [82].

The magnitude of Z and θ can be depicted for the frequency range within which the alternating voltage signal was applied in a so-called Bode plot as shown in Figure 2.14. For small frequencies, $Z_{\mathrm{C_{dl}}}$ goes toward infinity and the branch of C_dl can be considered as an open ciruit. The impedance of the equivalent circuit consists then only of the sum of R_ct and R_s. For higher frequencies $Z_{\mathrm{C_{dl}}}$ goes toward zero and the branch of C_dl can be considered as a short circuit. In that case the impedance of the equivalent circuit consists of only R_s. Furthermore, the middle part of the $|Z|$ curve has a slope of $m = -1$ and extrapolating this curve to the y-axis for $\omega \to 0$ gives $\log(\frac{1}{C_\mathrm{dl}})$.

As mentioned above, the calculations described are for the simplified Randles circuit. In the normal Randles circuit there is a frequency dependent resistance called the Warburg impedance Z_W which is in series to the charge transfer resistance. It describes the concentration changes in the diffusive double layer (subsection 2.4.2) upon application of an alternating voltage signal. It is important for electrode analysis when mass transport to the electrode is a limiting factor. For the simplified Randles circuit, a kinetically controlled case is considered which is why the Warburg impedance can be neglected.

2.5.2 ELECTRODE CHARACTERIZATION TECHNIQUE II: CYCLIC VOLTAMMETRY

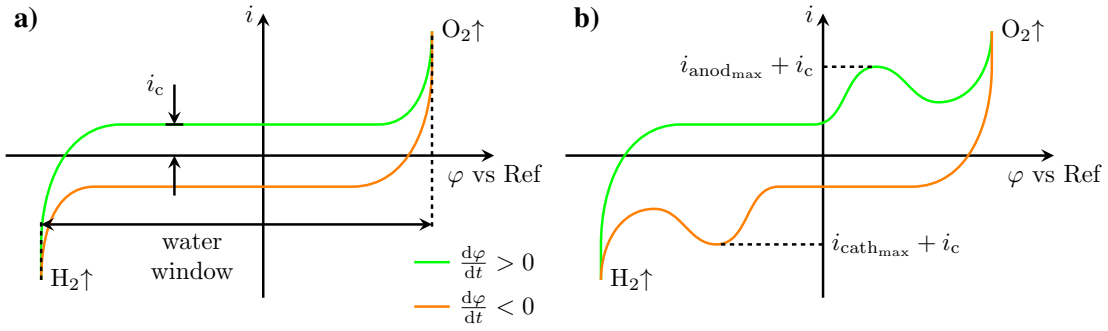

Figure 2.15: Cyclic voltammetry measurement at an electrode. Ref: equilibrium potential of a reference electrode. Green curve: when the electrode potential is increased. Orange curve: when the electrode potential is decreased. **a)** Only capacitive charging of the double layer capacitance. i_c: capacitive current. **b)** Capacitive charging in addition to Faradaic currents due to redox active active species. i_{anod}: anodic current. i_{cath}: cathodic current.

Another method for electrode characterization and to analyze electrochemical processes at the electrode is cyclic voltammetry. In this technqiue the working electrode is linearly polarized in a three electrode setup between two potentials back and forth with a certain voltage ramp (scan rate v_s ≈10–100 $\mathrm{mV\,s^{-1}}$) and the current is measured. For aqueous solutions, the limits are mainly the potentials at which hydrogen gas or oxygen gas in generated (Figure 2.15). By sweeping the electrode potentials in both the anodic and cathodic direction, the electrode surface can be freed from adsorbed species from the solution which helps in obtaining reproducible results in experiments. This technique is used to analyze electrode coatings and processes occurring at the electrode. In case there are no redox active species inside the solution, the measured current comes mainly from adsorption and desorption of hydrogen and oxygen atoms or other ions to the electrode surface and is a capacitive current. The magnitude is dependent on the scan rate. When the potential limits are chosen close to the equilibrium potential of the electrode (e.g. $\eta_o = \pm 100\,\mathrm{mV}$ vs φ_0), the electrode capacitance can be evaluated by following equation:

$$C = \frac{|i_{cath}| + i_{anod}}{2v_s} \tag{2.61}$$

In the equation above, i_{cath} and i_{anod} are the cathodic and anodic currents measured at $\eta_o = 0\,\mathrm{V}$ vs φ_0. For simulation electrodes, the charge evaluated by integrating the current between its water oxidation and reduction potentials is referred to as the charge storage capacity (CSC) and is a characteristic property for the electrode material. It is a measure for the reversible charge

that can be stored in the electrical double layer and can also be used to measure the real electrochemical surface of the electrode. If redox active species are available inside the solution, the measured current is the sum of capacitive and Faradaic currents. While the capacitive current has the same magnitude throughout the sweep range, the Faradaic currents occur at certain potentials or potential ranges. By varying the scan rate both currents can be separated from each other. For small scan rates, the capacitive currents can be neglected. The curve represents the normal $\eta_{\mathrm{o}}(t) - i(t)$ curve of the redox reaction at the electrode. For higher scan rates, the capacitive currents dominate the overall current. Both currents are independent from each other.

2.5.3 ELECTRODE CHARACTERIZATION TECHNIQUE III: VOLTAGE TRANSIENTS

For stimulation electrodes, the CSC (subsection 2.5.2) is usually divided into a cathodic part (area beneath the voltage axis) and an anodic part (area above the voltage axis) and only one part is used for characterizing the electrode. This is because only one phase is responsible for the activation of neural tissue, regardless whether the pulse in monophasic, biphasic, cathodic or anodic. The CSC is used as an important quantity in the literature of neural stimulation electrodes. However, it does not represent the maximum amount of charge that can be injected safely during a stimulation pulse because the assessment method is quasi-stationary (with a duration of up to a few minutes until the electrode has polarized) while stimulation typically relies on short voltage or current pulses (with a duration of micro- to a few milliseconds).

A method to determine a maximum amount of safe charge injection is to measure the voltage transient at the stimulation electrode vs a reference electrode upon the application of a current pulse. Here, the current amplitude is increased until the electrode polarization (measured as the total potential difference minus the potential drop across the solution resistance, refer to Figure 2.13) has reached either the water oxidation, water reduction, or any other specified potential. In case the applied signal is a biphasic pulse, the charge in the leading phase is then named as the charge injection limit (CIL) or charge injection capacity (CIC). Since it was shown theoretically and experimentally that cathodic currents provide more efficient stimulation compared to anodic currents [90, 91], the CIC values reported in literature are determined mainly using a cathodic leading phase. Important to mention is that the CIC values are in general lower than the CSC values. During CIC assessment, the electrode is at its equilibrium potential (somewhere between the water oxidation and reduction potentials) at the onset of the stimulation pulse. Thus, the polarization does not occur across the entire water window as it is the case during a CV measurement for determination of the CSC value. Furthermore, the CIC is not only dependent on the electrode material but also on the duration of the applied stimulation

current. Hence, for the determination of the CIC, the exact shape and temporal characteristics of the stimulation pulse should be considered as well.

2.5.4 ELECTRODE SURFACE MODIFICATION TECHNIQUE: ELECTRODEPOSITION

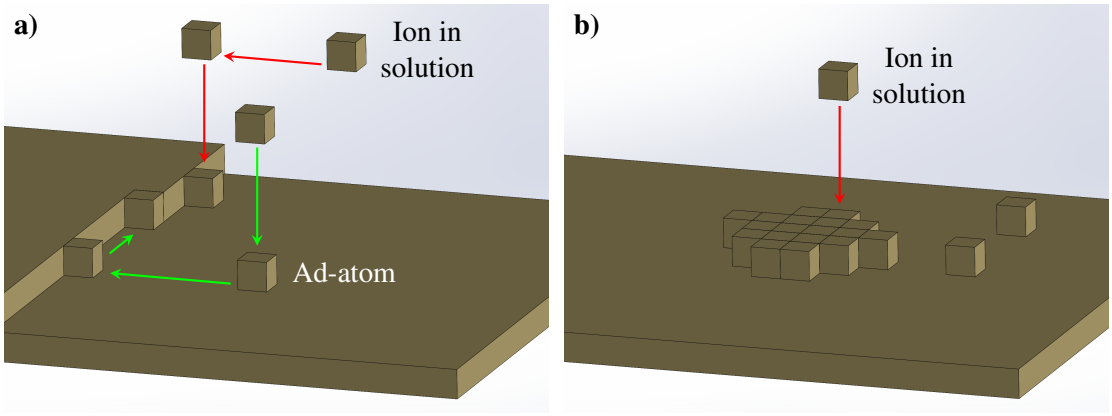

Figure 2.16: Schematic illustration of electrodeposition of metal ions. **a)** Adsorption onto the electrode surface and surface diffusion to the next suitable point in the metal lattice (green arrows) or diffusion inside the solution and direct deposition into the metal lattice (red arrows). **b)** Deposition and island growth formation. Figure was adapted from [92].

Electrodeposition is used to coat the surface of an electrode or an entire object with another material in order to modify its electrical or electrochemical properties or to only change its appearance. This is done by passing a current through the electrode to either reduce metal ions from a solution or to polymerize a conducting polymer, such as PEDOT:PSS (subsection 2.7.2, [93]), on the surface. In this work, Au was used to cover the surface of inkjet printed Ag electrodes and in combination with PEDOT:PSS to plate carbon nanotube conductors. It was selected due to its high electrical conductivity, its resistance against corrosion, its chemical inertness and due to its biocompatibility. In the following, only the electrodeposition of Au is explained. PEDOT:PSS was not electropolymerized from its monomers, but a solution containing the final polymer was used to directly deposit it on the carbon nanotube conductors.

In aqueous solutions for Au deposition, the metal is in the form of a $[Au(CN)_2]^-$ complex which is more stable than the bare Au ion itself. This form has a standard equilibrium potential between -0.611 and $-0.595\,\mathrm{V}$ vs NHE [94] which enables the usage of lower potentials during electrodeposition. This is crucial since using potentials in the magnitude range of the standard equilibrium potential of Au^+ ($1.42\,\mathrm{V}$ vs NHE [92]) can lead to the electrolysis of water

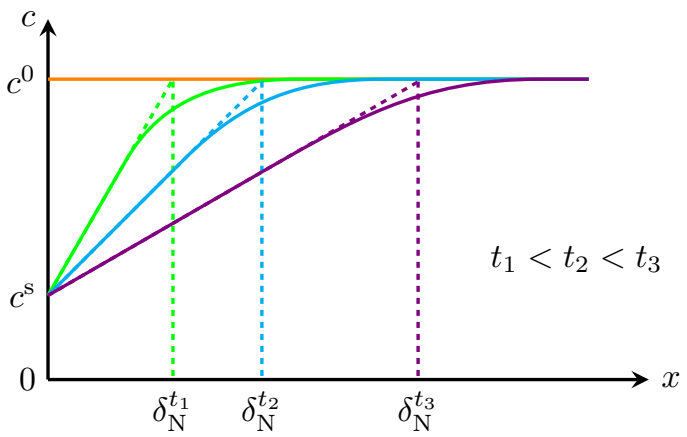

Figure 2.17: Concentration profile of metal ions upon application of a constant overpotential. x denotes the distance from the electrode surface towards the solution. c^0 is the ion concentration inside the solution, c^s is the ion concentration at the electrode surface. The longer the overpotential is applied, the more the diffusive layer δ_N widens into the solution. Figure was adapted from [92].

and thereby damage the electrode (subsection 2.4.3). In this work, anohter complex, namely $K[Au(CN)_2]$, was used for Au deposition and the electrochemical process is as follows:

$$K[Au(CN)_2] + e^- \rightleftharpoons Au + KCN + CN^- \tag{2.62}$$

The electrochemical technique used for electrodeposition is chronoamperometry, where the potential of the working electrode is controlled versus a reference electrode (Ag/AgCl, subsection 2.4.1) in a three electrode setup. When the electrode's potential is deviated from its equilibrium potential, a current will flow through the electrode as described in subsection 2.4.3. This will attract the metal complex to the surface of the electrode where it strips off from its ligands, deposits on the electrode surface and receives an electron. The metal ion, after it has diffused from the solution towards the electrode surface and is adsorbed there, is named as ad-atom. It can now migrate via surface diffusion towards the next suitable point in the metal lattice or start the growth of an island via further adsorbed metal ions around it (Figure 2.16).

Upon onset of a constant overpotential the concentration at the electrode surface drops from the concentration inside the solution c^0 to a value c^s within seconds. The concentration profile which forms between the electrode surface and the solution has a thickness of $\approx \delta_N$, called the Nernst diffusion layer (Figure 2.17). It is defined as follows:

$$\delta_N = \frac{c^0 - c^s}{(\partial c/\partial x)_{x=0}} \tag{2.63}$$

When the applied overpotential is as high as the potentials used for electrodeposition, the reaction at the electrode is controlled by the diffusion of ions towards the electrode. During current flow, the ion concentration at the electrode surface remains constant and the diffusive layer δ_{N} increases with time into the solution according to:

$$\delta_{\mathrm{N}} = \sqrt{\pi D t} \tag{2.64}$$

Above, D is the diffusion coefficient and t is the time during which the overpotential is applied. This equation applies for an infinitely extended electrode surface in a semi-infinite domain and represents the diffusion in an one-dimensional scenario. The increase of the diffusive layer causes a decrease in the current density through the electrode. Its course over time can be described as follows:

$$j = nF\sqrt{D/\pi t}(c^0 - c^{\mathrm{s}}) \tag{2.65}$$

Depending on how high the overpotential is and how long it is applied, the ion concentration at the electrode surface and the concentration profile from the electrode surface towards the solution can vary. When the diffusion of ions is not fast enough the ion concentration in the diffusive layer can be depleted very fast. In order to prevent this and promote the mass transport towards the surface, a pulsed method instead of a continuously applied potential can be used. In this case, the ion concentration in the diffusive layer has time to increase during the period the pulse is turned off. This method can yield to a smoother surface coverage of the deposited metal.

2.6 ELECTROPHYSIOLOGY

In this section, basics about neuronal anatomy and the electrical potential across a neuron's cell membrane is explained. The electrical signals in neurons, named as action potentials, are described and finally, the basics of how these signals can artificially be generated is given.

2.6.1 MEMBRANE POTENTIAL AND ACTION POTENTIAL

The basic anatomy of a neuron is composed out of a soma (cell body) to which many dendrites and one axon is connected (Figure 2.18). For neurons in the peripheral nervous system, the axon is wrapped with so-called Schwan cells. They provide an electrical insulation between the axon and the extracellular medium and the possibility for an action potential to move faster along an axon. An action potential is the change of the membrane potential which is a voltage difference across the cell membrane and is explained in detail further below in this section. In

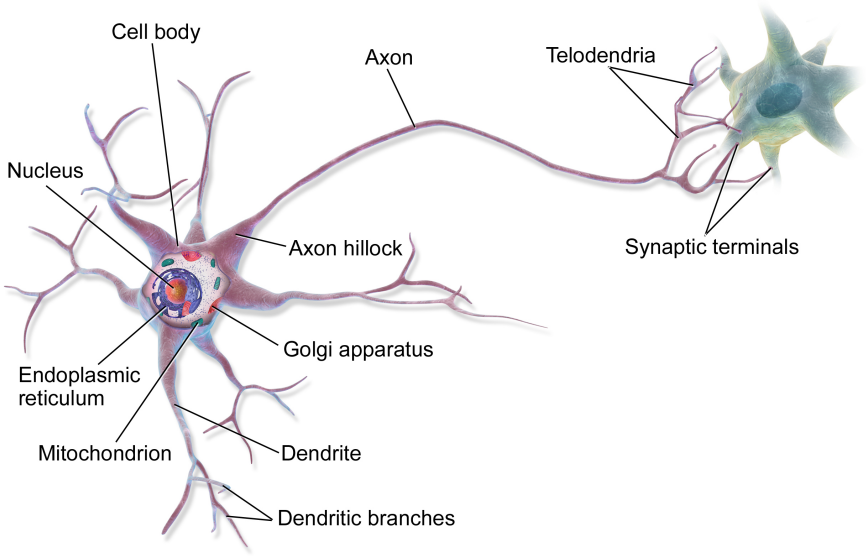

Figure 2.18: Anatomy of a neuron. Figure was adopted from [95].

between two Schwann cells, the axon is exposed to the extracellular medium. This small area is called the Node of Ranvier. The action potential generated at the soma moves down the axon and when it reaches its distal end, where it is connected to the dendrites of other neurons, it leads to the secretion of certain chemicals (contained in vesicles which combine with the neuron's membrane upon arrival of the action potential, exocytosis). These connections are called synapses and have small gaps. The secreted chemicals are called neurotransmitters and diffuse inside these gaps toward the receptors of the dendrites. Depending the type of synapse they either contribute to (excitatory) or prevent (inhibitory) the generation of an action potential in the soma (more specifically at the axon hillock) of the other neurons.

As mentioned above, the neuron has a voltage difference across its cell membrane which is $\approx -70\,\mathrm{mV}$ and is called the resting potential of the membrane. This value is provided by the measurement from the inside of the cell versus the outside, which means that the cell membrane is positive outside and negative inside. The resting potential is determined by an equilibrium state of concentration gradients of certain ions across the membrane, the membrane's permeability for each type of ion, so-called ions pumps and large anions inside the cell which cannot cross the membrane. Mainly three type of ions contribute to the resting potential. Sodium and chloride which have a higher concentration outside the cell and a smaller concentration inside and potassium which has a higher concentration inside the cell and a smaller concentration outside. The membrane is embedded with different types of proteins, called ion channels, with each type of channel permeable for one type of ion. Considering an electrically neutral state, for example

for potassium, in the inside and the outside of the cell, the potassium ions will diffuse down their concentration gradient from the inside to the outside of the cell, which leads to a charge separation across the membrane. The inside will become more negative and the outside more positive. This continues until the electrical potential difference across the membrane has reached a value which prevents a net potassium ion flux to the outside. The chemical force acting on the ions due to the concentration gradient is counterbalanced by the electrical force acting on the ions due to the electrical potential difference. This voltage is called the equilibrium potential of potassium ions and has a value of $\approx -90\,\mathrm{mV}$ (defined from the inside versus the outside). The equilibrium potential of an ion in defined as the voltage to maintain the concentration gradient of that ion across the membrane. It can be derived by first defining the diffusive flux (due to the concentration gradient, Equation 2.66) and the electrophoretically induced drift flux (due to the electrical potential difference, Equation 2.67):

$$\vec{J}_{\mathrm{diff}} = -D_{\mathrm{i}}\vec{\nabla}c_{\mathrm{i}} \tag{2.66}$$

$$\vec{J}_{\mathrm{elec}} = \frac{zF}{RT}D_{\mathrm{i}}\vec{E}c_{\mathrm{i}} \tag{2.67}$$

Equation 2.66 is called Fick's first law of diffusion. Equation 2.67 is a term from the Nernst-Planck equation which describes the motion of charged particles in a fluid medium. The Nernst-Planck equation is Fick's second law of diffusion with a term added to describe also the movement of charged particles due to electrostatic forces. D_{i} is the diffusion coefficient for the ion i. Setting both fluxes equal for an one-dimensional case results in the following:

$$\frac{\partial\varphi}{\partial x} = -\frac{RT}{zFc_{\mathrm{i}}}\frac{\partial c_{\mathrm{i}}}{\partial x} \tag{2.68}$$

$$\varphi_{\mathrm{m}} = \varphi_{\mathrm{in}} - \varphi_{\mathrm{out}} = -\frac{RT}{zF}\ln\left(\frac{c_{\mathrm{in}}}{c_{\mathrm{out}}}\right) \tag{2.69}$$

The indices m, in and out stand for membrane, inside the cell and outside the cell, respectively. The equilibrium potential for sodium and chloride are defined the same way and have values of $\approx 60\,\mathrm{mV}$ and $-70\,\mathrm{mV}$, respectively. The resting potential is a combination of these equilibrium potentials and is closer to the equilibrium potential of potassium because in the resting state, the permeability of potassium ion channels is higher than the permeability of sodium ion channels. It can be calculated using the Goldman-Hodgkin-Katz equation as follows:

$$\varphi_{\mathrm{m}} = -\frac{RT}{F}\ln\left(\frac{P_{\mathrm{Na^+}}c_{\mathrm{Na^+,in}} + P_{\mathrm{K^+}}c_{\mathrm{K^+,in}} + P_{\mathrm{Cl^-}}c_{\mathrm{Cl^-,out}}}{P_{\mathrm{Na^+}}c_{\mathrm{Na^+,out}} + P_{\mathrm{K^+}}c_{\mathrm{K^+,out}} + P_{\mathrm{Cl^-}}c_{\mathrm{Cl^-,in}}}\right) \tag{2.70}$$

In Equation 2.70, P_{i} is the permeability for the ion i in $\mathrm{m\,s^{-1}}$. Since the resting potential of the cell membrane is different than the equilibrium potentials of sodium and potassium, there is a constant flux of sodium ions inside the cell and of potassium ions outside the cell. There is another protein embedded in the cell membrane called the ion pump which constantly pumps three sodium ions to the outside and for every two potassium ions to the inside of the cell. This mechanism counteracts the leakage fluxes described above and maintains the concentration gradients stable.

As mentioned above, there are receptors in the cell membrane of the dendrites. These are ligand gated sodium ion channels. When neurotransmitters in the synaptic cleft diffuse toward these receptors and bind to them, the ion channels open and lead to an influx of sodium which makes the inside of the cell membrane at the dendrites less negative. This is called depolarization. The inward flux of sodium of multiple dendrites leads also to a decrease in the membrane voltage at the soma. At the area of the axon hillock, there is an increased density of voltage gated ion channels, the sodium and potassium ions channels described above. Their permeability is controlled by the electrical potential difference across the cell membrane. When the membrane potential at the axon hillock reaches a threshold value, sodium ion channels start to increase their permeability yielding in a higher influx of sodium inside the cell compared to the resting state. This depolarizes the membrane potential even more which in turn leads to a further increase in sodium ion channel permeability. This positive feedback continues until a maximum value of depolarization is reached where the membrane potential becomes positive inside and negative outside. Afterward, the sodium ion channels start to close and stay closed for a certain time duration. During depolarization, also the potassium ion channels' permeability starts to increase, however, a little slower than the sodium ion channels, leading to a higher outflux of potassium ions. Due to the diffusion of potassium ions outside the cell, the depolarization starts to decrease. The increased permeability of potassium ion channels lasts longer than for sodium ion channels. Therefore, the membrane potential not only reaches its resting potential value, but even becomes more negative. This is referred to as hyperpolarization. Slowly, the permeability for potassium decreases as well and the membrane potential reaches its resting potential value again. While all this happens, the ion pump mentioned earlier constantly works to reestablish the concentration gradients at the resting state and the resting membrane potential. The described change of the membrane potential is named as an action potential. The time duration between the membrane potential crossing the threshold value and reaching its resting value again for the first time is referred to the absolute refractory period during which no other action potential can occur. The time duration between the start of hyperpolarization and the membrane potential reaching its resting value again for the second time is referred to the relative refractory period during which another action potential may occur, however, a stronger excitation is necessary.

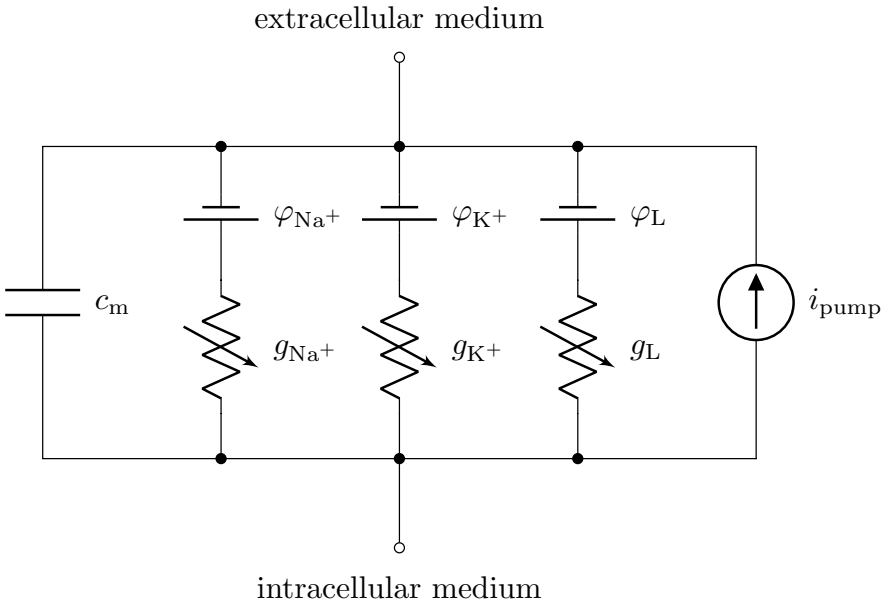

Figure 2.19: Electrical equivalent model of a patch from the squid's axonal membrane. c_{m}: specific membrane capacitance, φ_{i}: equilibrium potential values for sodium and potassium ion channels and for leakage currents. g_{i}: conductances to model the membrane's permeability to sodium, potassium and leakage currents. i_{pump}: sodium potassium ion pump. Figure was adapted from [2].

The ion channels in the cell membrane along the axon area all voltage gated. The depolarization of the cell membrane at the axon hillock leads to a slight depolarization of a neighboring membrane area in the axon. When the depolarization of the neighboring area has reached the threshold value, an action potential is triggered there as well. This is the mechanism how action potentials travel along the axon. The refractory period of the ion channels prevent the occurrence of another action potential at an area where it was just fired during the action potential generation at the neighboring area. Hence, biologically generated action potentials move only in one direction. Due to the myelin sheath available around axons in peripheral neurons, the action potentials are generated only at the nodes of Ranvier which is why the signal can travel along the axon faster compared to an axon without myelin sheath. Neuronal information sent along an axon is encoded in the number of action potentials and in the time interval between them.

Hodgkin and Huxley conducted experiments with the giant axon of a squid and fitted a mathematical model to quantitatively describe the dynamics between the membrane potential and the permeability of the neuron's cell membrane to sodium and potassium [2]. According to their model, the electrical equivalent circuit of a patch of the unmyelinated cell membrane is as depicted in Figure 2.19. As mentioned above, the cell membrane separates charges between the inside and the outside of the cell. Therefore, it can be modeled as a capacitor. The equilibrium

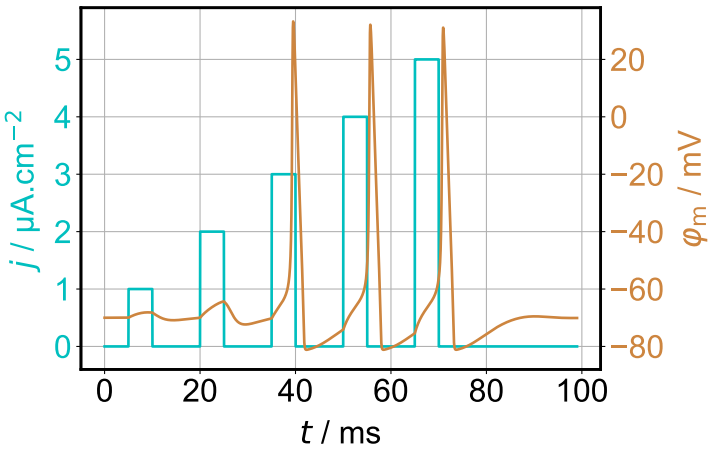

Figure 2.20: Simulation of an intracellular stimulation of a point cell with an anodic current. The membrane dynamics are modeled according to the equations of Hodgkin and Huxley [2].

potentials for sodium and potassium are modeled as batteries and the permeabilities of the ion channels to ion flux are modeled as variable resistors, since their value depends on the actual electrical potential difference across the cell membrane. An additional branch is included, also with a battery and a variable resistor to model the leakage currents. The net outward current sustained by the sodium potassium ion pump is modeled as a current source. In equilibrium, the sum of the capacitive current density through the membrane and the ionic current densities is zero and can be stated as follows (the ion pump is neglected):

$$c_\mathrm{m}\frac{\mathrm{d}\varphi_\mathrm{m}}{\mathrm{d}t} + j_{\mathrm{Na}^+} + j_{\mathrm{K}^+} + j_\mathrm{L} = 0 \tag{2.71}$$

$$c_\mathrm{m}\frac{\mathrm{d}\varphi_\mathrm{m}}{\mathrm{d}t} + g_{\mathrm{Na}^+}(\varphi_\mathrm{m} - \varphi_{\mathrm{Na}^+}) + g_{\mathrm{K}^+}(\varphi_\mathrm{m} - \varphi_{\mathrm{K}^+}) + g_\mathrm{L}(\varphi_\mathrm{m} - \varphi_\mathrm{L}) = 0 \tag{2.72}$$

In the equations above c_m is the membrane's specific capacitance. j_i is the current density of the ionic and leakage currents. g_i is the conductance value per unit area for the sodium and potassium ion channels and the leakage currents. All conductance values depend on the membrane potential. φ_m is the actual value of the membrane potential and φ_i are the equilibrium potential values for the sodium and potassium ion channels and the leakage currents.

Considering a point cell (without any dimensions) which is being stimulated by an anodic current, this sum of current densities is equal to the stimulation current density. As can be seen in Figure 2.20, when the stimulation current density is not high enough only a slight depolarization of the membrane potential can be observed. However, when the current density is higher than a certain value, an action potential is generated.

2.6.2 BASICS OF EXTRACELLULAR NERVE FIBER STIMULATION

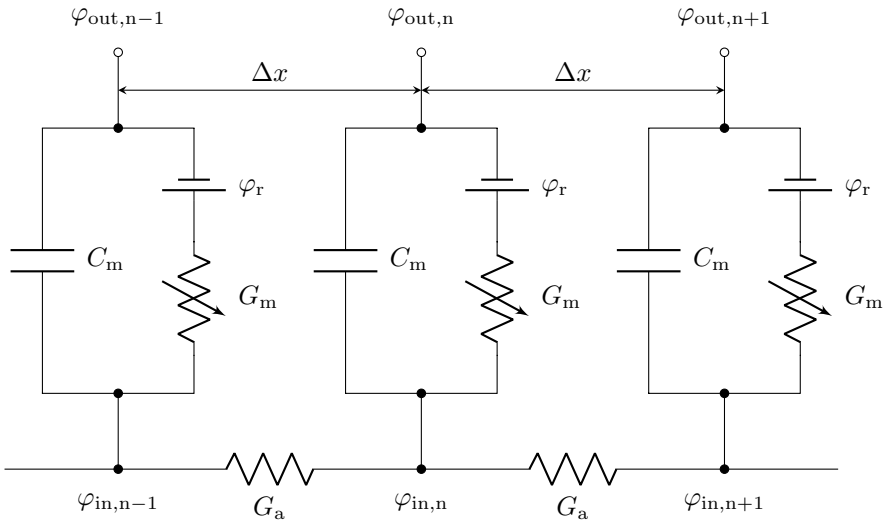

Figure 2.21: Electrical equivalent model of a patch of an axon. The axon is segmented into compartments which are seperated by Δx. For unmyelinated nerve fibers, Δx is the accuracy with which the potentials along the axon are computed. For myelinated fibers, Δx is the pitch between two adjacent nodes of Ranvier. φ_{in}: intracellular potential, φ_{out}: extracellular potential, φ_{r}: membrane resting potential, C_{m}: membrane capacitance of one compartment. G_{m}: ionic conductance, G_{a}: axonal conductance between two compartments. Figure was adapted from [96].

In the following the mathematical basics of extracellular stimulation of a part of an unmyelinated axon with an electrode located in its vicinity is explained according to [90, 96]. This technique relies on the electrical potential gradient along the axon induced by the current flowing through the electrode. First, the part of the axon being simulated is divided into segments of Δx, which is the length of a segment between two cross-sections of the axon. At each cross-section, the external and internal potential and the currents flowing across the membrane and through the axon are defined. The currents are induced by the electrical potential differences between each point. The membrane current at node n is equal to the sum of the capacitive and ionic currents through the membrane and to the sum of the axial currents through the axon. They can be stated as follows:

$$C_{\mathrm{m}}\frac{d(\varphi_{\mathrm{in,n}}-\varphi_{\mathrm{out,n}})}{dt}+i_{\mathrm{ionic,n}}=G_{\mathrm{a}}(\varphi_{\mathrm{in,n-1}}-\varphi_{\mathrm{in,n}})+G_{\mathrm{a}}(\varphi_{\mathrm{in,n+1}}-\varphi_{\mathrm{in,n}}) \tag{2.73}$$

For further computations, the so-called reduced potential φ_{n} is used which is defined as follows:

$$\varphi_{\mathrm{n}}=\varphi_{\mathrm{in,n}}-\varphi_{\mathrm{out,n}}-\varphi_{\mathrm{r}} \tag{2.74}$$

Equation 2.73 can be rewritten with φ_n as:

$$\frac{d\varphi_\mathrm{n}}{dt} = \frac{1}{C_\mathrm{m}} \left(G_\mathrm{a} (\varphi_{\mathrm{n}-1} - 2\varphi_\mathrm{n} + \varphi_{\mathrm{n}+1} + \varphi_{\mathrm{out,n}-1} - 2\varphi_\mathrm{out,n} + \varphi_{\mathrm{out,n}+1}) - i_\mathrm{ionic,n} \right) \quad (2.75)$$

The membrane capacitance and axonal conductance are defined as follows:

$$C_\mathrm{m} = \pi d_\mathrm{a} L c_\mathrm{m} \qquad G_\mathrm{a} = \frac{\pi d^2}{4\rho_\mathrm{in}\Delta x} \quad (2.76)$$

Above, d_a is the axon diameter, L is the length of the active membrane (membrane in direct contact to the extracellular medium, $L = \Delta x$ for unmyelinated fibers, $L \neq \Delta x$ for myelinated fibers), c_m is the membrane's specific capacitance, ρ_in is the resistivity of the medium inside the axon. When Equation 2.74 is rewritten with the definitions for the membrane capacitance and the axonal conductance it is as follows:

$$\frac{d\varphi_\mathrm{n}}{dt} = \frac{1}{c_\mathrm{m}} \left(\frac{d_\mathrm{a}\Delta x}{4\rho_\mathrm{in} L} \left(\frac{\varphi_{\mathrm{n}-1} - 2\varphi_\mathrm{n} + \varphi_{\mathrm{n}+1}}{\Delta x^2} + \frac{\varphi_{\mathrm{out,n}-1} - 2\varphi_\mathrm{out,n} + \varphi_{\mathrm{out,n}+1}}{\Delta x^2} \right) - j_\mathrm{ionic,n} \right) \quad (2.77)$$

In Equation 2.77, $j_\mathrm{ionic,n}$ is the ionic current density and can be calculated using the equations provided by Hodgkin and Huxley [2] for unmyelinated fibers and the equations provided by Frankenhaeuser and Huxley [5] for myelinated fibers. For the possibility of an action potential generation, φ_n must become positive. According to Equation 2.77, the term comprising the external potentials φ_out has a direct influence on φ_n. This term is referred to as the activating function f_n [90].

$$f_\mathrm{n}(t) = \frac{\varphi_{\mathrm{out,n}-1}(t) - 2\varphi_\mathrm{out,n}(t) + \varphi_{\mathrm{out,n}+1}(t)}{\Delta x^2} \quad (2.78)$$

At locations along the axon, where f_n is positive, the membrane potential depolarizes and in case the magnitude of depolarization is sufficiently high, an action potential can be generated. At locations where f_n is negative, hyperpolarization occurs. Including the indirect influence of the ionic currents, the membrane response to an external potential gradient along the axon can be computed.

Assuming an isotropic extracellular medium with a resistivity of ρ_out in which a spherical electrode is placed close to an axon as depicted in Figure 2.22 a, the external potential along the axon can be computed as follows:

$$\varphi_\mathrm{out} = \frac{\rho_\mathrm{out} i}{4\pi r} \quad (2.79)$$

In the equation above, i is the current flowing through the electrode and r is the distance between the electrode and each compartment for which the external potential is calculated. Further assumptions are that the presence of the axon does not interfere with the generated external

potential field and that the counter electrode is placed infinitely far away. In reality it is placed so far away that the potential field generated around it does not have an influence on the external potential along the axon. Also, membrane current density variations over a segment are neglected.

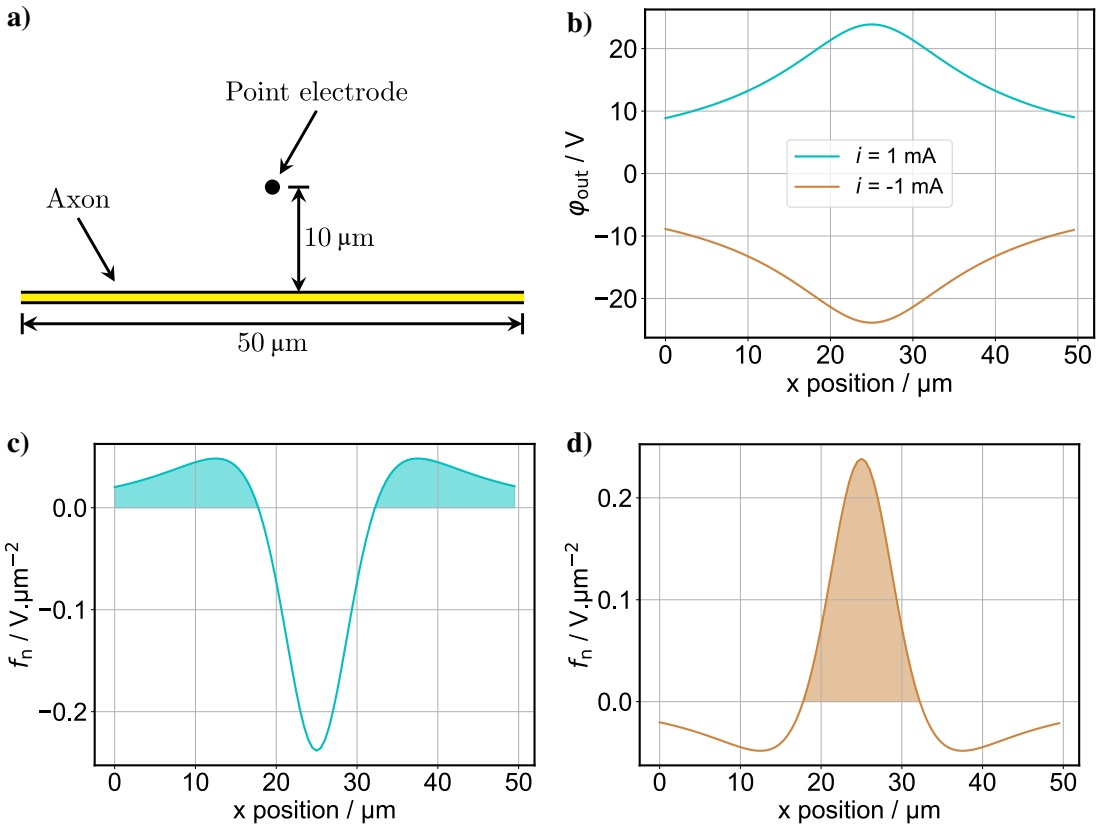

Figure 2.22: a) Schematic illustration of a $50\,\mu\mathrm{m}$ section of an unmyelinated axon and a point electrode. The point electrode resides $10\,\mu\mathrm{m}$ above the middle of the axon section. **b)** Simulation results of the distribution of the extracellular potential φ_{out} along the axon section for an anodic and a cathodic current of $1\,\mathrm{mA}$ amplitude. **c)** Simulation results of the activating function along the axon section for an anodic current of $1\,\mathrm{mA}$. **d)** The activating function for a cathodic current of $-1\,\mathrm{mA}$. The membrane potential depolarizes in the shaded areas and hyperpolarizes when the activating function $f_{\mathrm{n}} < 0$. Action potentials can occur in the shaded areas in case the degree of depolarization is sufficiently high. The resistivity of the extracellular medium is $3\,\Omega\,\mathrm{m}$ and the distance between the compartments is $\Delta x = 0.5\,\mu\mathrm{m}$.

In Figure 2.22 b, the external potential along a short unmyelinated axon section upon the application of an anodic and a cathodic constant current by a point electrode in its vicinity is depicted. Also the activating function along the axon and the depolarized areas where an action potential could be elicited is shown (Figure 2.22 c and d). In Figure 2.23, simulation results of the membrane potential's response for both currents is shown. The membrane depolarizes only

slightly at the lateral sections of the axon and no action potential is generated for an anodic current of $1\,\mathrm{mA}$ amplitude. However, for a cathodic current of the same magnitude, the membrane depolarizes high enough to generate an action potential in the middle of the axon section. The simulation shows that anodic currents require more charge to elicit action potentials compared to cathodic currents. In cases where the latter are too strong, they can inhibit action potential propagation due to a still lasting hyperpolarization at more distant nodes, when the action potential arrives at these nodes.

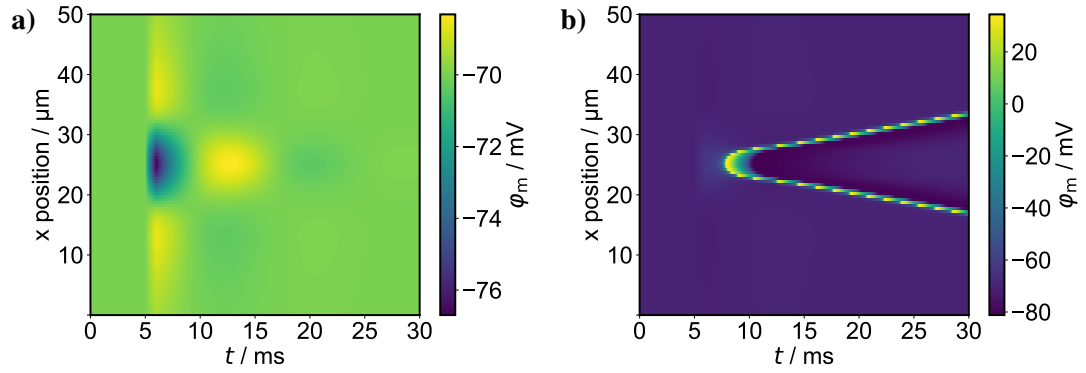

Figure 2.23: Simulation results for the extracellular stimulation of an unmyelinated axon of $50\,\mu\mathrm{m}$ length by a point electrode residing $10\,\mu\mathrm{m}$ above the middle of the axon section. The stimulation is performed by a constant current of $1\,\mathrm{ms}$ duration applied at $t = 5\,\mathrm{ms}$. **a)** Membrane depolarization for an anodic current of $1\,\mathrm{mA}$ amplitude. The membrane depolarizes at the lateral sections of the axon and hyperpolarizes in the middle. However, the depolarization is not high enough to elicit an action potential. The hyperpolarized section depolarizes after a while and regains the resting potential. **b)** Membrane depolarization for a cathodic current of $-1\,\mathrm{mA}$ amplitude. The membrane depolarizes in the middle of the axon and an action potential is elicitied which propagates in both directions.

2.7 ELECTRODE MATERIALS

Besides traditional electrode materials in neural interfacing applications such as steel, Pt or Au, several new materials are emerging. In this chapter, a short overview of two such materials is given. These are carbon nanotubes and poly(3,4-ethylenedioxythophene) polystyrene sulfonate (PEDOT:PSS) which are either used directly as electrodes or as electrode coatings in this work.

2.7.1 CARBON NANOTUBES

Carbon nanotubes (CNTs) are graphene sheets rolled to form hollow cylinders. They are available as either single-walled tubes consisting of only one graphene wall or as multi-walled

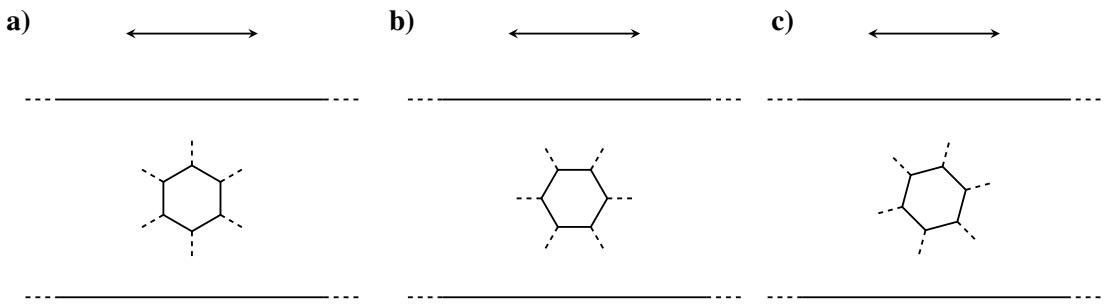

Figure 2.24: Schematic illustration of the hexagonal lattice orientation with respect to the CNT's longitudinal dimension which is shown by the double headed arrows. **a)** Armchair type. **b)** Zigzag type. **c)** Chiral type.

tubes which comprise multiple single-walled tubes nested into each other. CNTs have a high-aspect-ratio structure with diameters in the range a few of nanometers [97] and lengths ranging from a few micrometers up several millimeters [98]. Depending on how the hexagonal carbon atom lattice of the wall is tilted with respect to the length of the tube, its structure is indicated with the integer indices n and m [99]. In case $n = m$ (Figure 2.24 a) the structure is named as armchair, for $(n, 0)$ it is named as zigzag (Figure 2.24 b) and for all other (n, m) combinations, it is named as chiral (Figure 2.24 c). When $n = m$ or $n - m$ is a multiple integer of three, the nanotube has metallic electrical properties, in all other cases it shows semiconducting properties [99].

CNTs have remarkable properties such as a high tensile strength [100], high thermal conductivity [101], and can be chemically functionalized to provide desired properties [102]. They are used in various applications such as fillers in composite materials to improve their mechanical properties [103] or to render them electrically conductive [104], and even as a promising more energy-efficient alternative for silicon in transistors for computers [105]. Furthermore, to be used as electrodes in nerve interfacing, CNTs exhibit superior properties compared to conventional metal electrodes such as high specific capacitance [73, 106], a larger water window [107–109] and present a desirable surface for cell adhesion [110, 74].

In order to farbicate CNTs, mainly laser ablation, arc-discharge, or chemical vapor deposition are used [111]. CNTs are considered as a promising material for biomedical applications, however, their biocompatibility is still under discussion [112–116].

2.7.2 POLY(3,4-ETHYLENEDIOXYTHIOPHENE) POLYSTYRENE SULFONATE

Conductive polymers are promising materials as electrodes for neural interfacing applications [117]. Either used as coatings for metallic electrodes or as electrodes directly,

they exhibit low impedance and large charge storage capabilities [118, 119]. Among them, poly(3,4-ethylenedioxythophene) polystyrene sulfonate (PEDOT:PSS) is widely used in literature [120, 121]. Even though it shows remarkable efficiency in neural recording and stimulation, its mechanical stability in neural stimulation presents several issues [122, 119]. However, strategies to overcome these were already reported [123, 124]. In this work, it is used as an intermediate layer between carbon nanotubes and an Au coating.

CHAPTER 3

EXPERIMENTAL PROCEDURES

3.1 FABRICATION METHODS

3.1.1 PDMS SUBSTRATE PREPARATION

Glass slides were rinsed with isopropanol and dried with pressurized air. PDMS (Sylgard 184, Dow Corning, USA) was prepared by vigorously stirring a 10:1 (w:w) base to curing agent mixture for $2\,\mathrm{min}$ and degassing it for $20\,\mathrm{min}$ under vacuum (N816.1.2 KN.45.18/M37, IP20, 0.5 bar, KNF Neuberger, Germany). A PDMS layer was spun on the glass slides at $1000\,\mathrm{rpm}$ for $30\,\mathrm{s}$ and cured at $65\,^{\circ}\mathrm{C}$ for $4\,\mathrm{h}$ in an oven. The PDMS layers were left on the glass slides until the end of the entire fabrication. For direct inkjet printing the surface of the samples was either exposed to an O_2-plasma or a (3-mercaptopropyl)trimethoxysilane (MPTMS $95\,\%$, Sigma-Aldrich) treatment. The O_2-plasma treatment parameters were $20\,\mathrm{W}$, $0.9\,\mathrm{mbar}$ and $30\,\mathrm{s}$. MPTMS treatment was carried out as described in [125]. In short, $0.5\,\mathrm{mL}$ of MPTMS was mixed with $100\,\mathrm{mL}$ ethanol to yield a 1:200 (v:v) mixture. The PDMS samples were immersed into this mixture and left there for one hour. Later they were rinsed with ethanol and dried with pressurized air. Next, they were immersed into $0.1\,\mathrm{M}$ HCl for one hour, followed by rinsing with de-ionized (DI) water and drying by pressurized air again.

3.1.2 INKJET PRINTING

The prints were performed with an inkjet printer (CeraPrinter F-Serie, Ceradrop, Limoges, France), which comprises a piezoelectric transducer driven printhead, that can control cartridges with up to 16 nozzles. As the conductive ink, a silver nanoparticle (AgNP) dispersion (736465, Sigma-Aldrich, St. Louis, Missouri, USA, 30–35 $\mathrm{wt.\%}$ in triethylene glycol monomethyl ether, spec. resistivity $11\,\mu\Omega\,\mathrm{cm}$) was filled into a $10\,\mathrm{pL}$ cartridge (DMC-11610, Fujifilm Dimatix Inc,

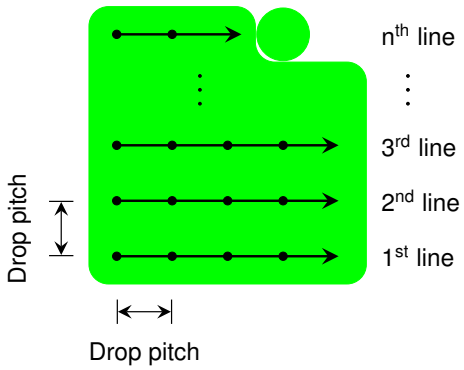

Figure 3.1: Schematic of print direction. Droplets are deposited horizontally from left to right. The layer is printed from bottom to top.

Santa Clara, USA). After a cartridge was fixed into the cartridge holder of the printhead, the nozzles and the chuck, where the sample was placed, were heated up to $55\,^{\circ}\mathrm{C}$. A bipolar waveform as seen in Figure 2.4 was developed according to the principles described in subsection 2.1.2 and applied at the cartridge. Shortly, the dwell time of the jetting pulse was adjusted until the maximum velocity of the droplets was achieved. In this way, the fundamental frequency of the ink channel was found to be approximately $T_\mathrm{f} = 8\,\mu\mathrm{s}$. The waveform parameters (amplitude, dwell time, time for rising/falling edges) were calculated according to the given equations and later slightly changed for the jetting pulse in order to adjust the jetting behavior. The amplitudes of the jetting pulse and of the quenching pulse were altered, until consistent droplets with a sufficiently high velocity were obtained.

All structures were printed in a square lattice, in which the ejection frequency was always set to $2\,\mathrm{kHz}$ and the overlap of the splats was determined by filling tests of $4 \times 4\,\mathrm{mm}^2$-sized test squares. Before the filling tests, the diameters of 5–10 splats were measured, their mean was calculated and rounded to an integer multiple of $5\,\mu\mathrm{m}$ and set as the splat diameter for the print of the structure of interest. The velocity of the printhead was calculated according to set splat diameter, splat overlap and the ejection frequency by the software of the printer. As can be seen in Figure 3.1, the layers were printed by horizontally deposited rows from bottom to top. The overlap of adjacent splats in both, horizontal and vertical directions was always set as the same. The working distance from the nozzle plate to the substrate surface was always set as $500\,\mu\mathrm{m}$.

3.1.3 SINTERING OF THE AGNP PATTERN

Once the print of the AgNP pattern was finished it was left on the chuck until the solvents evaporated and the pattern was optically dry. Next, they sample was placed in an oven at $65\,^{\circ}\mathrm{C}$ for $30\,\mathrm{min}$ for further evaporation of the solvent residuals. This was followed by sintering the silver pattern in an oven at $150\,^{\circ}\mathrm{C}$ for $30\,\mathrm{min}$ if not stated otherwise.

3.1.4 BONDING OF AN INSULATING PDMS LAYER

For the inkjet printed samples an insulating PDMS layer was bonded via O_2-plasma on the printed PDMS surface. First, another PDMS surface was prepared as described in subsection 3.1.1 except the surface treatments. Next, $\approx 2\,\mathrm{mm}$ of the rim was removed by a razor blase in order to avoid any rupture while peeling off the PDMS layer from the glass slide. In addition to that, the length of the PDMS slab to be peeled off was adjusted to fit the printed AgNP pattern such that after bonding it leaves one end of the conductors open to serve as electrodes and the other end open to serve as contact pads. Afterwards, the sample was exposed together with the printed PDMS sample to O_2-plasma at $20\,\mathrm{W}$ and $2.9\,\mathrm{mbar}$ for $30\,\mathrm{s}$. Immediately after the surface treatment, both samples were dipped shortly in ethanol and the insulating PDMS layer was peeled off the glass slide and placed on top of the printed PDMS surface such that the treated surfaces came into contact.

3.1.5 PREPARING AND SCREEN-PRINTING OF THE PDMS-MWCNT COMPOSITE

The preparation of the composite was adopted from [126] and the screen-printing of it was adopted from [56]. First, a few samples with an inkjet printed AgNP serpentine pattern on an O_2-plasma treated PDMS surface were prepared as decribed in subsection 3.1.1 and subsection 3.1.2 ($100\,\mu\mathrm{m}$ splat diameter and $40\,\%$ overlap). Next, two PDMS layers were prepared as described in subsection 3.1.1 and cut to dimensions a little larger than the desired insulation layer. Both layers were detached from the glass carrier, dipped shorty into ethanol and both were put on top of each other on a polyethylene naphthalate (PEN) foil. The foil was placed on a PDMS layer with a AgNP serpentine pattern and a gauge 19 blunt needle was used to pierce the electrode openings into the two double-layered PDMS slab while the AgNP pattern beneath was used to determine the desired positions of the electrode openings. In this step, the small circular double-layered PDMS slab stuck to the needle and an opening was formed into the insulation layer. Next, the double-layered PDMS slab and another AgNP patterned PDMS layer were exposed to O_2-plasma and bonded to each other as described in subsection 3.1.4 while aligning the electrode openings to the desired positions. Directly after the O_2-plasma exposure and before the bonding,

the circumference of the double-layered slab was cut again, but this time to the actual desired dimensions of the insulation layer. This additional cutting of the circumference was to avoid any bonding of the edges of the two unpatterned layers to each other since one of them will be removed in a later step.

Parallel to that, the PDMS-multiwalled carbon nanotubes (PDMS-MWCNT) composite dough was prepared for screen printing. First, multiwalled carbon nanotubes (MWCNTs, Hanos MWCNT M-95, entangled, 93–97 % purity, HanwhaChemical) were dispersed in isopropanol with a 1:100 (w:w) ratio in an ultrasonic bath for 30 min. Next, a low-viscosity silicone fluid ($100\,\mathrm{mm^2\,s^{-1}}$, AK 100, Wacker, Germany) was added to the dispersion in a 2:5 (w:w) MWCNTs to silicone fluid ratio and ultrasonicated for 10 min. Afterwards, PDMS base only (Sylgard 184, Dow Corning, USA) was added in a 1:4 (w:w) silicone fluid to PDMS base ratio and ultrasonicated for another 10 min. The mixture was placed on a hot plate at 55 °C for at least 12 h until the isopropanol evaporated. The final weight of the mixture was weight to ensure no isopropanol remained. Following that, the PDMS curing agent was added in a 10:1 (w:w) base to curing agent ratio to the resulting dough and mixed and degassed as described in subsection 3.1.1.

In the final step, the dough was smeared and pushed into the electrode openings. The upper PDMS layer, which was not O_2-plasma bonded to the layer beneath was peeled off in order to remove the excess of the dough from the circumference of the electrode opening. However, since more than the expected amount of the dough remained on top of the electrode, the excess had to be removed by sliding over the surface with the edge of a glass slide. Finally, the sample was put into an oven at 80 °C for 2 h to cure the PDMS-MWCNT dough.

3.1.6 MOLDING PDMS BODY AROUND AGNP PATTERN ON PEN FOIL

First, AgNP electrode patters were printed on a polyethylene naphthalate substrate (Teonex Q65HA, Teijin DuPont Films, Wilmington, Delware, USA, 50 µm thickness) substrate as described in subsection 3.1.2 with a drop spacing of 35 µm and were sintered at 150 °C for one hour. Afterwards, they were cut to the desired dimensions with scissors by the aid of cutting marks included into the print file.

The mold halves were printed with the resin UV-curable resin (FREEPRINT®splint, 405 nm, Detax, Germany) in a stereolithographic printer (MiiCraft 50X, wavelength 365 nm, maximum irradiance $6.2\,\mathrm{mW\,cm^{-2}}$, MiiCraft, Taiwan). They were designed in the CAD software Solidworks 2018 (Dassault Systemes, France). The CAD files were sliced into layers of 50 µm height by using the printer's software. All structures defining the body of the final nerve interface and the electrode area were included into the layers which were printed last. The print

settings were as follows: $250\,\%$ power for $30\,\mathrm{s}$ for the first layer, in order to achieve a good adhesion between the structure and moving platform, $250\,\%$ power for $3.25\,\mathrm{s}$ for all other layers.

Once the print finished, the mold halves were scraped off the moving platform with a cardboard cutter and rinsed with isopropanol. Next, they were immersed in isopropanol, ultrasonicated for $5\,\mathrm{min}$, rinsed again with isopropanol and dried with pressurized air. Afterwards, they were put into an oven at $40\,^{\circ}\mathrm{C}$ for $30\,\mathrm{min}$. This was followed by an exposure to 4000 flashes in an UV chamber (Otoflash G171, NK Optik, Baierbrunn, Germany) under nitrogen influx. As a final step, the mold halves were immersed in a $10\,\mathrm{wt.\%}$ sodium dodecyl sulfate (SDS) solution for one hour. Afterwards, they were dipped shortly in de-ionized (DI) water and left for drying for $30\,\mathrm{min}$. The remaining water was blown away with pressurized air.

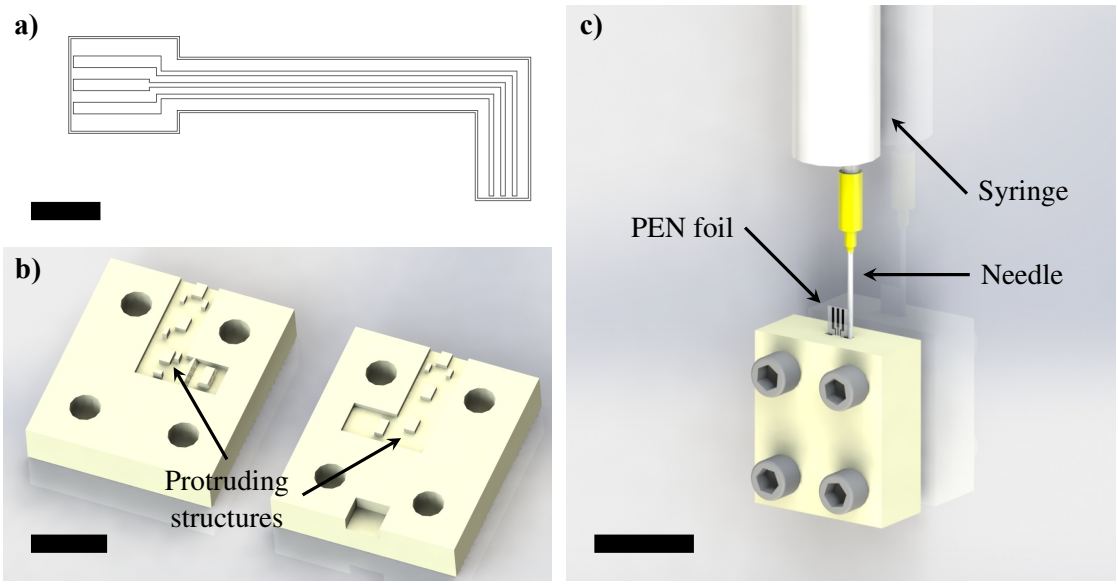

Figure 3.2: **a)** Layout of the electrode pattern for inkjet printing. The outer line is an aid for cutting the foil to the desired dimensions. Scale bar is $3\,\mathrm{mm}$. **b)** Schematic illustration of the mold halves. The protruding structures are there to hold the PEN foil in the middle of the mold when it is closed and filled with PDMS. Scale bar is $1\,\mathrm{cm}$. **c)** Schematic illustration of how the printed PEN foil is fixed into the mold and how the mold is filled with PDMS by a syringe. Scale bar is $3\,\mathrm{cm}$.

The printed foils were placed into one of the mold halves so that the protruding structures in the mold as seen in Figure 3.2 b could hold the sides and the edges of the foil equally spaced to the inner surfaces of the mold. Then the mold halves were closed and fixed with M4 screws. PDMS was prepared as described in the beginning of subsection 3.1.1 and filled into a syringe with a gauge 20 needle at its tip. The needle was inserted into the closed mold as seen in Figure 3.2 c until its tip hit the bottom. Then, the PDMS was injected slowly into the mold while the needle was drawn out at the same time, until the PDMS filled the mold entirely. Next,

the mold was put into an oven at $150\,°\mathrm{C}$ for $15\,\mathrm{min}$. The mold was left for at least one hour to cool down before opening it and detaching the cured PDMS body.

3.1.7 AU ELECTRODEPOSITION ON ELECTRODES

For AgNP electrodes on PEN substrates, the samples insulated either with a PDMS body as described in subsection 3.1.6 or with Kapton tape (VWR, Germany) on their feedlines, were attached to a commercial flexible printed circuit (FPC) connector (522070333, Molex, USA) from their contact pads. Since the PEN foil on which the AgNP pattern was printed was too thin to be clamped by the FPC connector, another thicker foil ($175\,\mu\mathrm{m}$) was clamped in parallel to press the AgNP contact pads tightly against the contacts of the connector. The entire electrode area was immersed into an aqueous potassium gold cyanide bath ($KAu[CN]_2$, Pur-A-Gold 401B, Enthone-OMI, 's-Hertogenbosch, Netherlands). The $KAu[CN]_2$ had a pH of 5.80–5.85 and a conductivity of 10.1–$10.2\,\mathrm{S\,m^{-1}}$ [127]. For the Au electrodeposition, chronoamperometry was performed in a three electrode setup by using the AgNP electrode as the working electrode, a Ag/AgCl reference electrode ($3\,\mathrm{M}$ NaCl, RE-6, BASi, West Lafayette, USA), a large Pt counter electrode and a potentiostat (PalmSens4, Houton, The Netherlands). A constant potential of $-1\,\mathrm{V}$ vs Ag/AgCl was applied for $90\,\mathrm{s}$ at the working electrode.

For CNT/PDMS test lines, the same procedure as described above was conducted with the only difference that the deposition duration was $15\,\mathrm{min}$. In total $n = 12$ samples were prepared which were divided into three equally sized groups. While Au was directly deposited on the samples in the first group, the samples in the second group were immersed into ethylene glycol for $2\,\mathrm{h}$ and rinsed by dipping them into the same DI-water bath for three times prior to Au deposition. The samples in the third group were immersed into a PEDOT:PSS solution (Clevios PH1000, Heraeus, Germany) in a three electrode setup as described above and a potential of $0.8\,\mathrm{V}$ vs Ag/AgCl was applied on the test lines for $10\,\mathrm{min}$ prior to Au deposition.

3.1.8 CNT/PDMS ELECTRODE FABRICATION

Filter membranes (Durapore, $0.22\,\mu\mathrm{m}$ pore size, polyvinylidene fluoride (PVDF) membrane, $\varnothing 47\,\mathrm{mm}$, hydrophilic, nonsterile) were patterned with the negative structure of the desired electrode layout by a wax printer (Xerox, ColorQube 8900). Afterward, they were wetted with deionized (DI) water from both sides and attached to a vacuum filtration setup. A CNT dispersion was prepared with $1.43\,\mathrm{mg}$ CNTs (Hanos MWCNT M-95, entangled, 93–$97\,\%$ purity, Hanwha Chemical), $16\,\mathrm{mg}$ sodium dodecyl sulfate (SDS) (BioChemica, A2573.0250, pH = $5.0 - 7.0$), and $100\,\mathrm{ml}$ DI water. The CNT amount was defined by the area of the targeted electrode design to yield a surface concentration of $1.33\,\mathrm{mg\,cm^{-2}}$ after filtration. An ultrasonic homogenizer

(generator: GM 2200.2, transducer: UW 2200, booster: SH213, sonotrode: KE76, Bandelin, Germany) was used at $40\,\%$ power for $5\,\mathrm{min}$ continuously to disperse the CNTs in the solvent. Subsequently, the dispersion was filtered through the patterned filter membrane to achieve a homogeneous CNT pattern on the wax-free areas of the membrane. The vacuum for the filtration was applied by a pump (MD 1, $1.5\,\mathrm{mbar}$, Vacuubrand GmbH+CoKG, Germany). The membranes were left to dry for at least $16\,\mathrm{h}$. Afterward, they were dipped into acetone four times with breaks of $5\,\mathrm{min}$ in between each step. This step removed the wax pattern and residual CNTs, which were not captured in the defined areas but adhered to the wax pattern. Before the next step, the membrane was left to dry for at least one hour. Meanwhile, a glass slide was cleaned with isopropanol and dried with pressurized air. PDMS (Sylgard 184) was prepared similar as described in subsection 3.1.1. Two layers of PDMS were spun on the glass slides. While the first layer was cured entirely ($100\,^{\circ}\mathrm{C}$) in an oven, the second layer was semi-cured at $65\,^{\circ}\mathrm{C}$ for $15\,\mathrm{min}$ on a precision hot plate (PR 5-3T, Harry Gestigkeit, Germany). Subsequently, the CNT pattern on the filter membrane was pressed on the semi-cured PDMS layer, and the sample was cured in an oven at $100\,^{\circ}\mathrm{C}$ for $1\,\mathrm{h}$. Afterward, the membrane was soaked with DI water for $2\,\mathrm{min}$ and manually detached leaving the CNT pattern embedded into the silicone surface.

For the electrical insulation layer, two different approaches were used. In the first one, a $175\,\mu\mathrm{m}$ thick PET foil was cut to the desired dimensions and left in a $10\,\mathrm{wt.}\%$ SDS solution for $24\,\mathrm{h}$. The foil was dipped two times in DI water and dried by pressurized air. Another PDMS layer (mixed and degassed as mentioned above) was prepared by spin coating ($1000\,\mathrm{rpm}$, $150\,\mathrm{s}$) on the PET foil. The foil was attached to a custom-made fineplacer with the PDMS-coated surface facing the embedded CNT pattern. It was aligned onto the CNT pattern such that only electrode openings and contact pads were not covered with the PDMS layer. After placement, the sample was put into a degassing chamber for $20\,\mathrm{min}$ and subsequently cured at $150\,^{\circ}\mathrm{C}$ for $1\,\mathrm{h}$. Finally, the foil was detached and the silicone probes were cut to the desired layout before detaching the samples from the glass surface. The complete fabrication process is illustrated schematically in Figure 3.3.

For the second fabrication approach of the electrical insulation layer, PDMS was deposited on top of the CNT/PDMS structures by extrusion printing. The printer was a custom assembly as described in the following (Figure 3.4 a). An adapter was printed with a 3D printer as described in subsection 3.1.6, which was used to connect a push-in-fitting (QS-1/8-6, Festo, Germany) to a $3\,\mathrm{ml}$ syringe (Omnifix Luer Lock Solo, $3\,\mathrm{ml}$, B.Braun Melsungen, Germany) with Luer-Lock tip and to connect the extrusion print head to the moving stage of a 3-axis robot (Microplotter II, Sonoplot, USA). A $\varnothing 6\,\mathrm{mm}$ hose was connected from one side to the push-in fitting and from the other side to a pressure controller (OB1 MK3+, Elveflow, France). Finally, a 27G blunt needle (Sterican, $0.40\,\mathrm{mm}\times 25\,\mathrm{mm}$, B.Braun Melsungen, Germany) was connected to the syringe. For

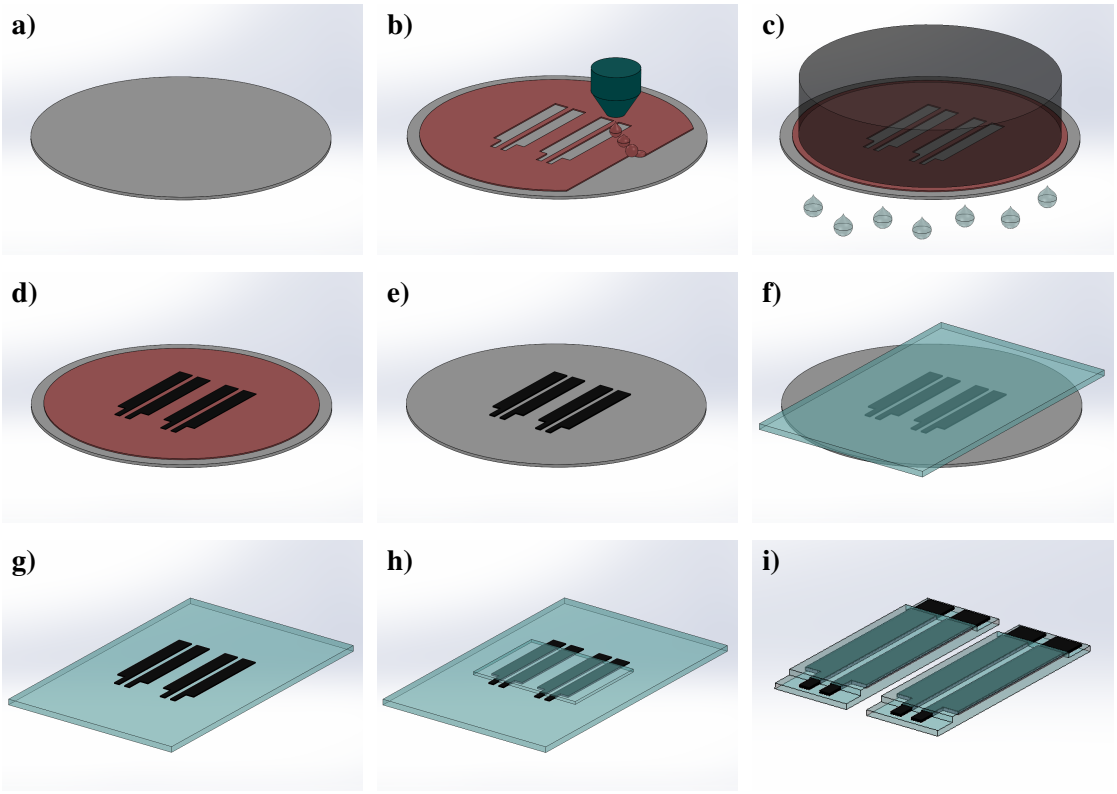

Figure 3.3: Fabrication procedure of embedding CNTs into PDMS. **a)** and **b)** A pattern is printed on a blank filter membrane. **c)** and **d)** Vacuum filtration of a CNT-SDS-DI water dispersion through the wax-free areas of the membrane. **e)** The wax pattern is dissolved by acetone. **f)** The CNT pattern is contacted with a semi-cured layer of PDMS. **g)** The filter membrane is detached after fully curing the PDMS layer. **h)** A PDMS top insulation is applied. **i)** The samples are cut and detached from the glass carrier.

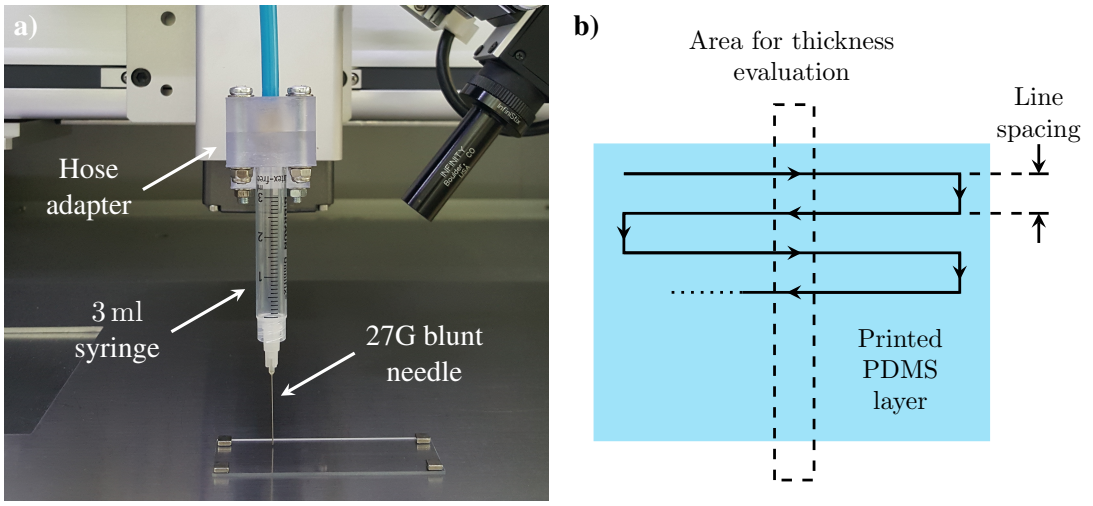

Figure 3.4: a) Silicone extrusion printing head. Assembly shows a 3 ml syringe with Luer-Lock tip, a 27G blunt needle, and an adapter to connect a push-in fitting for a 6 mm hose to the syringe and the entire assembly to the 3-axis robot's moving head. **b)** Schematic to illustrate the printing approach and the areas which were used to evaluate the thickness of the printed layer. The solid black line with the arrows depicts the movement pattern of the print head to extrude the silicone layer.

printing, PDMS was prepared as described in subsection 3.1.1 and filled into the syringe, before the syringe was placed into the adapter. Next, the robot's software was used to approach the tip of the blunt needle to the surface of the CNT/PDMS structures until it touched a CNT free area. Then the tip was increased by 200 µm and the print head followed the pattern shown in Figure 3.4 b on the XY-plane. During the print, the robot's moving stage had a velocity of $2\,\mathrm{mm\,s^{-1}}$ and an acceleration of $100\,\mathrm{mm\,s^{-2}}$. The pressure to extrude the silicone out of the syringe was set to 1.2 bar. The thickness of the insulation layer was defined by the center-to-center distance between adjacent printed lines (Figure 3.4 b, line spacing), which were always perpendicular to the length of the CNT conductors. For the final samples described in subsection 4.2.4, a line spacing of 300 µm was used. The printed layer covered the entire CNT pattern except an area of $3\,\mathrm{mm} \times 0.5\,\mathrm{mm}$ at the thicker end of the lines to form the contact pads. The print was performed within 30 min after degassing. In case this time duration would have exceeded during the print, fresh silicone was prepared. After the print, the silicone layer was cured in an oven at 150 °C for 1 h. To obtain the electrodes, the samples were cut at the middle of the thinner parts of the array design perpendicular to the length of the conductors by a razor blade (Figure 3.5).

Images of the samples were made by a stereomicroscope (Stemi 2000-C, Carl Zeiss, Germany) and a camera (EOS 8000D, Canon, Japan) with a microscope adapter (NY1XS, Mecan, Japan). The thickness of the PDMS substrate and electrical insulation layer were determined with a 3D laser scanning confocal microscope (VK-x250, Keyence, Japan). In order to deter-

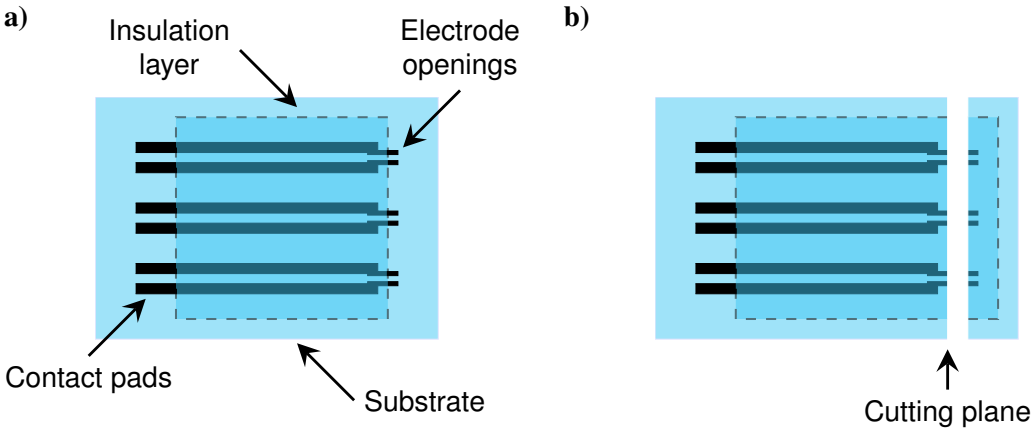

Figure 3.5: Schematic illustration of the two different approaches used to fabricate the electrical insulation. **a)** The insulation layer is fabricated by spin-coating PDMS on a plastic foil with a certain area and placed on top of the sample such it leaves both ends of the CNT conductors open so that one end is the contact pad and the other the electrode. **b)** The insulation layer is printed over the entire CNT electrode array pattern except the contact pads. Afterward, the sample is cut so that the cross-section of the tip of the conductors is used as the electrode.

mine the conductivity of the CNT conductors, samples were cut perpendicular to the length of the conductors, and their cross section was imaged in a scanning electron microscope (JSM-6060LV, JEOL, Japan) with an acceleration voltage of $10\,\mathrm{kV}$ at a magnification of $120\times$. The cross-sectional area of the CNT conductors was evaluated with the software Fiji. All mechanical, electrical and electrochemical properties presented, were evaluated with samples whose electrical insulation layer was manufactured with the first approach described above.

For interfacing with the leech, a thread was immersed in PDMS (mixed and degassed as mentioned above) and glued onto the back side of the CNT/PDMS electodes along the CNT conductors. The other end of the thread was attached to a surgical needle for suturing.

3.1.9 FORMING THE CUFF MECHANISM AROUND THE CNT/PDMS ELECTRODES

Molds were designed, printed and post-processed similar as described in subsection 3.1.6 with the difference of using another UV-curable resin (Medicalprint®clear & opaque, 378–388 nm, Detax, Germany). Also the settings of the printer were different: $150\,\%$ power for $3\,\mathrm{s}$ for the base layer and $150\,\%$ power for $1\,\mathrm{s}$ for the remaining layers of the sliced structure. Other differences were that after the exposure to UV light in the otoflash, the mold halves were placed again in an oven, but this time at $80\,^{\circ}\mathrm{C}$ for at least $48\,\mathrm{h}$ and that the injected silicone was cured at $65\,^{\circ}\mathrm{C}$ for at least $12\,\mathrm{h}$. The mold designs can be found in the appendix Figure 5. Beside

a silicone inlet, silicone outlets were included in the designs to avoid any entrapped air bubbles from preventing the silicone to fill the enclosed volume (appendix Figure 7). In one of the molds four channels were designed into which silk threads attached to a surgical needle (SERAFLEX Black, EP1 (5/0), $1 \times 0.75\,\mathrm{m}$, needle HR-17) were placed. This was done by placing the threads roughly to the designated channels and then fastening both mold halves with screws. The pressure applied with the screws was such that the threads could be drawn in between both mold halves until they moved into the channels. Afterward, the screws were fastened tightly. In that design, the four channels for the silk thread were at the same time the outlets for the entrapped air. After molding the silicone parts, they were separated from the silicone structures formed by the inlet and outlets of the molds and from each other with a razor blade. Before attaching the molded parts to the CNT/PDMS electrode array, the electrodes were created first. For this, first the electrical insulation layer was printed on top of the embedded CNT pattern as described in the subsection 3.1.8 and then the sample was cut perpendicular to the length of the array pattern. Next, the CNT/PDMS electrode array was bonded to the molded silicone part comprising the silk thread with O_2-plasma with the parameters given in subsection 3.1.4. Attention was given that the contact pads of the CNT/PDMS electrode array and the rippled part of the silicone structure were facing downward, so that the surfaces which should be be in touch together in the next step were entirely exposed to O_2-plasma. After having waited for at least $12\,\mathrm{h}$, the process was repeated with the other silicone structure, while attention was given that again the respective surfaces going to be in touch were facing upward during surface treatment.

3.1.10 FORMING THE CONNECTION BETWEEN THE CONTACT PADS AND THE ELECTRONICS

Two structures, which could be clipped together (appendix Figure 4) and two molds (appendix Figure 6), were designed, printed, and post-processed as described in subsection 3.1.9. The only difference was that the two clip parts were not immersed in a SDS solution. Next, two PTFE coated Cu wires with a diameter of $100\,\mu\mathrm{m}$ were wrapped around a $40\,\mathrm{mm}$ long G27 needle which was then placed into a mold which was designed to hold the needle from both ends (appendix Figure 6 c and d). One of the mold halves comprised outlet channels for the Cu wires. They were designed close to the grooves holding the needle. So the ends of the Cu wires which were not wrapped around the needle could be led through those channels. They served at the same time as silicone outlet channels. Next, the mold halves were fastened, the needle was carefully pulled out of the mold and silicone was injected into the mold and cured as described in subsection 3.1.9. Afterward, both ends of the wires which were not embedded into silicone were coated with tin solder. The wire ends from one side were wrapped around the

larger clip part so that they did not touch each other. Next, both clip parts were fastened around the contact pads by using a 3D printed alignment aid which was printed using the same resin and printing parameters as for the clip parts. Attention was paid that the clip part around which the Cu wires were wrapped was placed on top of the contact pads. Finally, the clip was encapsulated with silicone by using another mold (appendix Figure 6 a and b) and by using the same molding parameters as described in subsection 3.1.9. The wire ends on the other side were soldered to stranded wires with a soft and flexible silicone encapsulation (24 AWG, Haerkn, China) which were also encapsulated with silicone by using a third mold. The mold fabrication and molding parameters were the same as described above for the other molded parts.

3.2 MECHANICAL AND ELECTROCHEMICAL CHARACTERIZATION

3.2.1 STRAIN TESTS

For the mechanical characterization of the CNT conductors, samples with a $20\,\mathrm{mm}$ long and a $0.6\,\mathrm{mm}$ wide CNT/PDMS pattern were attached to a custom-made stretcher and stretched between $0\,\%$ and $20\,\%$ strain in a cyclic manner. The stretching speed was set to $0.5\,\mathrm{mm\,s^{-1}}$. The resistance of the CNT conductors was measured after 1, 10, 100, and 1000 and after every additional 1000 cycles until 10000 cycles were completed. Furthermore, a sequence of cycles was applied up to a total strain of $80\,\%$. The resistance of the samples was measured after each cycle. The mechanical characterization was performed on $n = 6$ conductors, and the reported values indicate the mean $\pm$ standard deviation.

3.2.2 CYCLIC VOLTAMMETRY AND IMPEDANCE SPECTROSCOPY

If not mentioned otherwise, cyclic voltammetry (CV) and impedance spectroscopy measurements were performed in phosphate buffered saline (Dulbecco's PBS, pH= 7, ρ =$0.63\,\Omega\,\mathrm{m}$, D8662, Sigma-Aldrich). Both measurements were performed in a three electrode setup with the fabricated electrode as the working electrode, a Ag/AgCl reference electrode ($3\,\mathrm{M}$ NaCl, RE-6, BASi, West Lafayette, USA), a large-area Pt wire as a counter electrode, and a potentiostat (PalmSens4, The Netherlands). Cyclic voltammetry was applied in different ranges for different electrode materials and for different purposes: A scan range between $-0.65\,\mathrm{V}$ and $0.80\,\mathrm{V}$ vs Ag/AgCl at $100\,\mathrm{mV\,s^{-1}}$ to precondition the Au coated AgNP electrodes. The following three ranges were applied for the CNT/PDMS electrodes: A scan range between $-2.5\,\mathrm{V}$ and $2.5\,\mathrm{V}$

vs Ag/AgCl at $100\,\mathrm{mV\,s^{-1}}$ for three cycles in order to determine the water oxidation and reduction limits of the CNT/PDMS electrodes and to activate the electrode surface. A scan range between $-1\,\mathrm{V}$ and $1\,\mathrm{V}$ vs Ag/AgCl at $100\,\mathrm{mV\,s^{-1}}$ was applied for ten cycles in order to precondition the surface before performing an electrochemical impedance spectroscopy measurement. A scan range between $-0.1\,\mathrm{V}$ and $0.1\,\mathrm{V}$ vs Ag/AgCl at $10\,\mathrm{mV\,s^{-1}}$ was applied to measure the surface double layer capacitance. The specific capacitance was determined by the formula $c_\mathrm{s} = (|i_\mathrm{cath}| + i_\mathrm{anod})/(2v_\mathrm{s}A)$, where i_cath and i_anod are the cathodic and the anodic current in A at $0\,\mathrm{V}$ vs Ag/AgCl, respectively, v_s is the scan rate in $\mathrm{V\,s^{-1}}$, and A is the electrode area in $\mathrm{m^2}$. In all CVs, the start and finish potential was set to $0\,\mathrm{V}$ vs Ag/AgCl, and the measurement started with a negative sweeping direction. The impedance data were recorded applying a signal of $10\,\mathrm{mV}$ (rms, $\approx 28.2\,\mathrm{mV}$ peak-to-peak). For comparison, the low-frequency regime of the impedance data (below $20\,\mathrm{Hz}$) of the CNT/PDMS electrodes was fitted to a simplified Randles circuit neglecting the Warburg element.

3.2.3 CONTSTANT CURRENT PULSING AND ELECTRODE POLARIZATION

For Au coated AgNP electrodes constant current pulsing was performed in a three electrode setup by using a potentiostat as described in the previous section. A constant current train consisted of 20 cathodic first biphasic pulses with a phase and interphase duration of each $2\,\mathrm{ms}$. The duration in between two consecutive pulses was $5\,\mathrm{s}$. The amplitude of the pulses was constant within the pulse train and was varied for each electrode.

In order to determine the charge injection capacity (CIC) of the CNT/PDMS electrodes and to perform the long-term stimulation experiments on them, pairs of electrodes on the same electrode array with similar surface area and impedance were characterized. A self-made constant-current source was used to apply stimulation pulses, and the polarization of both electrodes was measured with an oscilloscope (InfiniiVision DSOX2024A, $200\,\mathrm{MHz}$, $2\,\mathrm{GSa\,s^{-1}}$, Keysight, USA). A biphasic (cathodic first), charge-balanced current-controlled pulse of $200\,\mu\mathrm{m}$ phase duration and $20\,\mu\mathrm{s}$ interphase delay was applied through both electrodes. The amplitude of the signal was increased until the polarization of each electrode reached $\Delta\varphi_\mathrm{el} \approx 1\,\mathrm{V}$. The polarization was obtained by the formula $\Delta\varphi_\mathrm{el} = (\Delta\varphi_\mathrm{tot} - \Delta\varphi_\mathrm{s})/2$, where $\Delta\varphi_\mathrm{tot}$ is the total measured potential difference before and at the end of the cathodic pulse and $\Delta\varphi_\mathrm{s}$ is the voltage drop over the solution resistance. The CIC was determined by the formula $CIC = Q/A$, where Q is the charge passed through both electrodes during one phase and A is given by the average area of both electrodes.

The long-term stability upon periodic pulsing was determined by applying continuous pulses through each pair of electrodes, which were used to determine the CIC. Using an identical signal

as described above, the current was determined by the mean electrode area of both electrodes and a charge injection limit (CIL) of $32\,\mu\mathrm{C\,cm^{-2}}$. The frequency of the pulse train was $200\,\mathrm{Hz}$, and it was applied for one hour a day. Afterward, an impedance spectrum of both electrodes was recorded separately. In total, this measurement was performed twice a week over a period of three weeks.

3.3 *In Vivo* EXPERIMENT

3.3.1 SURGERY

Before the experiment, the leeches (Blutegelapotheke Biebertal, Germany) were kept in tap water (chlorine-free), which was obtained by letting the tap water rest for at least $48\,\mathrm{h}$ under ambient conditions. They were stored isolated from light and kept in a fridge at $10\,^{\circ}\mathrm{C}$. Their water was changed once a week by replacing half of the amount with fresh water. Prior to surgery, the leech was anesthetized by submersion into ice water for $\approx 20\,\mathrm{min}$, rendering them easier to handle. Then, the leech was pinned down on both ends and the middle with its ventral side facing upwards. Throughout the experiment, the leech was wetted several times with cold Ringer solution ($115.3\,\mathrm{mM}$ NaCl, $1.8\,\mathrm{mM}$ $CaCl_2$, $4.0\,\mathrm{mM}$ KCl, $10\,\mathrm{mM}$ Tris/maleic acid or HEPES). A small longitudinal incision centered over the ventral midline of the leech was made. The skin and the muscle layers were carefully separated until the nerve cord was exposed. Next, the black sheath surrounding the nerve was cut but not separated, leaving the nerve exposed from above.

The surgical needle that was attached to the nerve interface by a thread was inserted between the nerve cord and the surrounding sheath. Afterward, the thread was used to pull the electrode directly below the nerve to form a tight contact. The other end of the nerve interface was connected to a custom-made holder via a FPC connector (2005280040, Molex, USA). A large-area Pt wire, which was immersed in 2–$3\,\mathrm{cm}$ proximity to the CNT/PDMS electrodes in the Ringer solution, served as the counter electrode.

3.3.2 STIMULATION TEST

The stimulation was performed using trains of charge-balanced biphasic current pulses (cathodic phase first) applied through the CNT/PDMS working and the Pt counter electrode. Each phase had a duration of $200\,\mu\mathrm{s}$, an interphase delay and an interpulse delay of $75\,\mu\mathrm{s}$. The pulse trains consisted of an integer multiple of 100 biphasic pulses. The number of pulse trains and the amplitudes were adjusted until a contraction of the leech could be observed. At the same time, the potential difference between the CNT/PDMS stimulation electrode and the Pt counter

electrode was measured via an oscilloscope, as described for the electrode characterization. During the amplitude adjustment, attention was given not to exceed the water window of the CNT/PDMS electrodes.

CHAPTER 4

RESULTS AND DISCUSSION

This section presents the results obtained during manufacturing a soft peripheral nerve interface. It starts with the results of the first attempt, which was to use inkjet printing to fabricate the electrodes and conductors of the interface and next, it explains the second approach in which a wax pattern assisted filtration method was used to embed carbon nanotubes as electrodes and conductors into the body of PDMS.

4.1 INKJET PRINTED NERVE INTERFACE

In this section, first the results of directly printing with a silver nanoparticle ink on a PDMS substrate and the associated challenges are described. Next, the results of taking an alternative route by inkjet printing with the same ink on a polyethylene naphtalate substrate and the challenges with this approach will be presented.

4.1.1 SILVER NANOPARTICLE PATTERNS PRINTED ON PDMS

In order to fabricate a soft nerve interface a conductor must be encapsulated with a soft electrical insulation layer. Both ends of the conductor must be left open to have an electrode and a contact pad to connect the electrode to recording or stimulation electronics as can be seen in the schematic illustration in Figure 4.1 a. In this case the conductor was fabricated with silver nanoparticles (AgNP) and the isolator with polydimethylsiloxane (PDMS). In Figure 4.1 b, a serpentine test pattern printed with a silver nanoparticle ink on an O_2-plasma treated PDMS surface can be seen ($100\,\mu\mathrm{m}$ splat diameter and $40\,\%$ overlap). The resistivity of the silver lines was evaluated as $\rho_\mathrm{r} = (34.25 \pm 1.53) \times 10^{-8}\,\Omega\,\mathrm{m}$ ($n = 4$) which is one order of magnitude higher than for bulk silver.

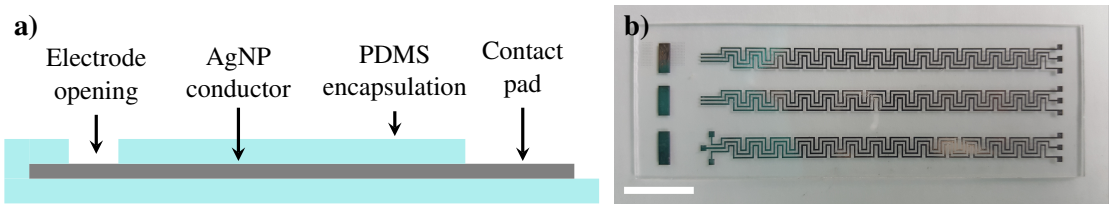

Figure 4.1: a) Schematic illustration of silver nanoparticle pattern in between two PDMS layers, serving as electrical insulation. **b)** Silver pattern printed on an O_2-plasma treated PDMS surface. Scale bar: 1 cm.

Even though the printed AgNP pattern could be contacted for resistance evaluation, the mechanical stability of these AgNP films posed a challenge. Since the metal layer is a thin and solid film on a soft and highly deformable surface, it cracked when it was touched with another solid object such as the metal pins of a connector or the tip of a multimeter probe (Figure 4.2). Such a cracking might lead to failure of the electrical connection in an implantable device when the contact is permanently under stress due to movements in the body.

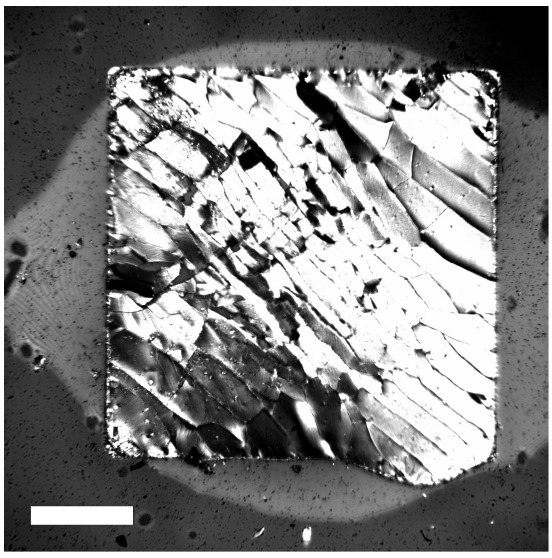

Figure 4.2: Cracking of AgNP pattern on MPTMS treated PDMS surface when touched with a solid object. Scale bar is 250 µm.

In order to realize a reliable connection between the electronics and the contact pads, AgNP conductor patterns were printed on a polyethylene naphthalate (PEN) foil, on which they were mechanically very robust and thus, could be easily connected to a commercial flexible printed circuit board adapter. Next, the other end of AgNP conductor pattern was the attached to the AgNP contact pads on the PDMS via a polyimide tape as can be seen in Figure 4.3. The resistance of two such test lines was evaluated under strain as depicted in Table 4.1. The resistance

Table 4.1: Change in resistance upon stretching two samples as depicted in Figure 4.3. For each sample the resistance change of one serpentine line on top of PDMS is given.

ϵ_s	0 %	1.25 %	2.5 %	3.75 %	5 %
R_{S1}	0.9 kΩ	2 kΩ	3.8 kΩ	7.5 kΩ	3 MΩ
R_{S2}	1 kΩ	1.7 kΩ	3.7 kΩ	170 kΩ	>500 MΩ

values were fully reversible when the strain was released. Usually the resistance of one serpentine line as can be seen in the figure is around 200 Ω when the sample is still on the glass carrier. However, the resistance of the two test lines were increased by almost fivefold when removed from the glass carrier and attached to the PEN foils. This increase might be either due to the mechanical stress induced into the AgNP film by the removal or due to the contact to the AgNP film on the PEN foil, since one of the AgNP lines on the foils had resistance values of only a few Ω. But before further investigating the exact reason of this increase in resistance or applying any improvement strategies on the electrical connection, a first attempt on investigating the electrochemical properties of the electrodes was made.

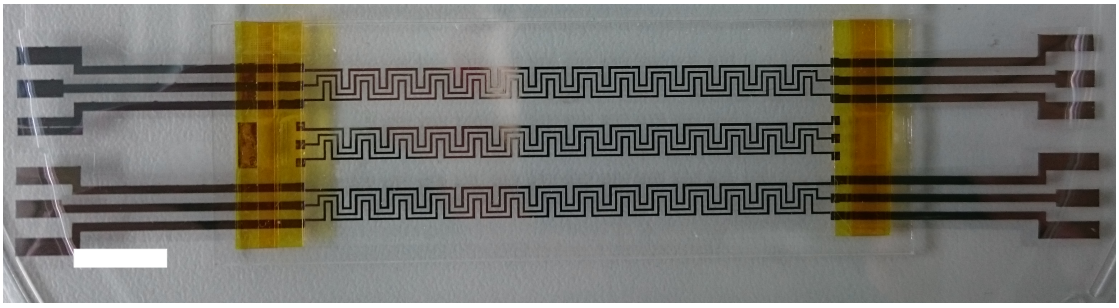

Figure 4.3: Polyethylene naphthalate (PEN) foil printed with AgNP pattern attached onto the AgNP contact pads with polyimide (Kapton) tape. Scale bars is 1 cm.

When a sample as shown in Figure 4.4 a was immersed into phosphate buffered saline (PBS) to carry out an electrochemical characterization by impedance spectroscopy and cyclic voltammetry, the silver pattern turned out to have a weak adhesion to the underlying PDMS substrate in PBS. In Figure 4.4 b, two of the electrodes (the part of the AgNP pattern not covered with an insulating PDMS layer) were detached from the substrate and one electrode was oxidized (lowermost electrode). The oxidation happened during the positive sweep of the cyclic voltammetry measurement to 2 V vs Ag/AgCl.

Since a strong adhesion between the conductor pattern and the underlying substrate is necessary in a salt solution environment, a possible solution to this problem was investigated by

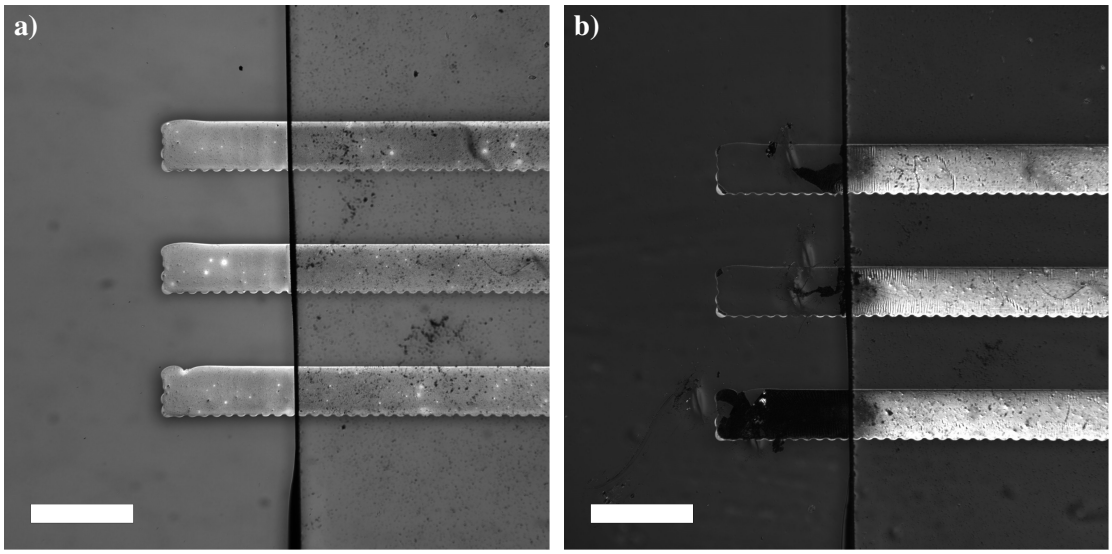

Figure 4.4: Both images show the same three electrodes. On the right side of the images the silver pattern lies in between two PDMS layers, while it is exposed on the left side (the vertical line in the images in the edge of the PDMS insulation layer). The pattern was printed on an O_2-plasma treated PDMS surface. Both images show the same three electrodes. **a)** Before performing a cyclic voltammetry measurement. **b)** After performing a cyclic voltammetry measurement. Both scale bars are $500\,\mu\mathrm{m}$.

surface treatment of the PDMS layer with (3-mercaptopropyl)trimethoxysilane (MPTMS). The use of this material was shown to lead to a good adhesion between PDMS and lithographically structured gold patterns in a dry environment [128] and to inkjet-printed silver and carbon patterns in salt solution [125, 129]. MPTMS has three methoxy ($-OCH_3$) functional end groups and a thiol (SH) functional head group, of which the former can bind to oxide surfaces and the latter to metals. However, even though the same protocol as in [125] was used, the silver pattern did not show a reliable adhesion to the underlying PDMS substrate in PBS as shown in Figure 4.5. The reason for this might be either a weak bond of the functional groups to their targeted materials or that either one of the bonds or both might weaken when getting in contact with PBS.

Another result was that the AgNP pattern printed on a MPTMS treated PDMS surface showed large cracks in the structure as can be seen in Figure 4.6 when it was sintered with the same parameters as a AgNP pattern printed on an O_2-plasma treated PDMS surface. Due to those cracks the pattern was not conducting any more. Since such cracking was not observed for the O_2-plasma treated PDMS sample, the reason for this was most likely the higher amount of AgNP per unit area comparing the splat diameters and the overlap used for printing the patterns ($100\,\mu\mathrm{m}$ splat diameter and $40\,\%$ overlap for the O_2-plasma treated PDMS surface and $45\,\mu\mathrm{m}$ splat diameter and $50\,\%$ overlap for the MPTMS treated PDMS surface). It seems as if

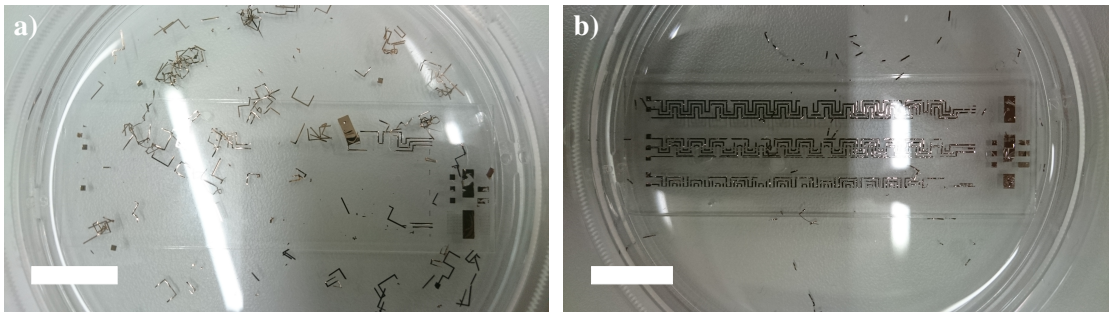

Figure 4.5: Adhesion test of inkjet printed AgNP patterns on PDMS surface in PBS. **a)** O_2-plasma treated PDMS surface. Splat diameter: $100\,\mu m$, splat overlap: $40\,\%$. Image was taken directly after immersion the sample in PBS. **b)** MPTMS treated PDMS surface. Splat diameter: $45\,\mu m$, splat overlap: $50\,\%$. Image was taken one day after immersion the sample in PBS. Both scale bars are $15\,mm$.

the AgNP pattern can conform to the thermal expansion to PDMS at $150\,°C$ when the material load per unit area is less than a certain amount. Nonetheless, a crack-free sintering of the AgNP pattern printed on the MPTMS treated PDMS surface could still be achieved by sintering the sample at $120\,°C$ for $1\,h$.

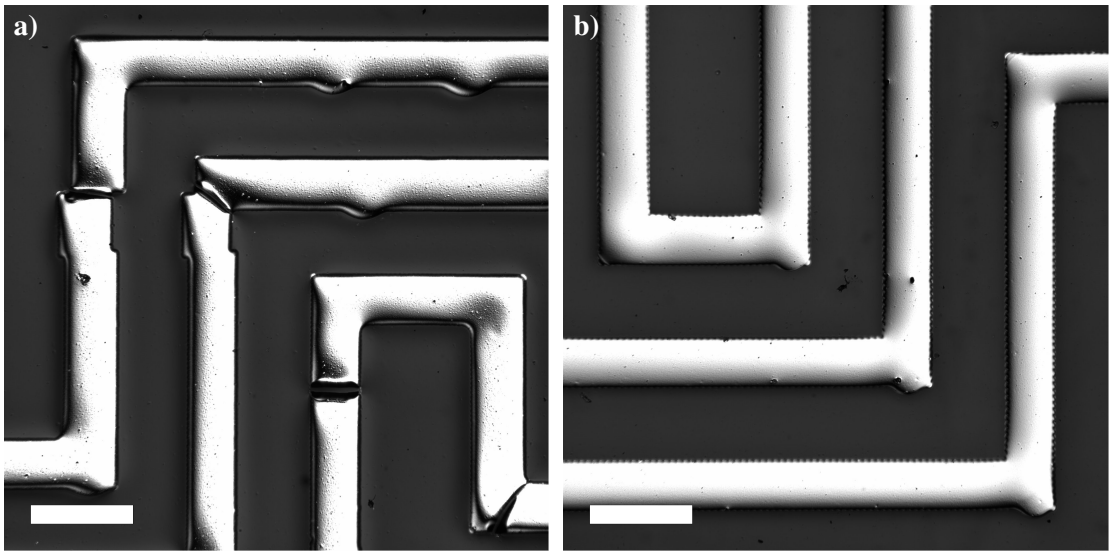

Figure 4.6: Cracking of AgNP pattern on MPTMS treated PDMS surface. Splat diameter: $45\,\mu m$, splat overlap: $50\,\%$. **a)** Sample was sintered at $150\,°C$ for $30\,min$ **b)** Sample was sintered at $120\,°C$ for $1\,h$. Both scale bars are $500\,\mu m$.

In order to overcome the challenge of a silver film delaminating from a PDMS surface in salt solution, a possible strategy would be to coat the electrode area of the AgNP pattern with another conductive material which prevents the direct contact of the silver to the salt solution and provides a stable seal at the circumference of the electrode opening. In literature a PDMS-

Pt composite was used to coat Au films lithographically patterned on PDMS so that the Au was only the conductor and the Pt in the composite acted as the electrode material [56]. In this work a similar approach was tested to coat the AgNP electrode with a conductive PDMS composite. However, instead of platinum, carbon nanotubes were blended into the silicone according to another published work [126].

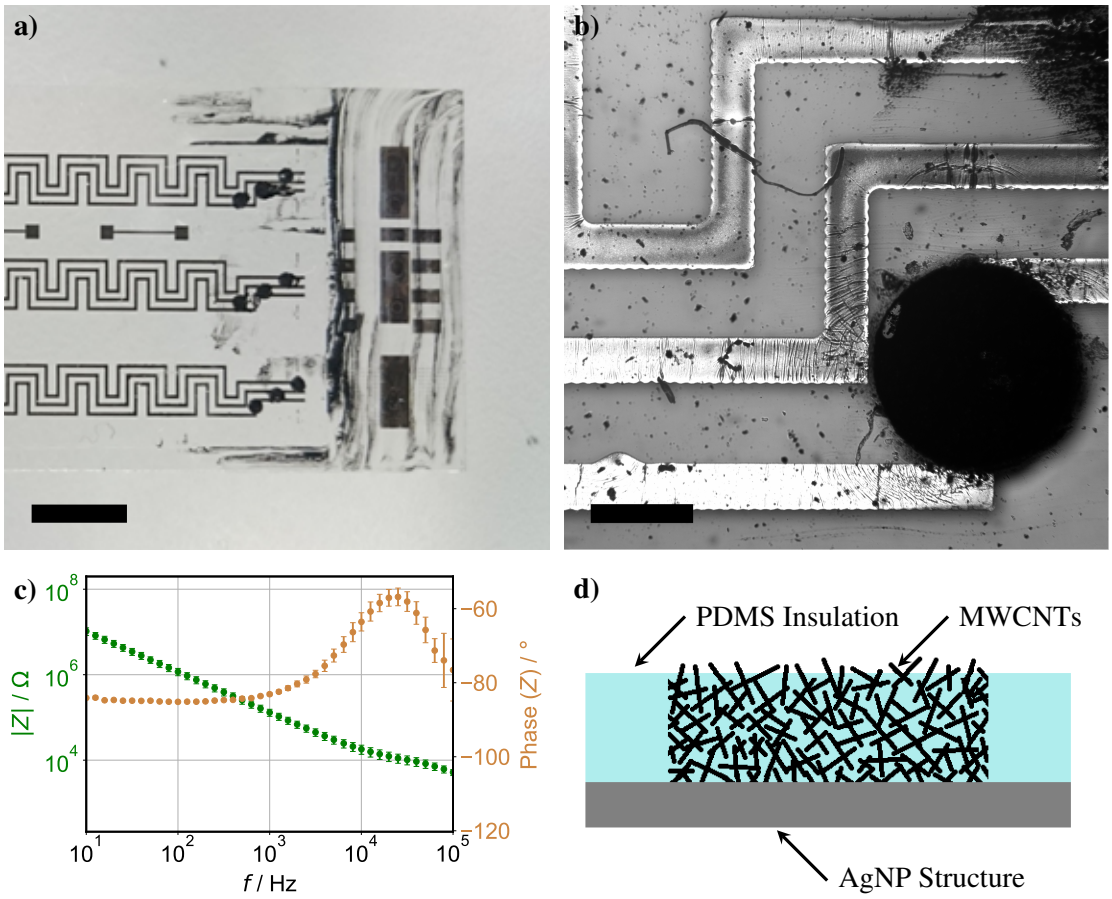

Figure 4.7: a) PDMS-MWCNT composite screen printed on top of the AgNP electrodes. Scale bar is 7 mm. **b)** Zoomed view of the lower most electrode in the left image. Scale bar is 500 µm. **c)** Impedance spectroscopy measurement of three electrodes as seen in the right image. The electrode diameter is 1 mm and the impedance at 1 kHz is $(130.6 \pm 24.5)\,\mathrm{k\Omega}$ ($n = 3$). **d)** Schematic representation of the MWCNT-PDMS composite on top of the AgNP pattern.

In Figure 4.7 a sample can be seen where multiwalled carbon nanotubes (MWCNT) blended into PDMS was brought in the circular electrode openings of the PDMS insulation layer. In one of the last manufacturing steps, the PDMS-MWCNT dough is screen printed on two such PDMS layers, were the upper one is used as a mask. When it is lifted off, it should remove the excess dough around the electrode opening. However, since an opening of 1 mm was too

large, more than the expected amount was left on the surface. During the removal of the excess conductive dough, the smearing seen in Figure 4.7 was created. This process could be improved with smaller electrode openings and by designing other optimization methods. However, the impedance of the test electrodes with a diameter of $1\,\mathrm{mm}$ was $(130.6 \pm 24.5)\,\mathrm{k\Omega}$ ($n = 3$) which was relatively high compared to electrodes made out of other materials (areal impedance of $102.6\,\mathrm{k\Omega\,mm^2}$ for the MWCNT-PDMS composite versus $49.6\,\mathrm{k\Omega\,mm^2}$ [130] and $4.6\,\mathrm{k\Omega\,mm^2}$ [131] for Au on PDMS and $0.4\,\mathrm{k\Omega\,mm^2}$ for the Pt-PDMS composite [56] from which the manufacturing approach was inspired). The reason for this high impedance might be explained by the schematic representation in Figure 4.7 d, in which one can see that only very few MWCNTs are sticking out of the PDMS carrier. Therefore the actual conductive electrode area might be in reality much smaller than the geometric electrode area resulting in an unexpectedly high impedance. At this point any further investigation of the actual cause of the high impedance or any other improvement strategy was abandoned and an entirely new manufacturing method was investigated which is explained in the following section.

4.1.2 SILVER NANOPARTICLE PATTERNS PRINTED ON PEN SUBSTRATES

In the fabrication approach described in the previous section the challenges of realizing a soft electrode interface were defined as follows: mechanical instability of a thin metal film on a soft silicone surface and a weak adhesion of the metal film on the silicone surface when immersed in PBS. While the former challenge could be solved, tackling the latter one remained an issue. In order to provide an electrode which adheres well on its substrate, an entirely new approach will be introduced in this section.

From former experiments it was known that a structure printed with AgNP was stable on a polyethylene naphthalate (PEN) substrate. Therefore, the electrode pattern was printed on this substrate material which was then subsequently encapsulated with a silicone body to provide the following three functionalities. First, by covering almost most of the substrate with silicone, a soft interface to the surrounding tissue will be provided. Second, by leaving certain areas free, the contact pad and the electrode areas will be realized. Third, by an interlocking three-dimensional closing-mechanism as seen in Figure 4.8 a, a nerve can be confined into a channel formed by a trapezoidal structure which is pushed into a groove in which the electrodes are located at the bottom.

The PDMS body around the PEN substrate was formed by placing the PEN foil with the electrode pattern into a 3D printed mold and filling the mold with the uncured PDMS polymer and curing it (Figure 4.8 b). The mold comprised the negative of the desired PDMS body. The electrode openings are formed by a tapezoidal protruding structure inside one of the mold

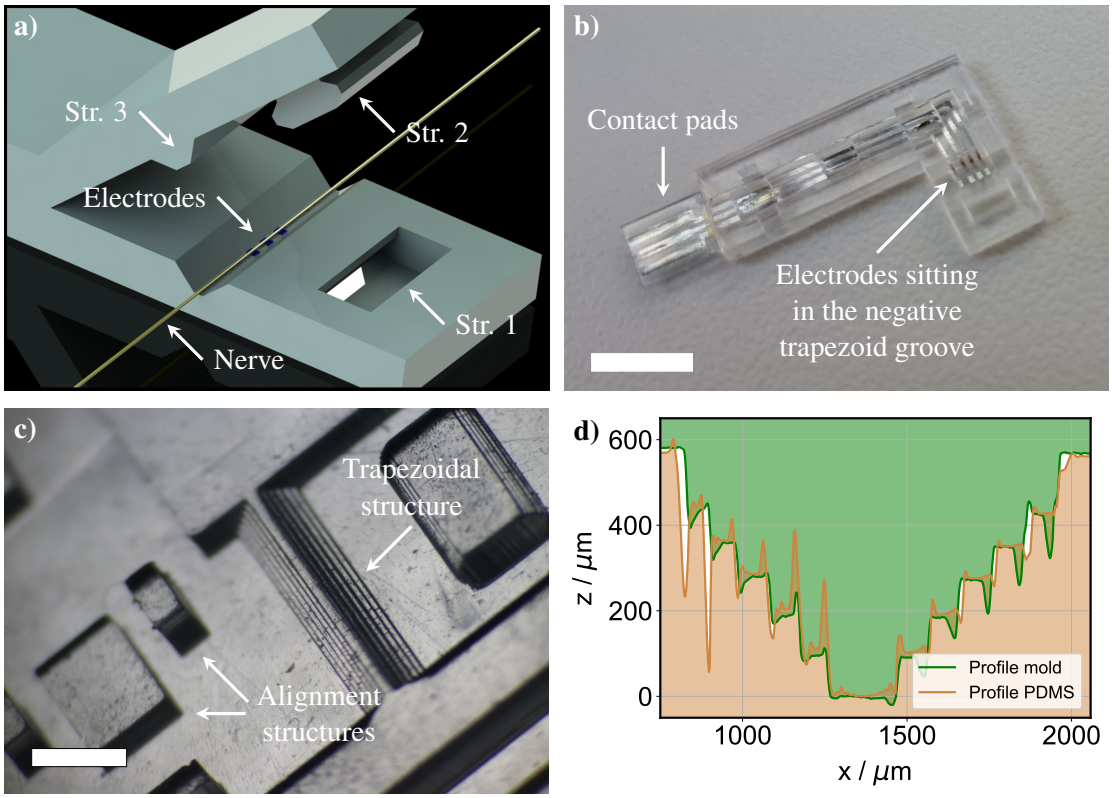

Figure 4.8: **a)** Schematic illustration of the nerve interface and a nerve with a diameter of $100\,\mu m$. The entire structure in the illustration represents PDMS. When the mechanism is closed, the outbulging structure (Str. 2) is pushed into the groove (Str. 1), which is the negative of Str. 1. Due to their form, the the mechanism stays closed. The trapezoidal structure (Str. 3) forces the nerve to be entrapped into the channel which is formed by Str. 3 and the groove with the negative trapezoid form. **b)** Lower part of the nerve interface seen in the left image. The PEN substrate comprising the electrode pattern is encapsulated with PDMS. Scale bar is $5\,mm$. **c)** Image of one of the mold halves for molding the PDMS body around the PEN foil. The protruding alignment structures are used to hold the PEN foil equally spaced to the inner walls of the mold when it is closed and filled with PDMS. Scale bar is $1.5\,mm$. **d)** Cross-sectional profiles of a structure in the mold used to form the electrode openings and the respective molded structure in the PMDS body. The green shaded positive trapezoidal area is the cross-section of the mold and the peru shaded negative trapezoidal area is the cross-section of the PDMS body formed by the mold. The peaks and valleys are due to measurement artifacts of the optical profilometer.

halves (Figure 4.8 c). When the PEN foil was placed into the mold, the flat area at the tip of this trapezoidal structure pressed on the printed side of the PEN foil while another protruding structure with a larger flat surface pressed on the foil from the other side. The height of both structures in both mold halves were the same as the surrounding areas which were brought in contact when the mold was closed. This way, the tip of the trapezoidal structure pressed tightly on the AgNP pattern and prevented this small area to be covered with PDMS during its injection

into the mold. In Figure 4.8 a, a schematic illustration of the electrode openings formed by the negative trapezoidal PDMS structure can be seen and in Figure 4.8 d profilometric cross-sectional profiles of the trapezoidal structure in the mold and the respective molded PDMS body are depicted.

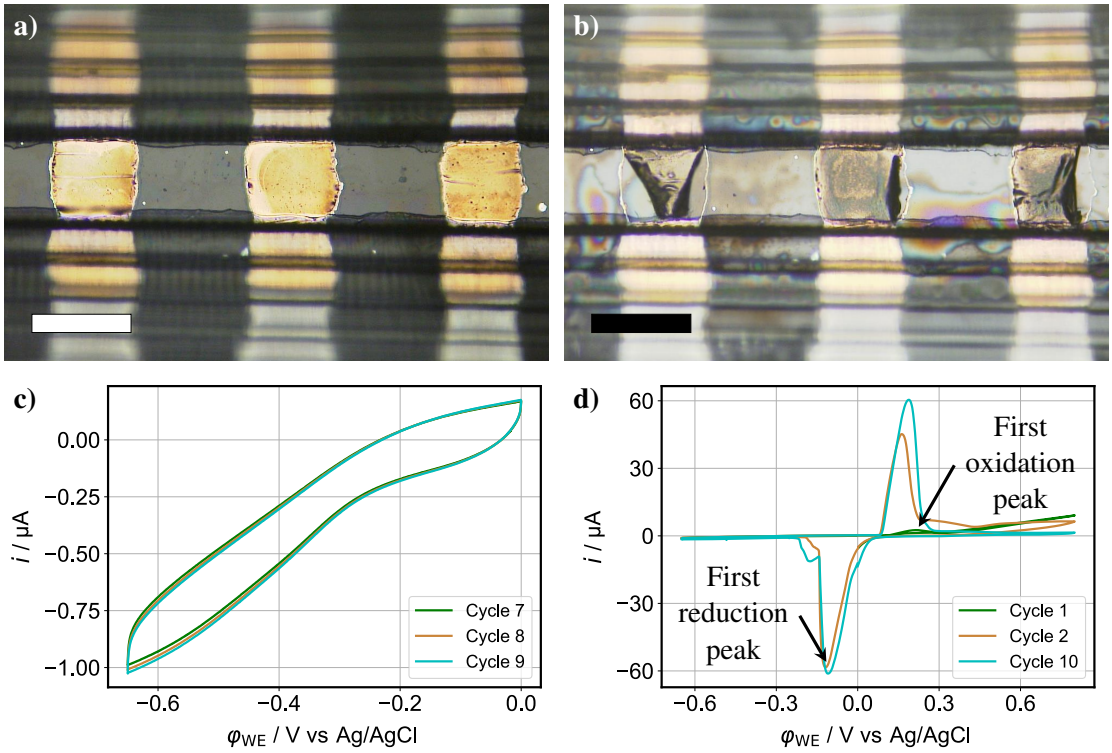

Figure 4.9: a) Au galvanized AgNP electrodes with PDMS insulation. Scale bar is $250\,\mu m$. **b)** The same electrodes after a cyclic voltammetry measurement in PBS. The electrodes oxidized and delaminated from the PEN substrate. Scale bar is $250\,\mu m$. **c)** A cyclic voltammetry measurement on one of the electrodes in the cathodic direction only. **d)** A cyclic voltammetry measurement on the same electrode as in c, in both the anodic and the cathodic direction. In both measurements the scan rate was $100\,mV\,s^{-1}$.

Since silver is known to be cytotoxic [132], Au as an electrochemically inert and a biocompatible material for implantable electrodes [133] was electrodeposited on top of the AgNP electrodes as described in subsection 3.1.7. Interestingly, the Au did not only coat the surface of the electrode, but also some area which was covered with PDMS (Figure 4.9 a). This suggests that the Au might have diffused into the porous AgNP pattern. Looking at the electrodes from their backside through the transparent PEN foil, showed that the Au diffused through the AgNP layer up to the surface of the PEN foil and also beyond the edge where the PDMS insulation starts (Appendix Figure 2 c). This result supports the idea of Au diffusion through the porous AgNP structure. However, when a cyclic voltametry measurement was carried out on the Au

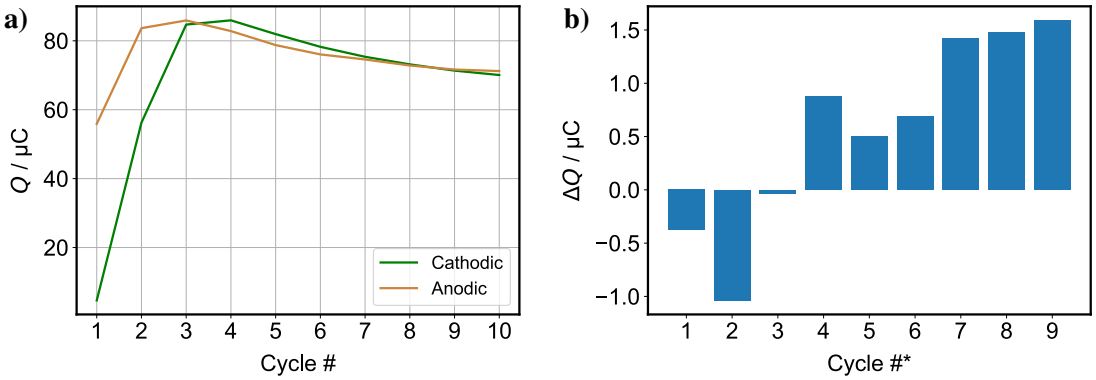

Figure 4.10: **a)** Charge of the anodic and cathodic silver reaction peaks over ten cyclic voltammetry cycles. **b)** Charge in the anodic peak in cycle n minus the charge in the cathodic peak in cycle $n+1$.

coated AgNP electrode between $-0.65\,\mathrm{V}$ and $0.8\,\mathrm{V}$, oxidation and reduction peaks were observed at $(186 \pm 2)\,\mathrm{mV}$ and $(-114 \pm 5)\,\mathrm{mV}$, respectively (averaged over the last three out of ten cycles) as seen in Figure 4.9 d. The reason of these peaks might be the reaction of silver with the chloride ions inside the PBS [134]. Even though the potentials at which the peaks occurred are not the same as reported in literature, silver particles with different dimensions were reported to have different electrochemical potentials [135]. When the cyclic voltammetry was carried out in the cathodic range only ($-0.65\,\mathrm{V}$ and $0\,\mathrm{V}$ vs Ag/AgCl), no reduction peaks occurred (Figure 4.9 c). Both cyclic voltammetry measurements started with a cathodic sweeping direction. The first reduction peak was observed during the second cycle after the first oxidation peak occurred during the first cycle. Therefore, it can be expected that first the oxidation $\mathrm{Ag} + \mathrm{Cl}^- \longrightarrow \mathrm{AgCl} + \mathrm{e}^-$ must occur to create silver chloride before it can reduced back to silver with the backwards reaction $\mathrm{AgCl} + \mathrm{e}^- \longrightarrow \mathrm{Ag} + \mathrm{Cl}^-$. When looking at Figure 4.10, it can be seen that the charge in the anodic peak of cycle n is almost the same as the charge in the cathodic peak in cycle $n+1$. Unfortunately, these peaks are not desired since they indicate that despite an Au layer on top of the AgNP pattern the Ag is still in contact with the electrolyte and may harm cells on top or in the vicinity of the electrode. The presence of electrochemical activity of printed AgNP layers coated with Au was also shown by Grob [127], who explained it by the interdiffusion of the Ag and Au layers. Even though lattice diffusion of Ag and Au atoms is observed only at higher temperatures, it was shown that at ambient temperatures Ag atoms can diffuse in polycrystalline Au films along their grain boundaries to the surface [136–138]. In order to prevent the silver oxidation and reduction peaks, the electrodeposition was performed for longer durations to achieve a thicker Au coating. However, the peaks were still present and the calculated charge during the silver oxidation and reduction reactions did not significantly change for different deposition times as was also shown by Grob [127]. He showed yet, when using a

pulsed electrodeposition protocol (a pulse consisted of negative phase of $-1.15\,\mathrm{V}$ vs Ag/AgCl for $20\,\mathrm{ms}$ followed by a positive phase of $0.4\,\mathrm{V}$ vs Ag/AgCl for $70\,\mathrm{ms}$ and a third phase of $0\,\mathrm{V}$ vs Ag/AgCl for $10\,\mathrm{ms}$) instead of a constant potential, the charge during the oxidation of Ag starts to become less for effective deposition times of $200\,\mathrm{s}$ and longer. This was explained by finer grain deposits during pulsed electrodeposition compared to electrodeposition with a constant potential. The finer grain deposits could be a good diffusion barrier for the Ag atoms and hence, less Ag could diffuse to the electrode surface and become oxidized. In addition to that he found that when the pulsed electrodeposition of Au is followed by an electrodeposition of Pt from a H_2PtCl_6 bath, also by using a pulsed protocol (a pulse consisted of a negative phase of $-200\,\mathrm{mV}$ vs Ag/AgCl and second phase of $0\,\mathrm{V}$ vs φ_0, the electrode's o equilibrium or open circuit potential, for $80\,\mathrm{ms}$) the Ag oxidation and reduction peaks could be prevented entirely. The effective deposition times were $200\,\mathrm{s}$ for Au and $120\,\mathrm{s}$ for Pt. It is worth mentioning that the electrodes in his work were three dimensional pillar electrodes. Whether his approach would also work with flat surface electrodes in this work was not tested since an entirely new fabrication approach based on a different electrode material was started before the solution for the Ag oxidation and reduction peaks were discovered by him.

As seen in the Figure 4.9 b, not only the electrochemical instability, but also the mechanical stability was often an issue during the cyclic voltammetry scans. Upon performing electrochemical measurements in PBS, the electrodes detached from the PEN substrate either partially or entirely. While this was not always the case after a cyclic voltammetry scan, it happened always upon applying stimulation pulses on the electrodes. Even when the electrodes stayed on the substrate directly after the stimulation, they detached immediately once they were rinsed with water. As mentioned further above, inkjet printed AgNP patterns on PEN substrates were quite stable in dry environment, but the observed weakness in adhesion was another challenge for reliable electrodes to be used in electrophysiological applications. It was shown in literature that when sintering printed AgNP layers above the glass transition temperature of the underlying polymer layer, the adhesion strength could be improved by an interfusion layer of both materials [139]. Even though the results shown were only for adhesion strength evaluations in dry environment, a mechanical strengthening of the adhesion by interfusion of both materials could also work in a wet enviroment. Therefore, in another test samples were sintered at $185\,^{\circ}\mathrm{C}$ for $1\,\mathrm{h}$ instead of $150\,^{\circ}\mathrm{C}$ for $1\,\mathrm{h}$, keeping all other fabrication steps the same (the glass transition temperature of the used PEN substrate material is $150\,^{\circ}\mathrm{C}$). For this evaluation, the electrical insulation of the samples was not a molded PDMS body, but a piece of Kapton tape (subsection 3.1.7). To test the stability of the electrodes they were exposed to stress by current-controlled biphasic stimulation pulses of increasing amplitude. As can be seen in Figure 4.11, corrosion starts to occur at $0.2\,\mathrm{mA}$. However, while the sample sintered at $150\,^{\circ}\mathrm{C}$ detached almost entirely by a

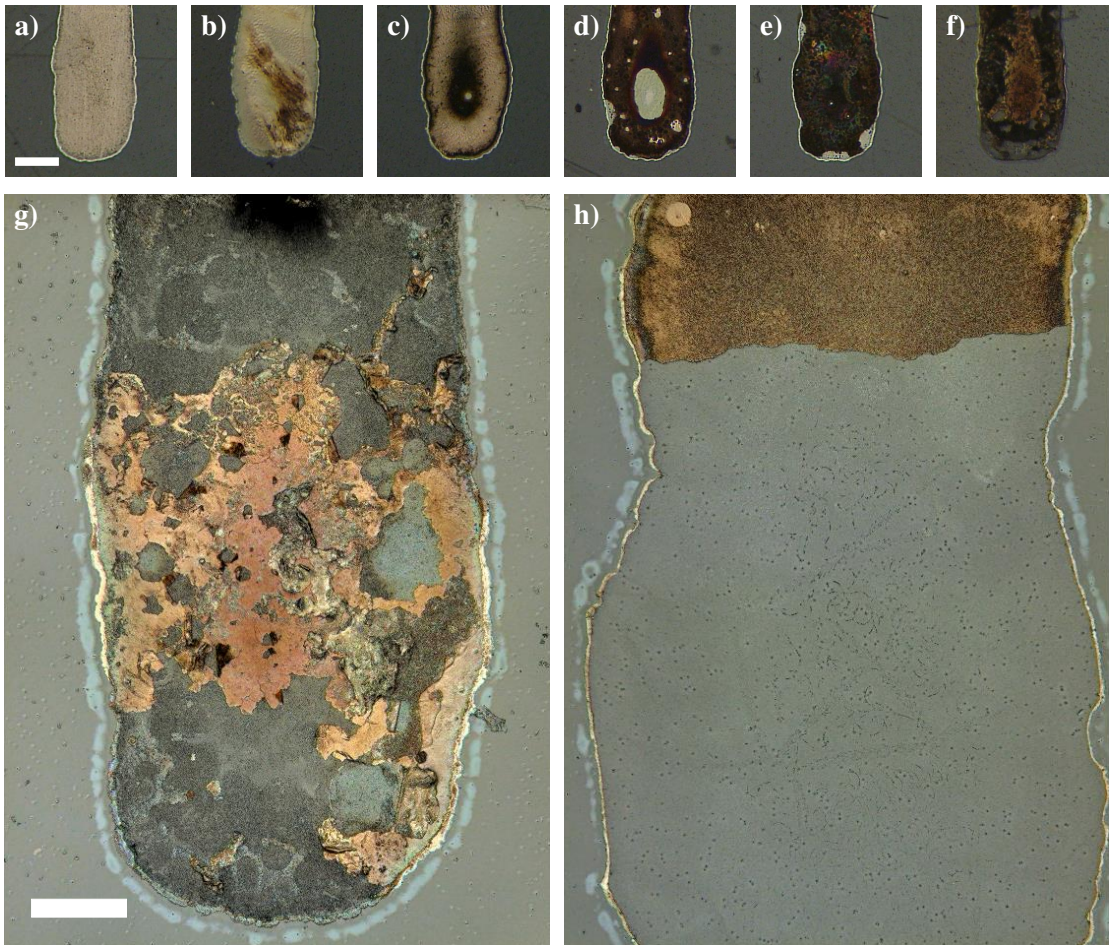

Figure 4.11: Inkjet printed AgNP electrodes on PEN substrates with an area of $(71\,800 \pm 3900)\,\mu m^2$ ($n = 12$). Samples shown in between **a)** - **g)** were sintered at $185\,°C$ for $1\,h$, while sample shown in **h)** was sintered at $150\,°C$ for $1\,h$. Electrodes were afterwards exposed to biphasic stimulation pulse amplitudes of **a)** $0.1\,mA$, **b)** $0.2\,mA$, **c)** $0.4\,mA$, **d)** $0.8\,mA$, **e)** $1.6\,mA$, **f)** $3.2\,mA$, **g)** $6.4\,mA$, **h)** $1\,mA$. Scale bar shown in **a)** is $50\,\mu m$ and applies until **f)**. Scale bar shown in **g)** is also $50\,\mu m$ and applies to **h)**.

pulse amplitude of $1\,mA$, the samples sintered at $185\,°C$ showed first signs of delamination at a pulse amplitude of $3.2\,mA$. It is worth to mention though that the stimulation charge densities used for this stability evaluation are chosen much higher ($\approx 9\,mC\,cm^{-2}$) than usually used for neuroprosthetic devices in the field ($30\,\mu C\,cm^{-2}$) [140]. Comparing Figure 4.11 g and h, the underlying PEN substrate after the AgNP pattern detached looks smooth for the sample which was sintered at $150\,°C$, while it looks much rougher for the sample which was sintered at $185\,°C$, suggesting an interfusion of the substrate and the conductor materials. Due to the observed difference in stability to stimulation pulses, sintering above the glass transition temperature of the underlying polymer layer seems to be applicable to cope with the adhesion issue between AgNP

patterns and PEN substrates in wet environments.

Even though the mechanical stability issue could be solved, the electrochemical stability of Au coated AgNP electrodes remained unsolved at the time of investigation as mentioned earlier. As a possible solution to this issue, directly printing with a biocompatible electrode material such as Au [63, 141] or with the emerging material PEDOT:PSS [121] in bioelectronic applications could be investigated. In case of a mechanical stability problem of the electrodes on the substrate, one of the adhesion improving methods described above could be tested, depending on the substrate on which the material is deposited. Another promising approach might be the printing of high-aspect-ratio materials such as CNTs [142] or Pt microparticles [143] which would also not require any post-processing and provide a mechanical stable interface when being embedded in PMDS. In this work however, an alternative fabrication route was taken while keeping the main focus on having the electrode material adhering well to the substrate in salt solution and at the same time being electrochemically inert while exposed to stimulation pulses. This new approach is presented in the following section.

4.2 SOFT NERVE INTERFACE MADE OUT OF CARBON NANOTUBES EMBEDDED IN SILICONE

In order to cope with the challenges described in the previous sections, a different electrode material, in this case carbon nanotubes (CNTs), was used. The choice fell on CNTs, due to their highly desirable electrochemical properties for neural electrophysiologic applications. At the same time, by making use of CNTs high-aspect ratio and embedding them into silicone, the electrode to substrate adhesion issue could be tackled. This was achieved through mechanical anchoring of the electrode material into the surface of PDMS. For the fabrication of the CNT/PDMS electrodes, a new fabrication method was established, which is described in subsection 3.1.8. In this section, the mechanical and electrochemical evaluation of the CNT/PDMS nerve interface and various approaches to improve its properties are presented. This is followed by an in-vivo experiment which is used as a model to demonstrate the functionality of the CNT/PDMS stimulation electrode. In the end, the design and the development of a final implantable device with a cuff closing mechanism for reliable nerve interfacing is shown.

4.2.1 MECHANICAL AND ELECTROCHEMICAL PROPERTIES OF CNT PDMS ELECTRODES

An example of a fabricated freestanding CNT/PDMS nerve interface can be seen in Figure 4.12 a. While the wider and longer part of the two CNT conductors were encapsulated in

between two PDMS layers, the thinner parts were embedded into PDMS only from one side. The other side constituted the electrode contacts. The PDMS substrate and electrical insulation thickness were $(188 \pm 10)\,\mu\mathrm{m}$ and $(41 \pm 13)\,\mu\mathrm{m}$, respectively. The stimulation electrodes had a surface area of $(0.16 \pm 0.03)\,\mathrm{mm}^2$. The CNT conductors had a cross-sectional area of $(4.9 \pm 0.7) \times 10^4\,\mu\mathrm{m}^2$ and a thickness of $(77 \pm 13)\,\mu\mathrm{m}$. In Figure 4.12 b, a cross-sectional view of the CNT conductor is shown (the electrical insulation of this sample was fabricated with the second insulation manufacturing approach, which led to a layer thickness of $(110 \pm 11)\,\mu\mathrm{m}$).

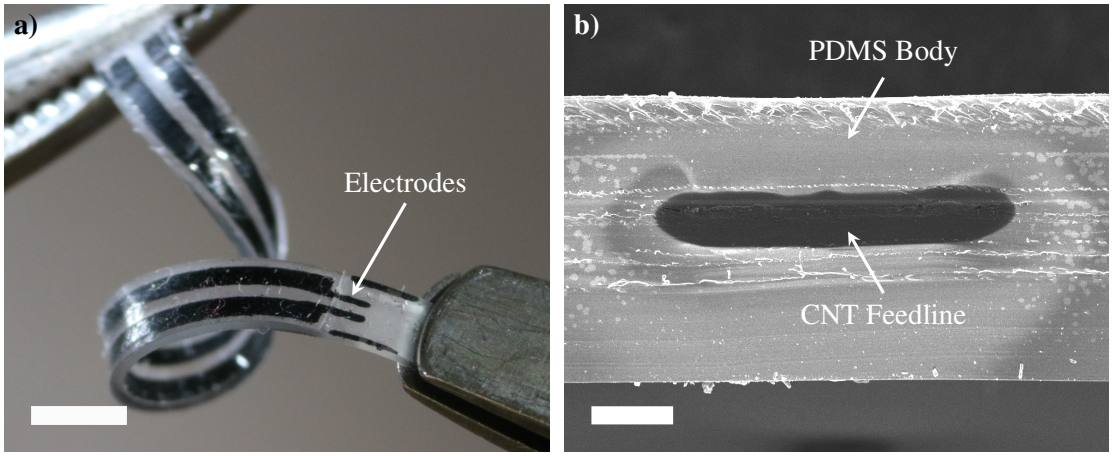

Figure 4.12: a) Image of a freestanding CNT/PDMS nerve interface. Scale bar is $3\,\mathrm{mm}$. **b)** Cross-sectional image of a CNT conductor embedded into PDMS. Scale bar is $150\,\mu\mathrm{m}$.

The conductivity of the CNT conductors was $(262 \pm 35)\,\mathrm{S\,m^{-1}}$ directly after fabrication and decreased to $(173 \pm 27)\,\mathrm{S\,m^{-1}}$ after release from the glass carrier. This difference was attributed to the uniaxial strain to which the sample was exposed during release from the glass carrier used during manufacturing. In Figure 4.13 a, the resistance change after stretching the feedline to $20\,\%$ strain up to 10000 cycles is shown. During the first ten cycles, an increase of the conductor resistance in the range of $\approx 5\,\%$ was observed, followed by a decrease ($\approx 15\,\%$ of the original value) after a few thousand cycles. Afterward, the resistance remained stable. Applying strains up to $80\,\%$ lead to an approximately twofold increase in the conductor resistance after relaxation (Figure 4.13 b), which is an acceptable value. The nerve interface is expected to be bent and stretched during normal body movements after being implanted. Therefore, the increase in resistance during the initial stretching cycle of the fabrication procedure can be neglected. These results validate the functionality of the CNTs embedded into PDMS to be used as reliable and stretchable feedlines for implantable nerve interfaces.

From cyclic voltammetry measurements in the range between $-2.5\,\mathrm{V}$ and $2.5\,\mathrm{V}$ vs Ag/AgCl (Figure 4.14 a), the water oxidation and reduction limits of the CNTs were found to be $\approx -1.5\,\mathrm{V}$

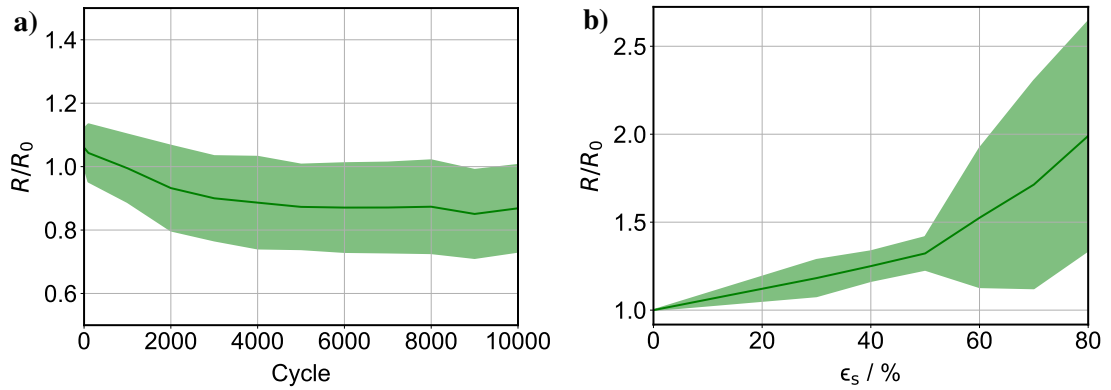

Figure 4.13: Change in resistance of CNT/PDMS conductors. **a)** Upon cyclic stretching to $20\,\%$. **b)** Upon cyclic application of increasing strains up to $80\,\%$ ($n = 6$, dark green line: mean value, light green area: standard deviation).

and $1.7\,\mathrm{V}$ vs Ag/AgCl by extrapolation of the oxidation and reduction slopes onto the voltage axis. This corresponds to a water window that is notably larger than that of the commonly used stimulatin electrodes from platinum, which spans appoximately a range from $-0.6\,\mathrm{V}$ to $0.9\,\mathrm{V}$ vs saturated calomel electrode (SCE) [107]. The reduction and oxidation limits are similar to values reported in literature for bare CNT fibers [144].

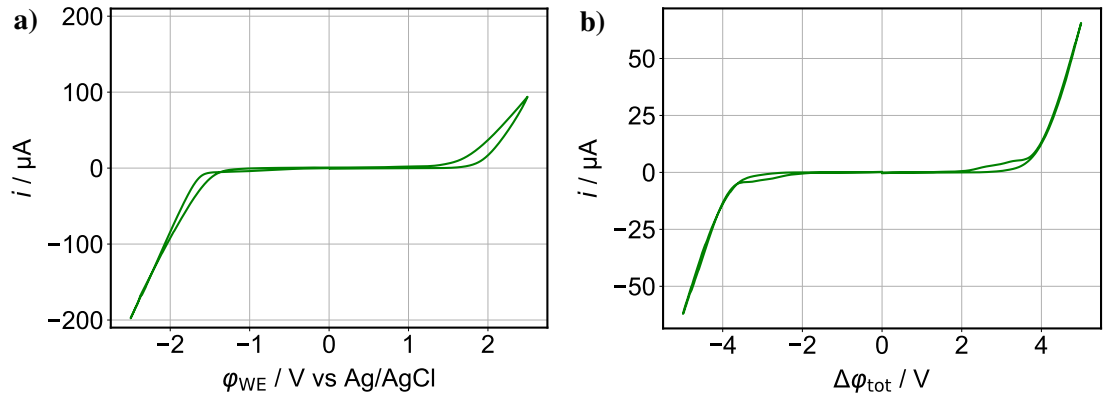

Figure 4.14: Cyclic voltammograms used to determine the reduction and oxidation limits of water for carbon nanotube electrode. **a)** Measurement on a CNT electrode in a three-electrode-configuration. **b)** Measurement between two CNT electrodes on the same electrode array.

By performing cyclic voltammetry beyond the water window, cathodic and anodic Faradaic currents are generated at the electrodes. As a result, the impedance of the electrodes decreased from $(26 \pm 4)\,\mathrm{k\Omega}$ to $(3.9 \pm 0.3)\,\mathrm{k\Omega}$ at $1\,\mathrm{kHz}$ ($n = 12$, mean $\pm$ standard deviation, Figure 4.15 a). Such a decrease was previously observed for carbon nanotube electrodes with an insulating epoxy as the substrate [145]. In this work, this decrease was sustained during repetitive mea-

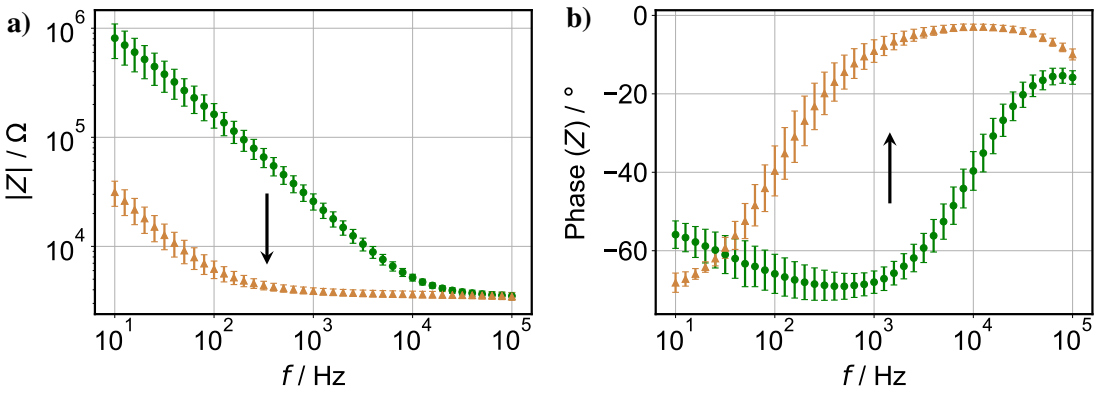

Figure 4.15: Impedance spectroscopy of CNT/PDMS electrodes with an area of $(0.16 \pm 0.03)\,\mathrm{mm}^2$ ($n = 12$, mean $\pm$ standard deviation) **a)** Change in impedance and **b)** change in phase angle before (circles) and after (triangles) surface activation via cyclic voltammetry. The arrow shows the direction of change.

surements in fresh PBS. A possible explanation for this phenomenon is that fabrication-induced contaminations adsorbed on the surface were removed during the CV scan, effectively increasing the accessible surface area. Furthermore, hydrolysis could alter the pH around the electrode, which might induce edge-plane defects or oxygen-containing functional groups on the carbon nanotube surface [146]. Such functional groups can decrease the electrode's impedance by a pseudocapacitive contribution due to redox reaction. Comparing the decreased impedance values with, for example, gold electrodes patterned on PDMS, areal impedance at $1\,\mathrm{kHz}$ was lower ($0.6\,\mathrm{k\Omega\,mm}^2$ for CNT/PDMS vs $49.6\,\mathrm{k\Omega\,mm}^2$ [130] and $4.6\,\mathrm{k\Omega\,mm}^2$ for Au on PDMS [131]). However, when the comparison was done with gold electrodes with increased surface roughness by reactive ion etching ($0.8\,\mathrm{k\Omega\,mm}^2$ at $1\,\mathrm{kHz}$ [147]), the areal impedance values were similar. Platinum-coated titanium oxide nanowire electrodes can show significantly lower impedances [67]. It is noteworthy to mention that the final impedance of the CNT electrodes was strongly affected by the CNT conductor resistance, which was $(2.7 \pm 0.4)\,\mathrm{k\Omega}$ ($n = 12$, mean $\pm$ standard deviation). In subsection 4.2.2 an attempt to decrease the feedline resistance is presented.

When the cyclic voltammetry measurement on the CNT/PDMS electrodes was performed between $-1\,\mathrm{V}$ and $1\,\mathrm{V}$ vs Ag/AgCl, a Faradaic current contribution in the cathodic region could clearly be seen. Although a capacitive only CV behavior is reported for graphene based [148] or carbon nanotube electrodes [108] in this potential region, in Figure 4.16 a, starting from $\approx -0.4\,\mathrm{V}$ vs Ag/AgCl a strong Faradaic current starts to flow towards more negative potentials. It was assumed that this is due to redox reactions of oxygen inside the PBS or oxygen-containing groups bound to the CNT surface [149]. In order to test this, the same CV experiments were performed on CNT/PDMS electrode samples after the PBS was bubbled with N_2 for one hour

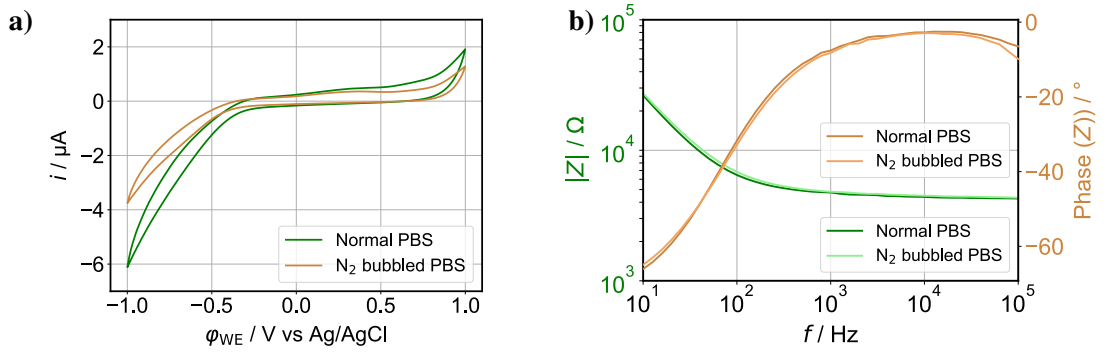

Figure 4.16: a) Cyclic voltammetry measurement of a CNT/PDMS test electrode in modified (bubbled with N_2) and unmodified PBS. **b)** Impedance spectroscopy measurement of the same test electrode again in modified and unmodified PBS.

in order to decrease the oxygen concentration inside the PBS. As can be seen in Figure 4.16 a, a decrease of $(40.0 \pm 2.9)\,\%$ ($n = 3$) in the Faradaic current contribution at $\varphi_{\mathrm{WE}} = -1\,\mathrm{V}$ vs Ag/AgCl and no significant change in the electrode impedance (Figure 4.16 b) was observed. Therefore, the Faradaic current can be associated with a redox reaction of the CNT/PDMS electrodes with dissolved oxygen inside the PBS.

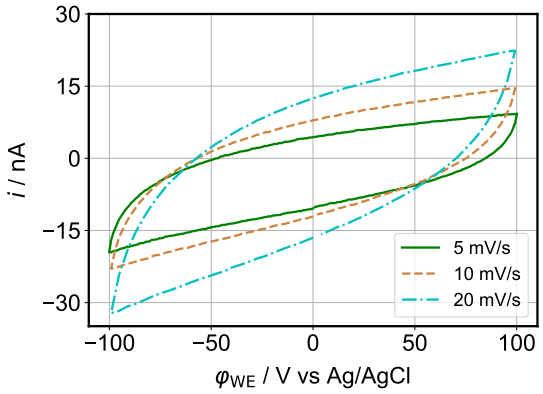

Figure 4.17: Cyclic voltammetry performed with a CNT/PDMS electrode ($0.143\,\mathrm{mm}^2$) at different scan rates.

The specific capacitance of the CNT/PDMS electrode was determined from CV measurements (Figure 4.17) to be $(0.7 \pm 0.2)\,\mathrm{mF\,cm^{-2}}$ ($n = 12$, mean $\pm$ standard deviation), which is approximately one order of magnitude less than what was reported for lithographically patterned CNT electrodes [73, 108, 150]. A possible reason for this might be that the CNTs in this work are partially embedded in PDMS, which decreases the effective surface area of the electrode. It was shown that aligned CNT films possess a larger pore size as well as a more regular pore

structure and conductive paths compared to entangled CNTs [151]. Due to the smaller and more irregular pores in entangled CNT electrodes, ions cannot diffuse easily to the inner region of the electrode, ultimately leading to a lower specific electrode capacitance. For comparison, the specific capacitance was evaluated also by fitting a simplified Randles circuit to the impedance spectra. In the low-frequency region, where the capacitive contribution dominates, a value of $(0.4 \pm 0.1)\,\mathrm{mF\,cm^{-2}}$ was obtained ($n = 12$, mean $\pm$ standard deviation). However, it should be considered that the interface is not exactly described by the Randles circuit and the results are frequency dependent.

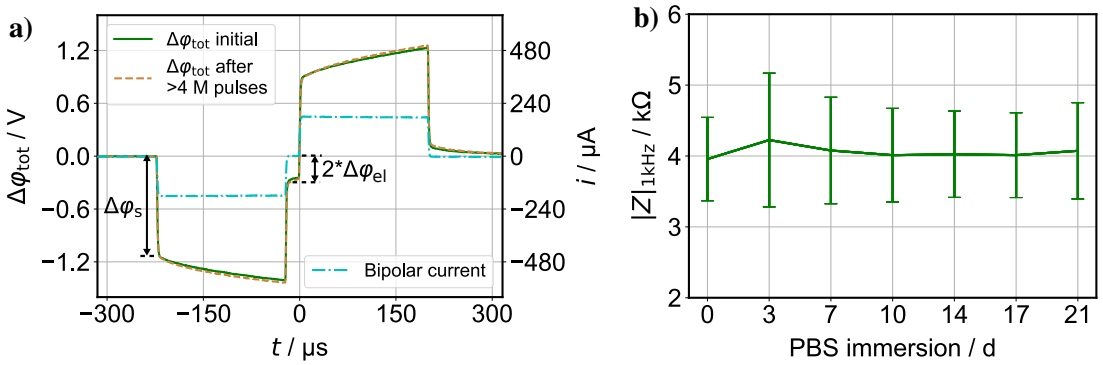

Figure 4.18: a) Voltage transient at an exemplary interface (CNT/PDMS electrode-PBS-CNT/PDMS electrode) upon application of a biphasic constant-current pulse. The current amplitude was set to have a charge density of $32\,\mu\mathrm{C\,cm^{-2}}$. **b)** Change in electrode impedance upon leaving the electrode immersed in PBS and having applied one hour of continuous stimulation per day for six days over three weeks ($n = 12$, error bars show the standard deviation).

In this work, the CIC measurement was performed between two electrodes on a single electrode array. After having determined the water window for the CNT/PDMS electrodes, a conservative value of 1 V was set as the target polarization of one electrode and a total polarization of 2 V (for two electrodes) was used to determine the CIC. Using two similar electrodes on the same stimulation device has the advantage that the measurement can also be performed during *in-vivo* experiments. It is noteworthy that determining the CIC for one electrode only in a three electrode setup in a living organism is problematic due to the possible leakage of potentially harmful materials of the reference electrode (e.g. silver from a Ag/AgCl reference electrode). An additional CV was carried out across both electrodes to show that the entire system (electrode-electrolyte-electrode) can be operated up to 2 V without significant effects of electrolysis (Figure 4.14 b). Using this approach, the CIC of the CNT/PDMS electrodes was calculated to be $(81 \pm 19)\,\mu\mathrm{C\,cm^{-2}}$ ($n = 6$ electrode pairs, mean $\pm$ standard deviation). In order to assess the long-term electrochemical stability, the CNT/PDMS electrodes were exposed to $> 4 \times 10^6$ stimulation pulses over a time period of three weeks. As during experiment for

the CIC determination, the pulses were applied between two CNT/PDMS electrodes and the polarization was evaluated. The charge density was set to $32\,\mu C\,cm^{-2}$ per phase, which is close to the allowed upper limit for deep brain stimulators ($30\,\mu C\,cm^{-2}$) and for cochlear implants to be used in patients [152, 153, 140]. Despite the applied $> 4 \times 10^6$ stimulation pulses, no severe change was found in the electrode properties, such as polarization (Figure 4.18 a) or electrode impedance (Figure 4.18 b). This shows that the CNT/PDMS electrodes are capable of withstanding prolonged stimulation conditions.

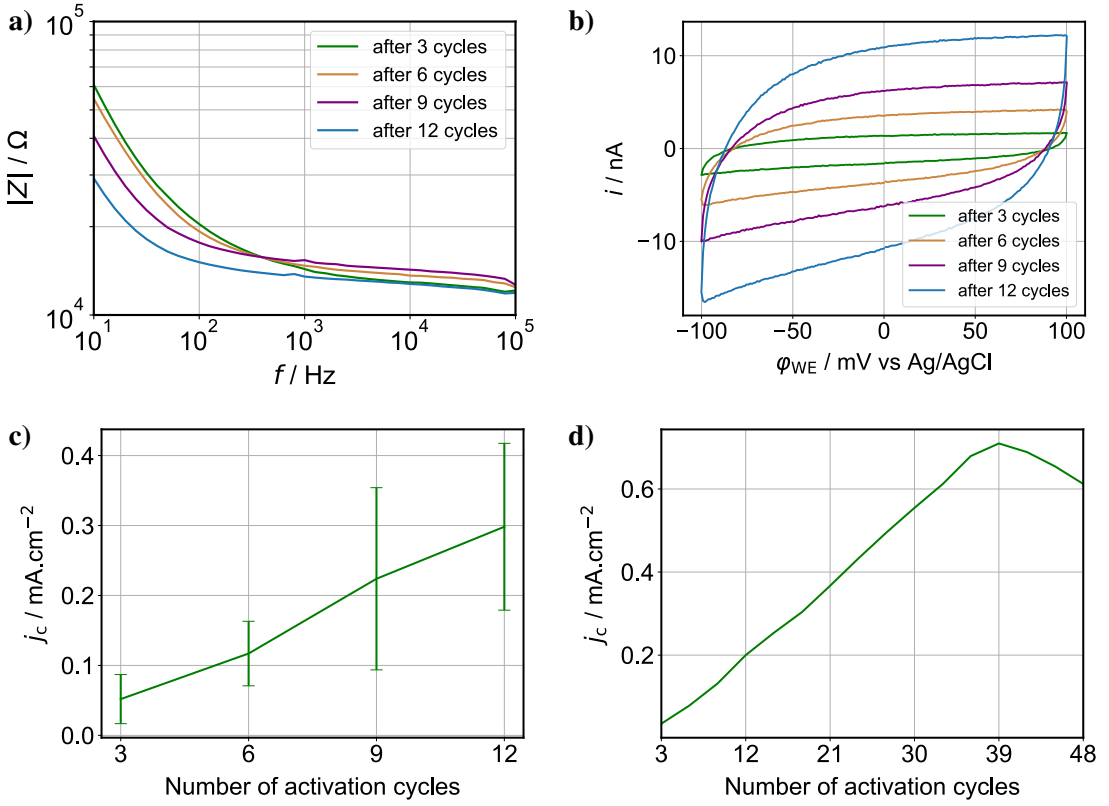

Figure 4.19: Influence of multiple surface activation cycles on electrochemical properties of CNT/PDMS electrodes. **a)** Change in impedance of an electrode with a geometric surface area of $9120\,\mu m^2$. **b)** Change in cyclic voltammetry graphs measured with a the same electrode as in **a)**. **c)** Change in capacitive current densities ($j_{anod} + |j_{cath}|$ at $\varphi_{WE} = 0\,V$ vs Ag/AgCl) evaluated from CV measurements as in **b)** ($n = 6$, mean $\pm$ standard deviation). **d)** Change in capacitive current density for a test electrode.

Since the electrode surface activation via cyclic voltammetry decreased the CNT/PDMS electrode impedance, this process was applied four more times in order to test, whether further desirable improvements in the electrodes' electrochemical properties could be achieved. The CNT/PDMS electrode samples were characterized for their impedance, capacitive charge delivery (determined from cyclic voltammetry measurements between $-0.1\,V$ and $0.1\,V$ vs Ag/AgCl)

and polarization properties, each time after they went through another surface activation as described in subsection 3.2.2. As shown in Figure 4.19 a, a further decrease in the electrodes' impedance could be seen only in the low frequency region, however, there is almost no change at higher frequencies. This can be attributed to the solution resistance and to the previously mentioned high resistance of the CNT conductors which is assumed to obscure the real value of the electrode impedance. When analyzing the capacitive currents at $\varphi_{\mathrm{WE}} = 0\,\mathrm{V}$ vs Ag/AgCl from Figure 4.19 b and c, a regular increase in the electrodes' ability to inject capacitive charge can be seen. One test electrode was used to investigate for how many surface activation cycles this improvement can be sustained (Figure 4.19 d). The results showed that there was a constant increase in the capacitive currents until 39 cyclic voltammetry applications between $-2.5\,\mathrm{V}$ and $2.5\,\mathrm{V}$ vs Ag/AgCl. Upon the exposure of the electrodes to more activation cycles, the capactive currents started to decrease.

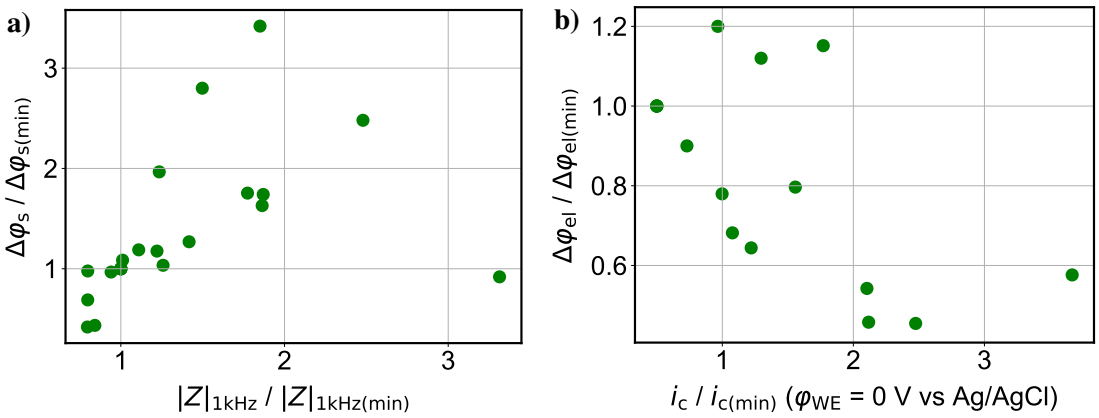

Figure 4.20: a) Correlation between access voltage (polarization across solution resistance and CNT conductor resistance) and electrode impedance. **b)** Correlation between electrode polarization and capacitive currents ($|i_c|$ at $\varphi_{\mathrm{WE}} = 0\,\mathrm{V}$ vs Ag/AgCl) obtained from CV measurements. In both graphs the given values were normalized to the smallest potential/impedance/capacitive current values for each electrode.

From the polarization graphs of the electrodes, the instantaneous polarization φs and the electrode-electrolyte interface polarization $\Delta\varphi_{\mathrm{el}}$ values were correlated to the electrodes' impedance and capacitive charge delivery properties. $\Delta\varphi_{\mathrm{s}}$ is not only a measure of the voltage drop across the solution resistance but also of the CNT conductors while its value is dominated by the latter for the electrodes in this work. Correlating $\Delta\varphi_{\mathrm{s}}$ to the electrodes' impedance values resulted in a coefficient of 0.47. This result in consideration of the polarization graph depicted in Figure 4.18 leads to following conclusion: in case of lower CNT conductor values or impedance values, smaller overall potentials could be used to drive the same amount of current through the electrodes. In terms of power management of implantable stimulation devices this is highly

desirable. The correlation between $\Delta\varphi_{\mathrm{el}}$ and the capacitive currents of the electrodes resulted in an coefficient of -0.63 and depicts that electrodes with a higher specific capacitance lead to less polarization across the electrode-electrolyte interface.

4.2.2 AU DEPOSITION ON CNT CONDUCTORS EMBEDDED IN PDMS

As already mentioned in subsection 4.2.1, the impedance of the CNT/PDMS electrodes was dominated by the relatively high resistance of the CNT conductors. An attempt to lower their resistance was by electrochemical deposition of Au on top of the CNTs (Figure 4.21). Initial tests with Au electrodeposition lead to an optically inhomogeneous Au coating of CNT conductors which was attributed to the hydrophobic surface properties of CNTs. Therefore two approaches were followed in order to turn them more hydrophilic. One was to coat the CNTs with ethylene glylcol [108] and the other by electrochemical PEDOT:PSS deposition prior to Au coating. The samples with a PEDOT:PSS surface coating had optically the most homoge-

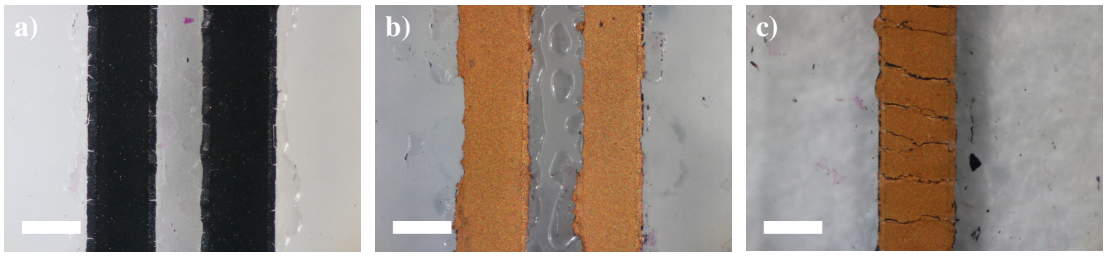

Figure 4.21: CNT conductors embedded into the surface of PDMS. **a)** Without coating. **b)** With PEDOT:PSS and Au coating. **c)** Cracked Au layer of the sample with PEDOT:PSS and Au coating after being exposed to strain during detachment from the glass carrier. Scale bars are $500\,\mu\mathrm{m}$.

neous Au coating among all samples. Depositing Au directly decreased the resistance of CNT test lines from $(2.0 \pm 0.1)\,\mathrm{k}\Omega$ to $(55 \pm 11)\,\Omega$ (reduction by $97.3\,\%$). When the conductors were immersed in ethylene glycol prior to coating, the resistance decreased from $(2.4 \pm 0.1)\,\mathrm{k}\Omega$ to $(178 \pm 130)\,\Omega$ (reduction by $92.7\,\%$), and when PEDOT:PSS was deposited on the CNTs before Au deposition, the resistance was lowered from $(2.4 \pm 0.1)\,\mathrm{k}\Omega$ to $(7 \pm 1)\,\Omega$ (reduction by $99.7\,\%$). The deposited charges did not vary much among the samples and were $1.39\,\mathrm{C\,cm^{-2}}$, $1.13\,\mathrm{C\,cm^{-2}}$ and $1.52\,\mathrm{C\,cm^{-2}}$, respectively. Although all three approaches gave promising results, after releasing the conductors from the glass carrier the resistances regained values close to their initial values they had before Au deposition, similar to the results given in the beginning of subsection 4.2.1. This was attributed to the cracks in the Au film which formed during the release as can be seen in Figure 4.21 c and lead to discontinuities in the conductive coating. According to [124] PEDOT:PSS coated Au films depict cracks when being exposed to strain, which is attributed to the PEDOT:PSS layer. Therefore, it might be assumed that the cracks in

the Au film might have formed due to cracks in the underlying PEDOT:PSS film. However, since the cracks in the Au films of the samples without any coating and with the polyethylene glycol coating exhibited the same cracking pattern, the crack formation was not accounted for cracks in the PEDOT:PSS film in this work.

4.2.3 STIMULATION EXPERIMENT WITH A HORSE LEECH

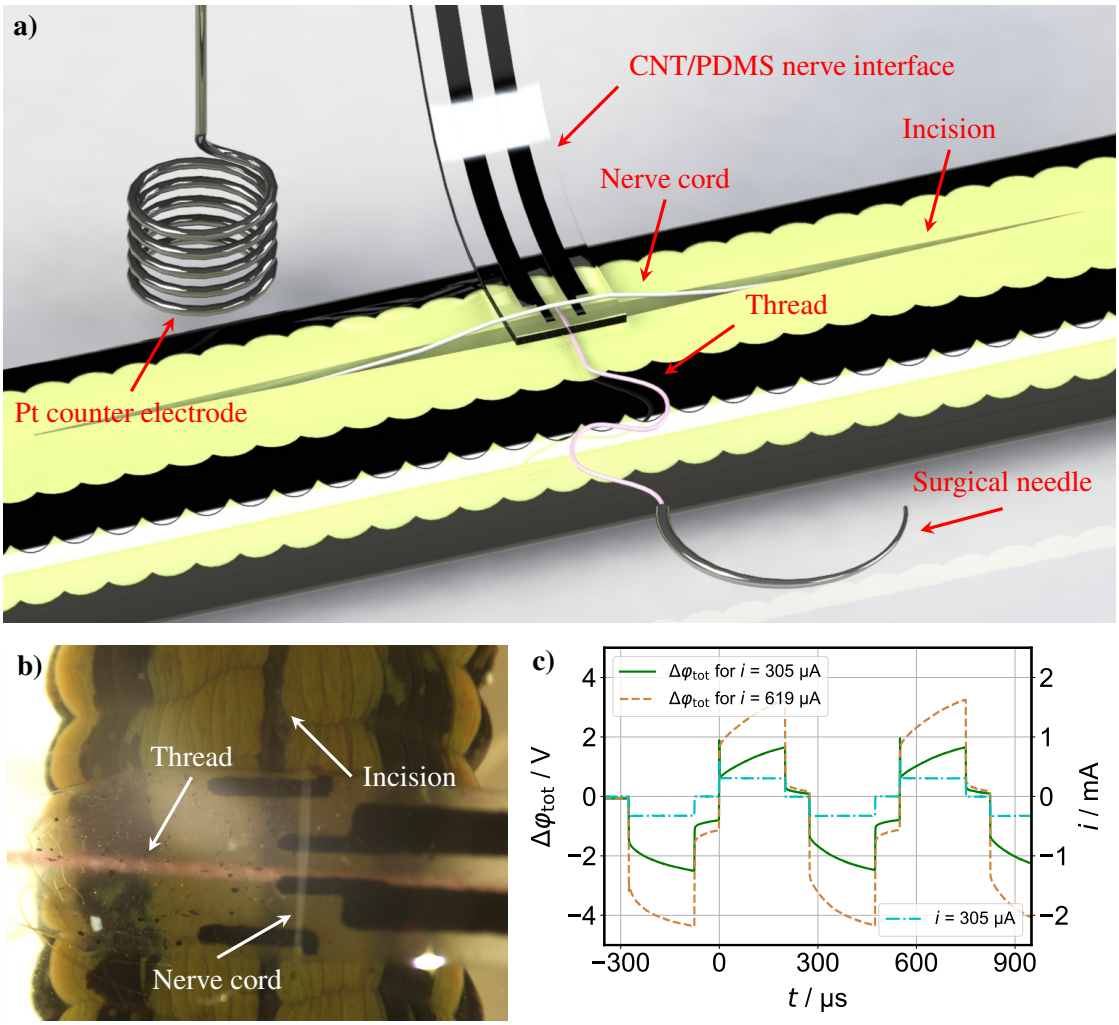

Figure 4.22: a) Schematic of the surgical and experimental setup. **b)** CNT/PDMS electrodes interfacing the main nerve cord of the horse leech. Scale bar is 1 mm. Only one CNT electrode (upper one) was used for stimulation (A =0.14 mm^2). **c)** Electrode polarization upon passing constant currents with two different amplitudes.

The functionality of the electrodes to provide successful stimulation was validated by stimulating the central nerve cord of a horse leech between two randomly selected ganglia (Figure 4.22

a and b). In order to prevent electrode potential drift and irreversible damage due to unidirectional Faradaic currents, a biphasic current pulse was chosen. A contraction along the entire leech body was evident when stimulating with a pulse train of 1000 pulses. The stimulation threshold was determined by increasing the stimulation amplitude, and the initial contractions could be observed for a stimulation current of $245\,\mu\mathrm{A}$ ($35\,\mu\mathrm{C\,cm^{-2}}$ per phase). Increasing the current to $305\,\mu\mathrm{A}$ ($43.6\,\mu\mathrm{C\,cm^{-2}}$ per phase), the contraction was clearly visible under these conditions. To assess the dependency of stimulation on the number of applied pulses, the total pulse number was decreased in steps of 100 pulses. For this experiment, a stimulation amplitude of $619\,\mu\mathrm{A}$ ($88.4\,\mu\mathrm{C\,cm^{-2}}$ per phase) was applied to ensure reliable stimulation conditions, well above the threshold. Below a pulse number of 300, the leech did not respond to the stimulation conditions. Therefore, the lower thresholds for further experiments were determined to be either a pulse train of 1000 pulses with an amplitude of $305\,\mu\mathrm{A}$ or a pulse train of 400 pulses with an amplitude of $619\,\mu\mathrm{A}$. Noteworthy is that when increasing the delivered charge during a pulse train, there was no difference in contraction intensity, which indicates that the contraction is due to elicited action potentials in the target nerve area. Next, the minimum time between two stimulation trains for a successful stimulation event was investigated. For this, 800 pulses with an amplitude of $619\,\mu\mathrm{A}$ were applied in order to avoid operation at the stimulation threshold. Thus, a contraction could be ensured given that there is enough time in between two consecutive stimulations. The duration in between two consecutive pulse trains was decreased from $11\,\mathrm{s}$ to $1\,\mathrm{s}$. For stimulation frequencies below $0.5\,\mathrm{Hz}$ ($2\,\mathrm{s}$ delay between pulse trains), the subsequent contractions following the first one visibly decreased in strength. These durations are much longer than the refractory period of an axonal action potential, which is in the order of a few milliseconds. Thus, we attribute this outcome to the sluggish relaxation of the contracting muscles, which cannot follow the stimulation repetitions. We characterized the potential excursion of the interface CNT/PDMS electrode–nerve/ringer solution–Pt wire during the stimulation of the leech. The polarization reaches up to $1.05\,\mathrm{V}$ for the amplitude of $305\,\mu\mathrm{A}$ and up to $1.5\,\mathrm{V}$ for the amplitude of $619\,\mu\mathrm{A}$ (Figure 4.22 c). In this scenario, the Pt counter electrode has a large area ($\approx 44\,\mathrm{mm^2}$), and thus, its contribution to the overall polarization should be very small or negligible. Therefore, the CNT/PDMS electrodes used in this study were able to successfully elicit action potentials while staying within their water window.

4.2.4 DESIGN AND DEVELOPMENT OF A FINAL DEVICE

Finally, a way of coupling the CNT/PDMS electrodes to a peripheral nerve and the CNT contact pads to stimulation or acquisition electronics was developed. The solutions described in the following were both either realized by molding certain silicon structures in 3D printed molds

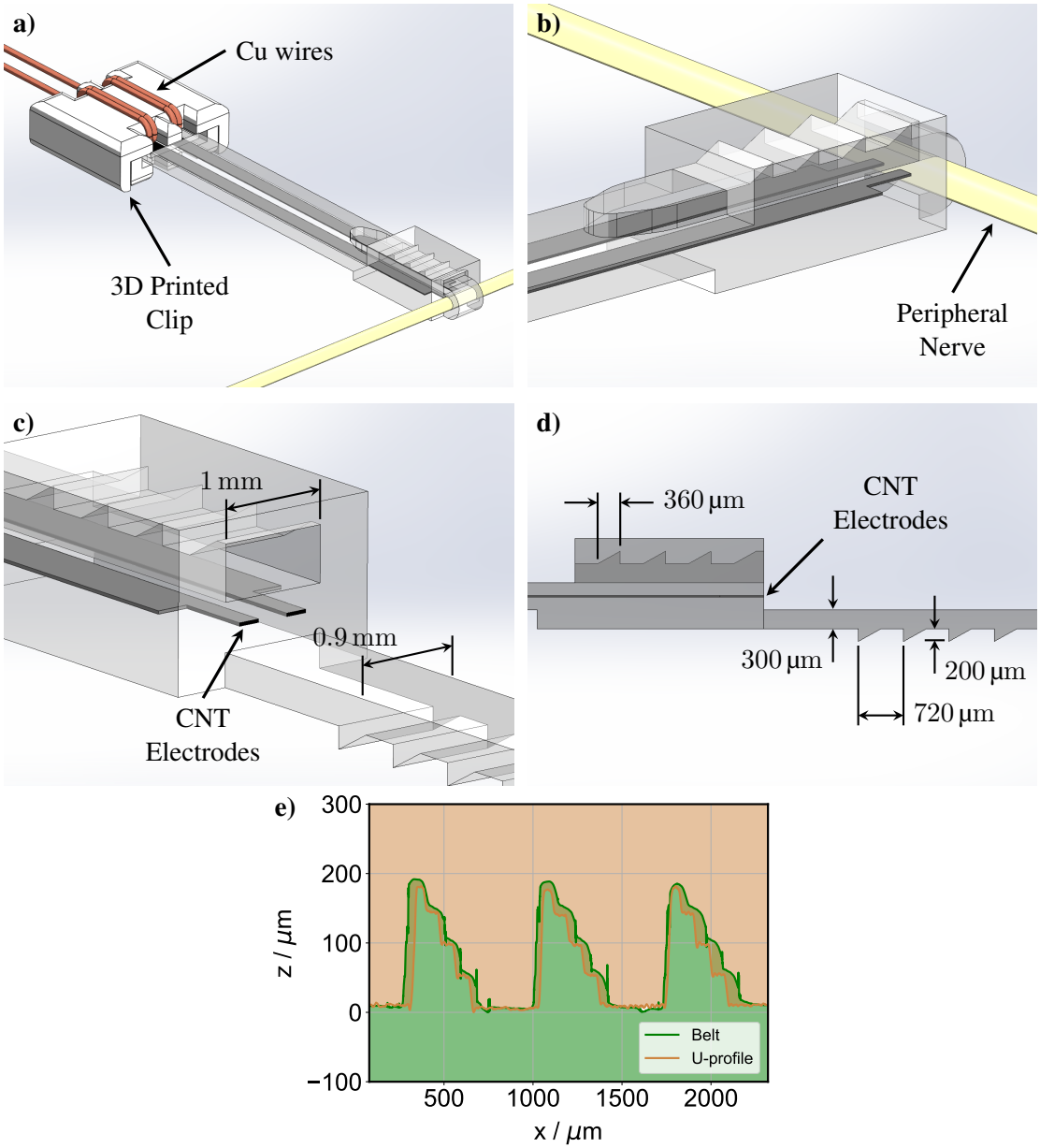

Figure 4.23: CAD illustration of the final device. **a)** A 3D-printed clip is used to connect Cu wires to the CNT contact pads. **b)** The cuff mechanism is closed to press the electrodes against a peripheral nerve. **c)** The cuff mechanism is open. The electrodes are on the same plane as the channel opening. **d)** Side view of the cuff mechanism. **e)** Cross-sectional view of a profilometric analysis of the closing mechanism from a sample. The measurements of both parts of the closing mechanism were taken independently and put together in the plot in order to visualize how the ripples of the belt part would reside into the grooves of the U-profile. The light brown area shows the cross-section of the U-profile and the light green area shows the cross-section of the belt part.

and attaching these parts to the CNT/PDMS nerve interface or by using the 3D printed structures directly.

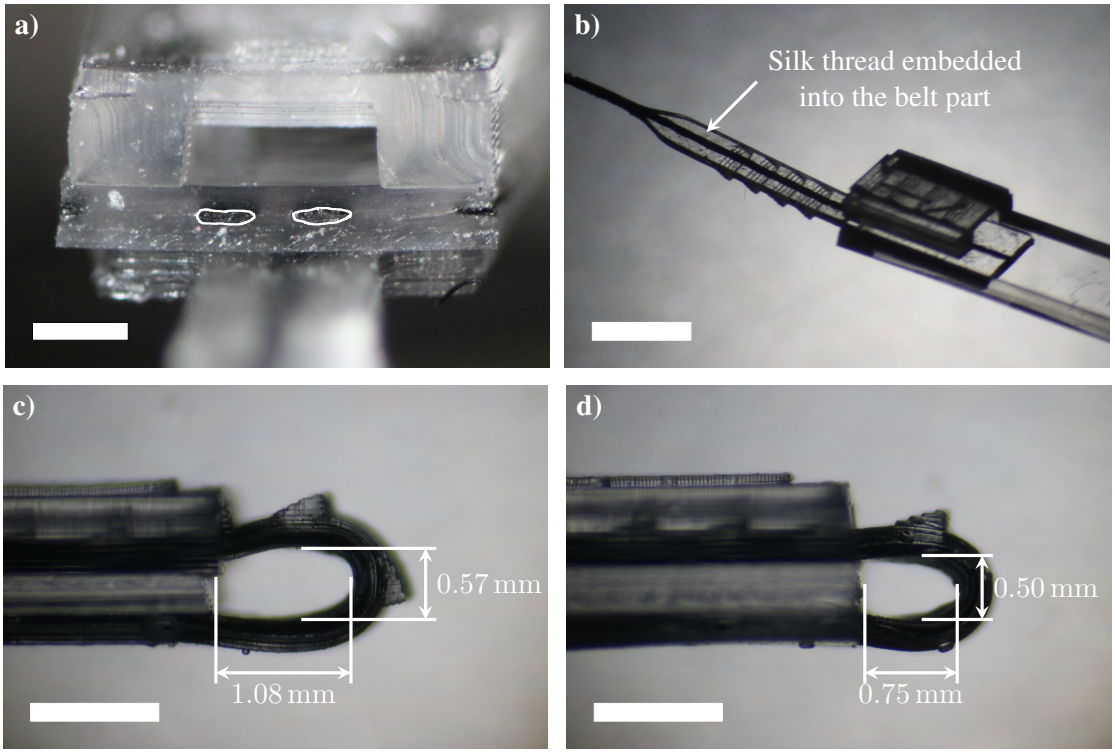

Figure 4.24: a) Front view of a final device showing the U-profile and two cross-sectional electrodes. The electrodes' circumference is highlighted with white for better visibility. The left electrode has a geometric surface area of $15\,316\,\mu m^2$ and the right electrode of $17\,297\,\mu m^2$. Scale bar is $500\,\mu m$. **b)** A dummy device without CNT electrodes showing the front end with the closing mechanism. Scale bar is $3\,mm$. **c)** Side view of a dummy device when the cuff is closed such that two out of four ripples from the belt are pushed inside the U-profile. Scale bar is $1\,mm$. **d)** The same as in the left image but when three out of four ripples reside inside their corresponding grooves of the U-profile. Scale bar is $1\,mm$.

In the final device, the cross-section of the CNT conductors which is perpendicular to the electrode array pattern was used as electrode (geometric surface area of $(15\,398 \pm 1518)\,\mu m^2$, mean $\pm$ std for $n = 6$ electrodes). The aim was to obtain electrodes as small as possible with the above described fabrication method for a higher spatial selectivity during stimulation. For a reliable interfacing of these cross-sectional electrodes with a peripheral nerve, a cuffing mechanism was designed as can be seen in Figure 4.23. In order to be able to wrap the cuff around nerves of different diameters, the design was inspired by the closing mechanism of a cable tie. Two separate parts, made by molding silicone in 3D printed molds, were bonded from both sides around the cross-sectional electrode (Figure 4.24 a). While one of the parts had a positive ripple pattern (in the following referred to as the belt), the other part had the negative

ripple pattern (in the following referred to as the U-profile). The belt could be pushed into the channel formed by the U-profile and the silicone insulation layer on top of the CNT pattern. Figure 4.23 e shows a profilometric analysis of a belt and an U-profile how the positive ripples would then reside inside the negative ripples. Since the belt is made from silicone, pushing it into a channel into which it tightly fits is a challenge. To facilitate this closing during the attachment to a peripheral nerve, a silk thread attached to a surgical needle was embedded into the belt during its fabrication (Figure 4.24 b). The needle could then be used to first draw the thread through the channel and thereafter the belt into the channel. By varying the distance of the first ripple to the electrode plane during the design or the number of ripples pushed into the channel, the cuffing diameter could be adjusted as desired (Figure 4.24 c and d).

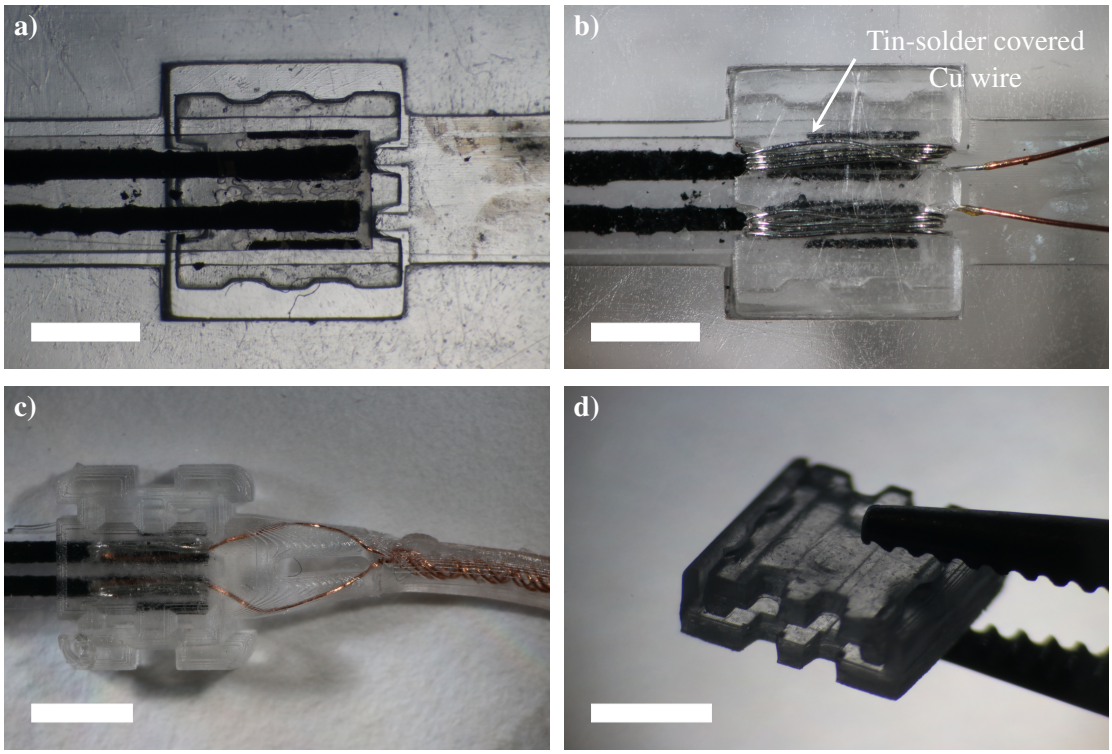

Figure 4.25: **a)** The smaller half of the Cu-CNT-clip is placed inside a 3D printed alignment aiding structure and the rear end of a CNT/PDMS electrode array is placed on top of it with the contact pads facing upwards. Scale bar is 2 mm. **b)** Tin solder coated tips of PTFE coated 100 µm thick Cu-wires are wrapped around the larger Cu-CNT-clip half which is placed onto the smaller Cu-CNT-clip half. Scale bar is 2 mm. **c)** The Cu-CNT-clip forming the electrical connection between the CNT contact pads and the Cu wires is encapsulated with silicone. Scale bar is 3 mm. **d)** A freestanding Cu-CNT-clip. Scale bar is 2 mm.

For contacting the CNT contact pads to electronics, a novel approach was required due to the soft substrate they were residing in. This was realized by a 3D-printed clip (referred to as the

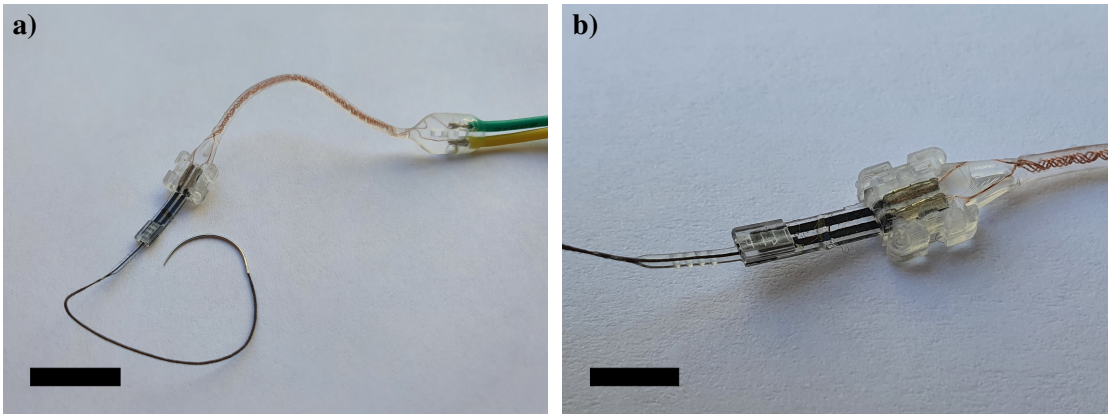

Figure 4.26: Images of the final device. The CNT contact pads are connected to Cu wires via a 3D printed clip. The Cu wires are soldered to stranded wires for simple and reliable connection to electronics. **a)** Scale bar is 15 mm. **b)** Scale bar is 6 mm.

Cu-CNT-clip) composed out of two separate parts. As can be seen in Figure 4.23 a, thin metal wires can be wrapped around one half of the clip (Figure 4.25 b) which can then be pressed on the CNT contact pads by clipping the two separate parts together. It was important that both parts of the clip are fastened tightly around the PDMS substrate and that the metal contacts are pressed firmly on the CNT contact pads in order to achieve a stable electrical connection. This was realized by leaving a distance of 30 µm from both sides between the inner side walls of the larger part and the outer side walls of the smaller part of the clip (see Appendix Figure 4, vertical measures in b and c). Figure 4.25 a and b show how the clip parts were placed around the CNT contact pads. In the end, the entire clip was cast into silicone to insulate the CNT contact pads and the Cu wires from the body fluid (Figure 4.25 c). This was also important to prevent any micromovements between the contact pads and the wires from damaging the CNT contact pads. The Cu wires were also cast into silicone after forming them into a helical structure. Thereby, the electrical connection between a stimulator or recorder and the CNT contact pads could accommodate any stress induced during body movements.

In Figure 4.26, images of a final device are presented. The other end of the spiralized Cu wires were soldered to flexible commercial wires for simple and reliable connection to electronics for experimental setups. The soldered area was also cast in silicone with the same molding technique used for the other parts. By increasing the length of the needle used during the fabrication of the spiralized part of the Cu wires (described in subsection 3.1.10) and adapting the mold, the distance between the CNT contact pads and implantable electronics could be accommodated as desired. Such a case might be necessary when the area of interfacing a peripheral does not permit the implantation of a recording and stimulating device in its vicinity.

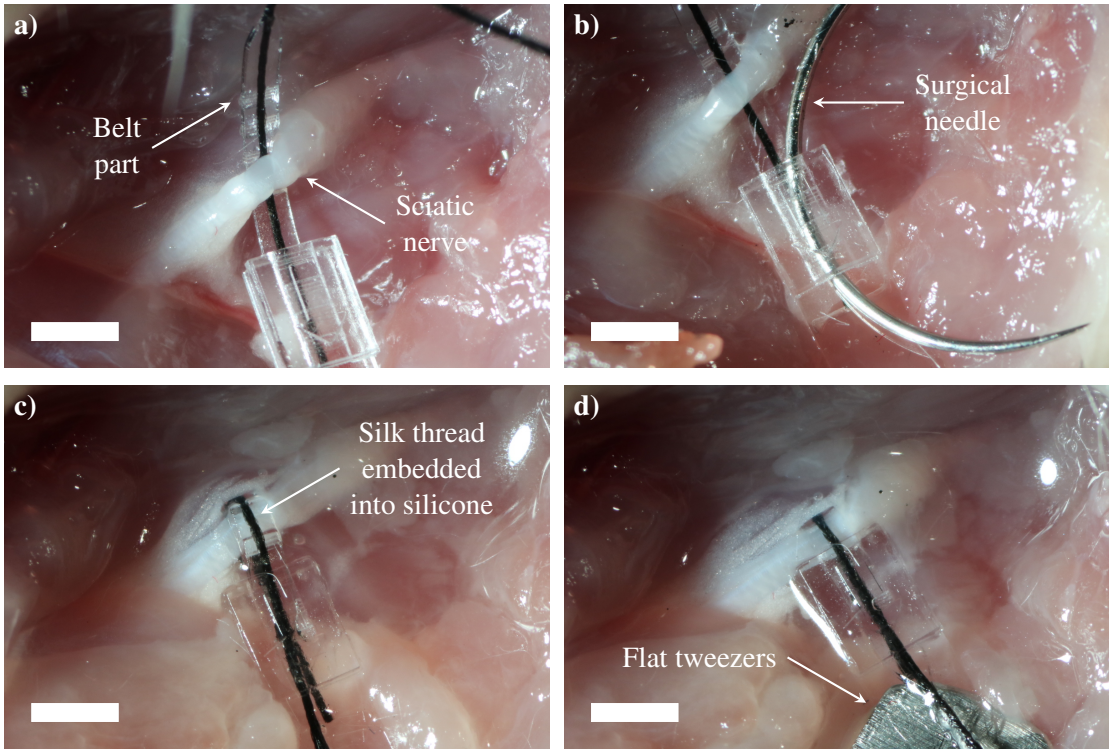

Figure 4.27: Wrapping the cuff mechanism around the sciatic nerve of a rat. **a)** The belt part is pushed beneath the nerve by the semicircle shaped surginal needle which is attached to the belt part by a silk thread. **b)** The surgical needle is pushed into the channel of the closing mechanism formed by the U-profile to pull the thread and thereby the belt part through the channel. **c)** The belt part is pulled through the channel of the closing mechanism. **d)** The belt is pulled so much that the nerve is pressed against the electrodes (which are not available in the dummy sample shown in the images) residing on the same plane as the channel opening. Scale bars are $2\,\mathrm{mm}$.

Finally, a dummy device without electrodes was used to demonstrate the cuffing mechanism by attaching the device around the sciatic nerve of a dead rat (Figure 4.27). The surgical needle was used to guide the belt beneath the nerve and to insert it into the channel of the U-profile. By holding the device with tweezers and pulling at the needle, the belt could be pushed inside the channel until the nerve was tightly wrapped by the belt and pressed against the plane on which electrodes are supposed to reside.

The demonstrated cuffing mechanism could be used to interface peripheral nerves for various research purposes and medical treatment experiments in different animal models. By stimulating the vagus nerve in rodents for example, its influence on epilepsy, depression and other neuropsychiatric disorders could be investigated [154]. Neural modulation of the posterior tibial nerve [155] or recording the activity of the afferent fibers of the pelvic nerve [147] could be performed to achieve control over the bladder for people suffering from incontinence. As

another example, vocal fold paralysis which is mainly caused by an synkinetic reinnervation of the posterior cricoarytenoid muscle in the larynx due to a damage to the recurrent laryngeal nerve could be targeted. While this neurological disorder is addressed by stimulating the neuromuscular junction of the muscle [156], direct stimulation of the recurrent laryngeal nerve could be tested. These neural modulation application are mainly open-loop applications. In order to achieve a higher degree of control of the targeted organ, a closed-loop stimulation could be performed on peripheral nerves while using large insects as an alternative animal model [157]. By combining the nerve interface with a fully implantable stimulation and recording system with wireless control, scientists could also investigate neural modulation in animals without having their bodies fixed on an experimental setup. In summary, the developed cuffing mechanism in combination with the CNT electrodes offers researchers and medical doctors a reliable interface for peripheral nerves.

CHAPTER 5

CONCLUSION AND OUTLOOK

In conclusion, an implantable soft neural interface with a cuffing mechanism for peripheral nerves was developed. The fabrication methods were mainly based on various printing technologies. The first approach to realize this device was by using inkjet printing. Ag nanoparticles were deposited as conductors. Since the underlying substrate on which the Ag conductor was patterned was a soft elastomer, breakage in the electrical conduction pathway along the conductor posed a problem upon strain application. The surface of the not encapsulated part, serving as the electrode, was modified by Au electrodeposition to provide a biocompatible interface to nerve tissue. However, the Au coating could not provide an electrochemically stable barrier between the Ag and the electrolyte solution. The weak adhesion between the Ag and the silicone substrate in electrolyte solution was improved by chemical surface treatment, yet not to an end with desirable stability. In order to address this challenge, a carbon nanotube comprising silicone composite was deposited onto the electrode. The final electrode impedance was yet not in a range with which this manufacturing approach could have led to the realization of a functional neural interface. Since inkjet printing is yet a very powerful technique to rapid prototype new electrode array designs, this approach could be in future pursued by using an intrinsically stretchable polymer [121] to address the issue of electrical conduction breakage in conductors encapsulated in between stretchable insulation layers. Another strategy for stretchable conductors might be printing metallic powder [158, 143] with larger particle size compared Ag nanoparticles and then embed it in fluid silicone before curing the silicone to realize a conductive composite. For the electrodes, further investigations should focus on a strong bonding between the silicone substrate and the electrode material, if the not encapsulated end of the conductor will be used directly as the electrode. Alternatively, an encapsulation of the electrode with a highly conductive composite [56] might be used as well.

As a solution to the challenges faced with the direct inkjet printing and subsequent electrode

coating approach, CNTs, being a high-aspect-ratio material, were embedded into the silicone matrix after patterning them on a filter membrane by selective vacuum filtration. Thereby, the electrical connection of the conductors remained stable after repeated application of strain. A faced challenge was their relatively high resistance. Even though it could be descreased by electrodeposition of Au on the CNT conductors, this effect was canceled when they were stretched. Further investigations on decreasing the conductor resistance might test the incorporation of Au nanowires or the alignment of the CNTs during the filtration process [159–161]. Aligned CNT films were shown to have increased conductivity in the alignment direction. Due to the mechanical anchoring of the CNTs inside the elastomer body, no delamination of the electrodes from the substrate occurred. Furthermore, the CNTs could be used directly as the sole electrode material without any surface modification for interfacing with nerves since they are electrochemically stable. Their biocompatibility, however, is still controversal [112–116]. Therefore, the long-term biocompatibility of CNTs serving as neural electrodes should be further investigated. It was shown that driving Faradaic currents through the CNTs while polarizing them beyond their water window led to a decrease in electrode impedance. The stimulation capabilities of the CNT electrodes was validated by the extracellular stimulation of the central nerve cord of a horse leech and correlating its muscle movements to the applied stimulation signals. Finally, 3D printing was used for the rapid prototyping of molds for silicone injection. The silicone parts produced by this method were used to fabricate a cuff closing mechanism around the electrodes which could be adjusted according to the nerve diameter. Furthermore, a 3D printed clip was developed in combination with silicone molding to realize a stable interconnect between CNT contact pads on the soft elastomer substrate and stimulation and recording electronics. Using this encapsulation approach for the contact pads, fully implantable neural modulation systems could be fabricated for research or for medical treatment applications.

In the final device with the cuff closing mechanism, the cross-section of the CNT conductors were used as electrodes. In future, this approach might be used to stack multiple layers of the demonstrated design on top of each other to fabricate an array with electrodes aligned not only in one dimension, but in a two-dimensional matrix fashion. Thereby, a higher electrode count could be incorporated in the nerve interface for, e.g., a more advanced control of neuroprosthesis.

APPENDIX

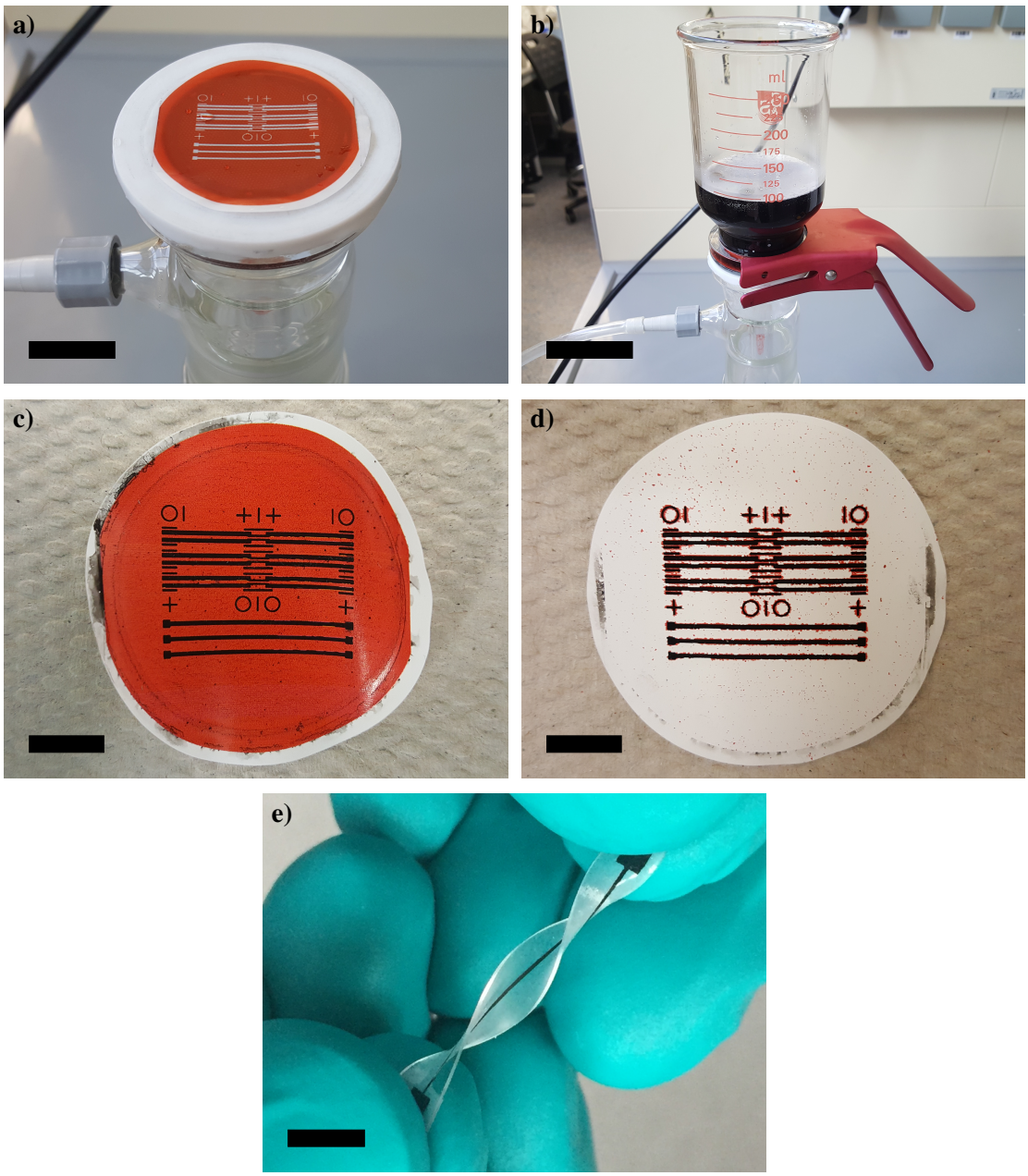

Figure 1: Fabrication steps of CNT-PDMS electrode array. **a)** Filter membrane with wax pattern on top of lower part of the filtration setup. Scale bar is 15 mm. **b)** Pattern-assisted filtration process of CNT-DI-water dispersion. Scale bar is 40 mm. **c)** CNT pattern on wax-free areas of the filter membrane. Scale bar is 10 mm. **d)** Filter membrane with wax pattern removed leaving only the CNT pattern on the membrane. Scale bar is 10 mm. **e)** CNT pattern transferred and embedded into a silicone substrate. Scale bar is 5 mm.

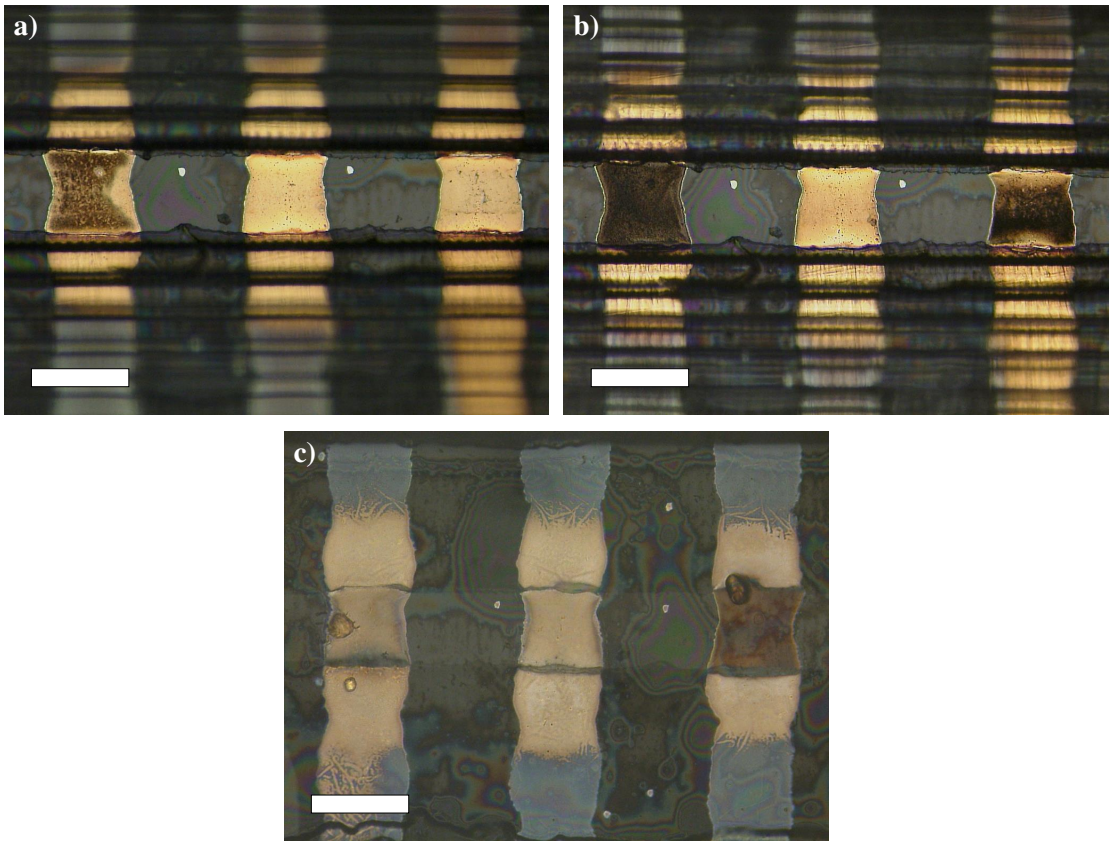

Figure 2: Images of a sample on which Au electrodeposition was performed for $5\,\mathrm{min}$. **a)** Directly after electrodeposition. The reason for the dark area of the left electrode is not known. **b)** After the left and the right electrode were exposed to ten cycles of cyclic voltammetry between $-0.6\,\mathrm{V}$ vs Ag/AgCl and $0.8\,\mathrm{V}$ vs Ag/AgCl. **c)** An image from the backside when the sample was flipped vertically by $180°$. It can be seen that the Au diffused through the porous AgNP pattern not only until the surface of the PEN foil but also farther along its length than the theoretically limiting PDMS insulation layer. However, the corrosion occured only at the electrode opening. Scale bars are $250\,\mu\mathrm{m}$.

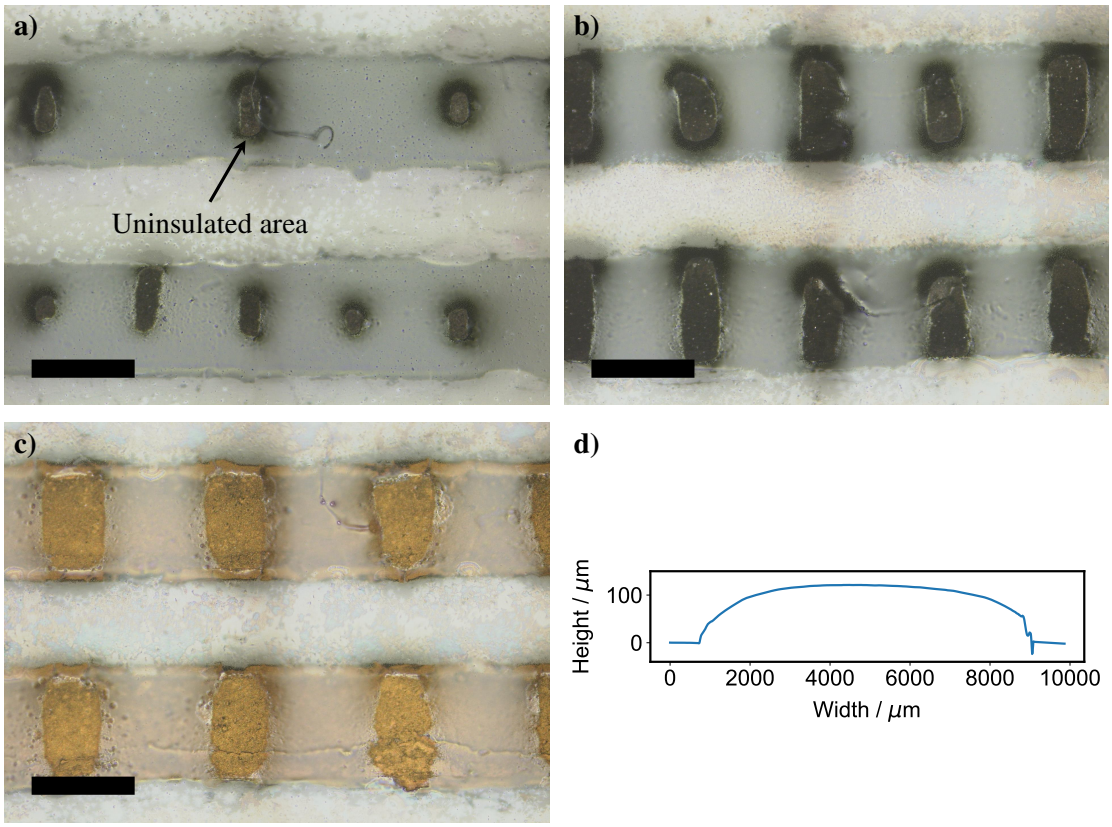

Figure 3: Images and profilometric analysis of extrusion printed PDMS insulation layers. The layers were printed with a line spacing of **a)** $500\,\mu m$, **b)** $600\,\mu m$, **c)** $800\,\mu m$, **d)** $300\,\mu m$. While in a and b the insulation layer was printed directly on a CNT pattern embedded in PDMS, in c it was printed after an Au layer was electrodeposited on top of the CNT pattern. In all three images uninsulated areas can be seen. The layers printed with a line spacing of $400\,\mu m$ or smaller did not have any uninsulated areas. Scale bars are $500\,\mu m$.

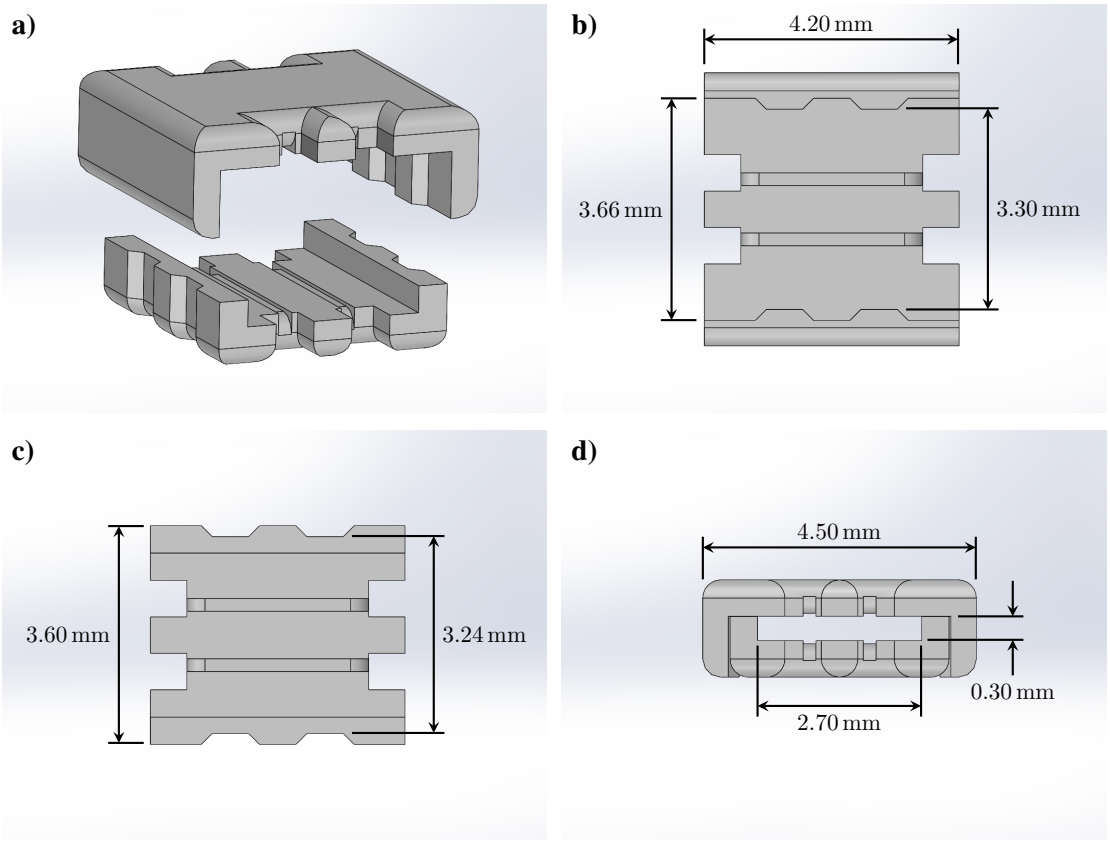

Figure 4: CAD drawing of the 3D printed clip used to press Cu wires onto the CNT contact pads. Only the dimensions important for securing the clip onto the CNT/PDMS conductors are shown. **a)** Exloded view of both clip parts. **b)** Top view of the larger clip half. **c)** Top view of the smaller clip half. **d)** Front view of the clip when both halves are fastened to each other.

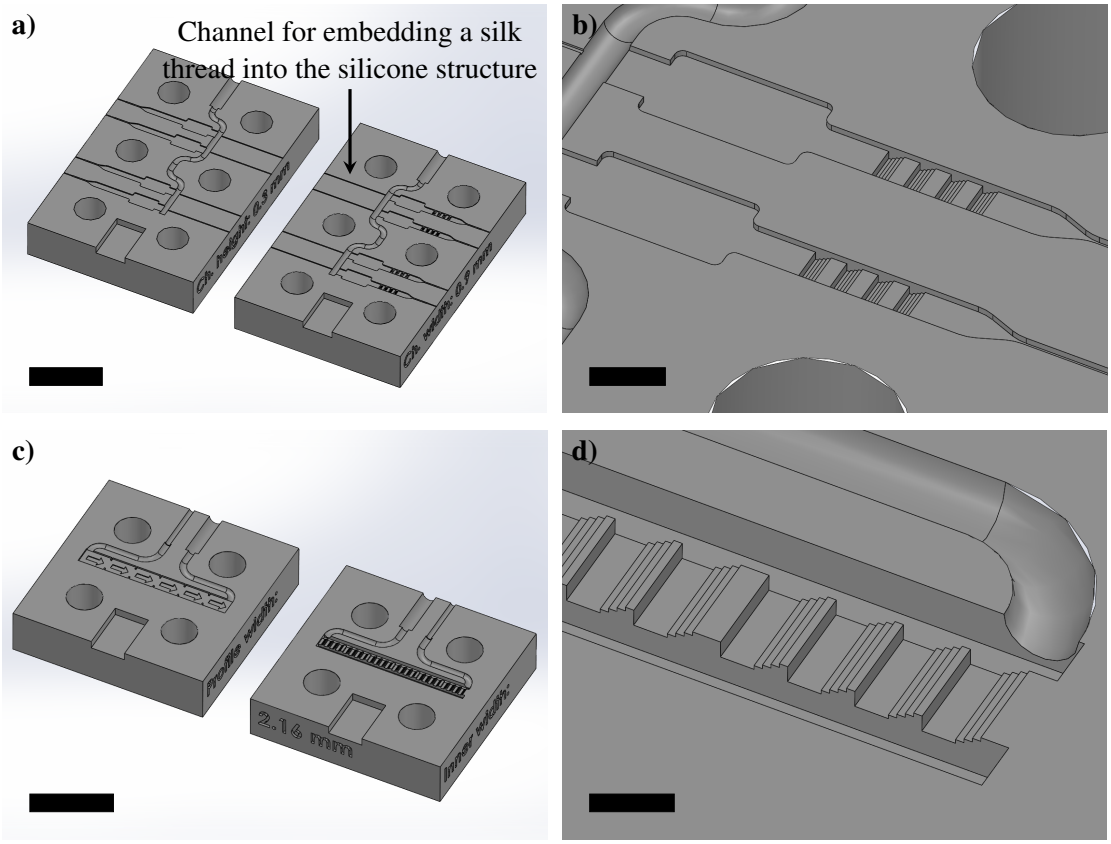

Figure 5: CAD drawing of the molds which were used to fabricate the closing mechanism out of PDMS. **a)** The mold for the belt part. Scale bar is $10\,\mathrm{mm}$. **b)** Zoomed view on right mold half in a. Scale bar is $2\,\mathrm{mm}$. **c)** The mold for the U-profile. Scale bar is $10\,\mathrm{mm}$. **d)** Zoomed view on the right mold in c. Scale bar is $1\,\mathrm{mm}$.

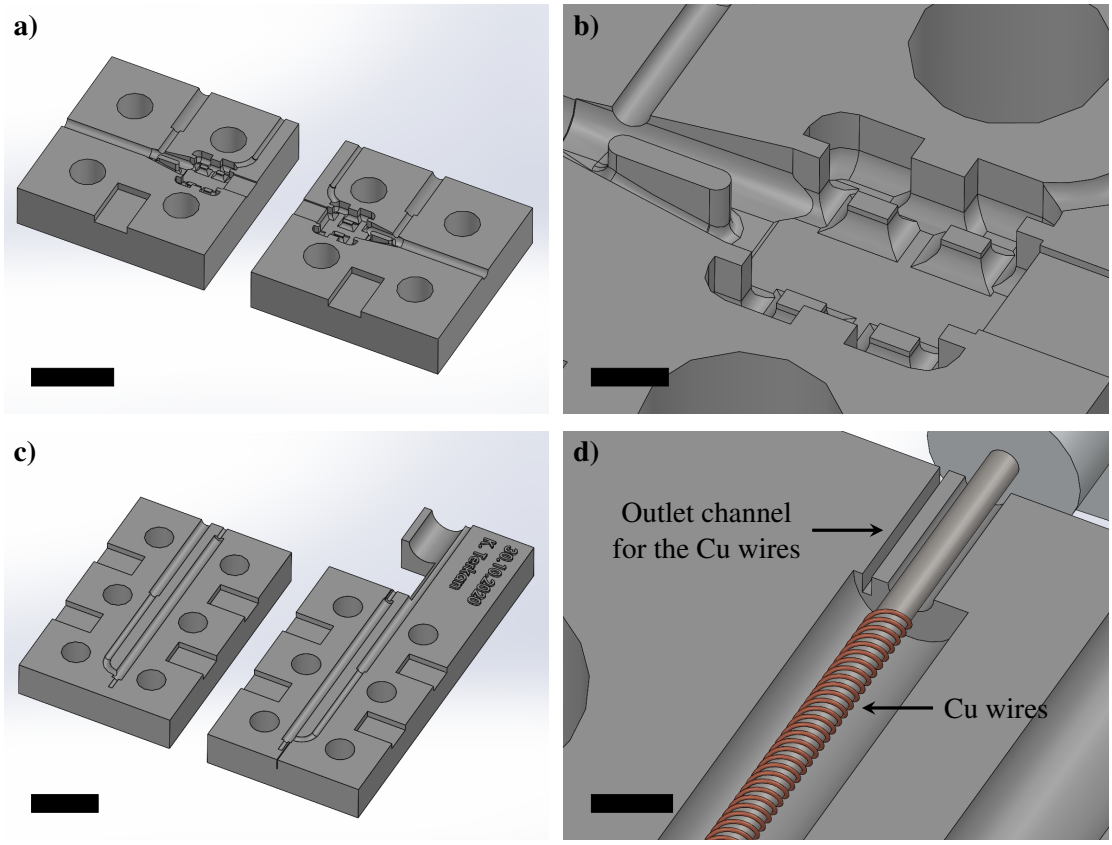

Figure 6: CAD drawing of the molds which were used to fabricate the silicone encapsulation for the electrical connection between the CNT conductors and the external electroncis. **a)** The mold for the Cu-CNT clip. Scale bar is $10\,\mathrm{mm}$. **b)** Zoomed view on the left mold half in a. Scale bar is $2\,\mathrm{mm}$. **c)** The mold for the spiralized Cu wire. Scale bar is $10\,\mathrm{mm}$. **d)** Zoomed view on the right mold half showing how the the spiralized Cu wires are held in the middle of the channel by a G27 needle. Scale bar is $1\,\mathrm{mm}$.

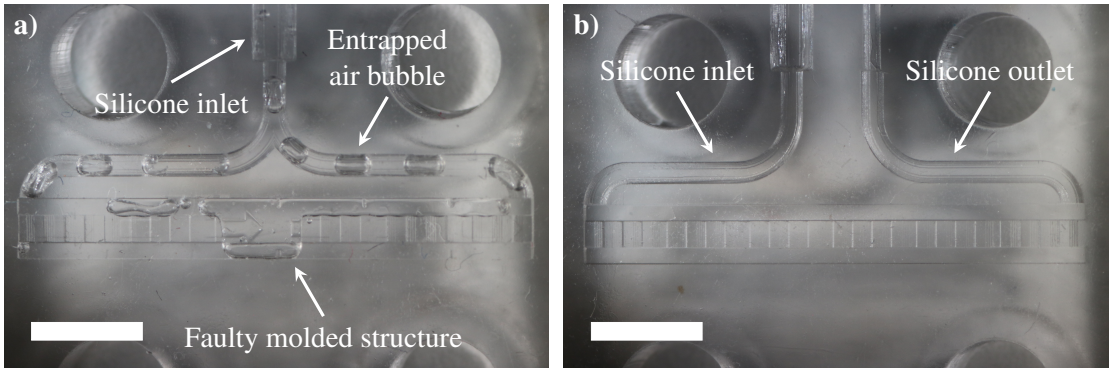

Figure 7: **a)** A faulty mold design where no outlet for the silicone is included. Due to entrapped air bubbles the injected silicone cannot fill the entire hollow volume inside the mold. This leads to a faulty molded structure. **b)** In order to avoid air bubbles inside the mold silicone outlets must be included in the design. Scale bars are $4\,\mathrm{mm}$.

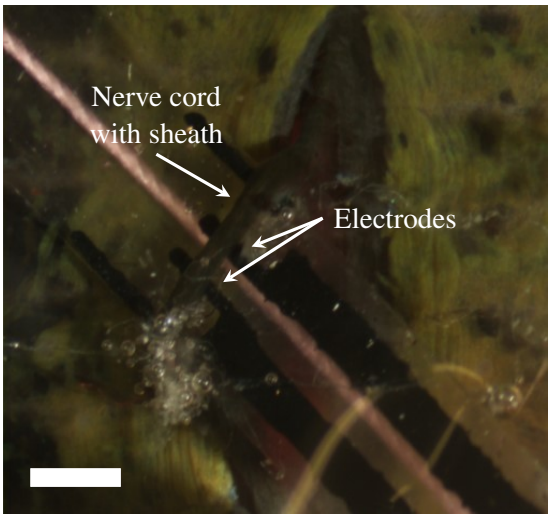

Figure 8: An interfacing experiment with a leech where the sheath wrapped around the nerve cord was not removed. In this experiment the nerve could not be stimulated due to the sheath. Scale bar is $1\,\mathrm{mm}$.

REFERENCES

[1] López-Muñoz, F., Boya, J. & Alamo, C. Neuron theory, the cornerstone of neuroscience, on the centenary of the Nobel Prize award to Santiago Ramón y Cajal. *Brain Research Bulletin* **70**, 391–405 (2006). URL https://www.sciencedirect.com/science/article/pii/S0361923006002334.

[2] Hodgkin, A. L. & Huxley, A. F. A quantitative description of membrane current and its application to conduction and excitation in nerve. *The Journal of Physiology* **117**, 500–544 (1952). URL https://onlinelibrary.wiley.com/doi/10.1113/jphysiol.1952.sp004764.

[3] Hodgkin, A. L., Huxley, A. F. & Katz, B. Measurement of current-voltage relations in the membrane of the giant axon of Loligo. *The Journal of Physiology* **116**, 424–448 (1952). URL http://www.ncbi.nlm.nih.gov/pmc/articles/PMC1392219/.

[4] Adrian, E. D. The Basis of Sensation. *British Medical Journal* **1**, 287–290 (1954). URL http://www.ncbi.nlm.nih.gov/pmc/articles/PMC2093300/.

[5] Frankenhaeuser, B. & Huxley, A. F. The action potential in the myelinated nerve fibre of *Xenopus laevis* as computed on the basis of voltage clamp data. *The Journal of Physiology* **171**, 302–315 (1964). URL http://doi.wiley.com/10.1113/jphysiol.1964.sp007378.

[6] Barrett, E. F. & Barrett, J. N. Intracellular recording from vertebrate myelinated axons: mechanism of the depolarizing afterpotential. *The Journal of Physiology* **323**, 117–144 (1982). URL http://doi.wiley.com/10.1113/jphysiol.1982.sp014064.

[7] Pine, J. Recording action potentials from cultured neurons with extracellular microcircuit electrodes. *Journal of Neuroscience Methods* **2**, 19–31 (1980).

[8] Gross, G. W., Rhoades, B. K., Azzazy, H. M. E. & Ming-Chi Wu. The use of neuronal networks on multielectrode arrays as biosensors. *Biosensors and Bioelectronics* **10**,

553–567 (1995). URL http://www.sciencedirect.com/science/article/pii/095656639596931N.

[9] Blau, A. *et al.* Characterization and optimization of microelectrode arrays for in vivo nerve signal recording and stimulation. *Biosensors & Bioelectronics* **12**, 883–892 (1997).

[10] Yeung, C. K. *et al.* Drug profiling using planar microelectrode arrays. *Analytical and Bioanalytical Chemistry* **387**, 2673–2680 (2007).

[11] Harding, S. E., Ali, N. N., Brito-Martins, M. & Gorelik, J. The human embryonic stem cell-derived cardiomyocyte as a pharmacological model. *Pharmacology & Therapeutics* **113**, 341–353 (2007).

[12] Wesche, M. *et al.* A nanoporous alumina microelectrode array for functional cell-chip coupling. *Nanotechnology* **23**, 495303 (2012).

[13] Schnitker, J., Afanasenkau, D., Wolfrum, B. & Offenhäusser, A. Planar reference electrodes on multielectrode arrays for electrochemical measurements of ionic currents. *physica status solidi (a)* **210**, 892–897 (2013). URL http://onlinelibrary.wiley.com/doi/10.1002/pssa.201200850/abstract.

[14] Thomas, C. A., Springer, P. A., Loeb, G. E., Berwald-Netter, Y. & Okun, L. M. A miniature microelectrode array to monitor the bioelectric activity of cultured cells. *Experimental Cell Research* **74**, 61–66 (1972). URL http://www.sciencedirect.com/science/article/pii/0014482772904818.

[15] Spira, M. E. & Hai, A. Multi-electrode array technologies for neuroscience and cardiology. *Nature Nanotechnology* **8**, 83–94 (2013). URL http://www.nature.com/nnano/journal/v8/n2/full/nnano.2012.265.html.

[16] Yakushenko, A., Schöps, V., Mayer, D., Offenhäusser, A. & Wolfrum, B. On-chip fast scan cyclic voltammetry for selective detection of redox active neurotransmitters. *physica status solidi (a)* **211**, 1364–1371 (2014). URL http://onlinelibrary.wiley.com/doi/10.1002/pssa.201330276/abstract.

[17] Ballini, M. *et al.* A 1024-Channel CMOS Microelectrode Array With 26,400 Electrodes for Recording and Stimulation of Electrogenic Cells In Vitro. *IEEE Journal of Solid-State Circuits* **49**, 2705–2719 (2014).

[18] Eversmann, B. *et al.* A 128 /spl times/ 128 CMOS bio-sensor array for extracellular recording of neural activity. In *2003 IEEE International Solid-State Circuits Conference, 2003. Digest of Technical Papers. ISSCC.*, 222–489 vol.1 (2003).

[19] Berdondini, L. *et al.* Active pixel sensor array for high spatio-temporal resolution electrophysiological recordings from single cell to large scale neuronal networks. *Lab on a Chip* **9**, 2644–2651 (2009).

[20] Dragas, J. *et al.* In Vitro Multi-Functional Microelectrode Array Featuring 59 760 Electrodes, 2048 Electrophysiology Channels, Stimulation, Impedance Measurement, and Neurotransmitter Detection Channels. *IEEE Journal of Solid-State Circuits* **52**, 1576–1590 (2017).

[21] Helm, S. *et al.* Peripheral Nerve Stimulation for Chronic Pain: A Systematic Review of Effectiveness and Safety. *Pain and Therapy* **10**, 985–1002 (2021). URL `https://link.springer.com/10.1007/s40122-021-00306-4`.

[22] Molina, R. *et al.* Report of a patient undergoing chronic responsive deep brain stimulation for Tourette syndrome: proof of concept. *Journal of Neurosurgery* **129**, 308–314 (2018). URL `https://thejns.org/view/journals/j-neurosurg/129/2/article-p308.xml`.

[23] Liu, Y. *et al.* Frequency Dependent Electrical Stimulation of PFC and ACC for Acute Pain Treatment in Rats. *Frontiers in Pain Research* **2**, 728045 (2021). URL `https://www.frontiersin.org/articles/10.3389/fpain.2021.728045/full`.

[24] Howland, R. H. Vagus Nerve Stimulation. *Current Behavioral Neuroscience Reports* **1**, 64–73 (2014). URL `http://link.springer.com/10.1007/s40473-014-0010-5`.

[25] Yildiz, K. A., Shin, A. Y. & Kaufman, K. R. Interfaces with the peripheral nervous system for the control of a neuroprosthetic limb: a review. *Journal of NeuroEngineering and Rehabilitation* **17**, 43 (2020). URL `https://jneuroengrehab.biomedcentral.com/articles/10.1186/s12984-020-00667-5`.

[26] Hochmair-Desoyer, I. J. & Hochmair, E. S. An Eight Channel Scala Tympani Electrode for Auditory Prostheses. *IEEE Transactions on Biomedical Engineering* **BME-27**, 44–50 (1980). URL `http://ieeexplore.ieee.org/document/4123125/`.

[27] Bloch, E., Luo, Y. & da Cruz, L. Advances in retinal prosthesis systems. *Therapeutic Advances in Ophthalmology* **11**, 251584141881750 (2019). URL `http://journals.sagepub.com/doi/10.1177/2515841418817501`.

[28] Mueller, A. H. *et al.* Laryngeal pacing for bilateral vocal fold paralysis: Voice and respiratory aspects: Voice and Respiratory Aspects of LP System. *The Laryngoscope* **127**, 1838–1844 (2017). URL http://doi.wiley.com/10.1002/lary.26428.

[29] Yan, D. *et al.* Ultracompliant Carbon Nanotube Direct Bladder Device. *Advanced Healthcare Materials* **8**, 1900477 (2019). URL https://onlinelibrary.wiley.com/doi/10.1002/adhm.201900477.

[30] Rowald, A. *et al.* Activity-dependent spinal cord neuromodulation rapidly restores trunk and leg motor functions after complete paralysis. *Nature Medicine* **28**, 260–271 (2022). URL https://www.nature.com/articles/s41591-021-01663-5.

[31] Eilenberg, M. F., Kuan, J.-Y. & Herr, H. Development and Evaluation of a Powered Artificial Gastrocnemius for Transtibial Amputee Gait. *Journal of Robotics* **2018**, 1–15 (2018). URL https://www.hindawi.com/journals/jr/2018/5951965/.

[32] Lempka, S. F., Miocinovic, S., Johnson, M. D., Vitek, J. L. & McIntyre, C. C. *In vivo* impedance spectroscopy of deep brain stimulation electrodes. *Journal of Neural Engineering* **6**, 046001 (2009). URL https://iopscience.iop.org/article/10.1088/1741-2560/6/4/046001.

[33] Wang, W. *et al.* Human motor cortical activity recorded with Micro-ECoG electrodes, during individual finger movements. In *2009 Annual International Conference of the IEEE Engineering in Medicine and Biology Society*, 586–589 (IEEE, Minneapolis, MN, 2009). URL http://ieeexplore.ieee.org/document/5333704/.

[34] Lee, Y. J., Kim, H.-J., Do, S. H., Kang, J. Y. & Lee, S. H. Characterization of nerve-cuff electrode interface for biocompatible and chronic stimulating application. *Sensors and Actuators B: Chemical* **237**, 924–934 (2016). URL https://linkinghub.elsevier.com/retrieve/pii/S0925400516310310.

[35] Ordonez, J. S. *et al.* Cuff electrodes for very small diameter nerves — Prototyping and first recordings in vivo. In *2014 36th Annual International Conference of the IEEE Engineering in Medicine and Biology Society*, 6846–6849 (IEEE, Chicago, IL, 2014). URL http://ieeexplore.ieee.org/document/6945201/.

[36] Xue, N. *et al.* Polymeric C-shaped cuff electrode for recording of peripheral nerve signal. *Sensors and Actuators B: Chemical* **210**, 640–648 (2015). URL https://linkinghub.elsevier.com/retrieve/pii/S0925400515000222.

[37] Schiefer, M. A., Polasek, K. H., Triolo, R. J., Pinault, G. C. J. & Tyler, D. J. Selective stimulation of the human femoral nerve with a flat interface nerve electrode. *Journal of Neural Engineering* **7**, 026006 (2010). URL https://iopscience.iop.org/article/10.1088/1741-2560/7/2/026006.

[38] Lawrence, S., Dhillon, G., Jensen, W., Yoshida, K. & Horch, K. Acute peripheral nerve recording Characteristics of polymer-based longitudinal intrafascicular electrodes. *IEEE Transactions on Neural Systems and Rehabilitation Engineering* **12**, 345–348 (2004). URL https://ieeexplore.ieee.org/document/1333050/.

[39] Kundu, A. *et al.* Stimulation Selectivity of the "Thin-Film Longitudinal Intrafascicular Electrode" (tfLIFE) and the "Transverse Intrafascicular Multi-Channel Electrode" (TIME) in the Large Nerve Animal Model. *IEEE Transactions on Neural Systems and Rehabilitation Engineering* **22**, 400–410 (2014). URL https://ieeexplore.ieee.org/document/6545380/.

[40] Boretius, T. *et al.* A transverse intrafascicular multichannel electrode (TIME) to interface with the peripheral nerve. *Biosensors and Bioelectronics* **26**, 62–69 (2010). URL https://linkinghub.elsevier.com/retrieve/pii/S0956566310002496.

[41] Badia, J., Raspopovic, S., Carpaneto, J., Micera, S. & Navarro, X. Spatial and Functional Selectivity of Peripheral Nerve Signal Recording With the Transversal Intrafascicular Multichannel Electrode (TIME). *IEEE Transactions on Neural Systems and Rehabilitation Engineering* **24**, 20–27 (2016). URL https://ieeexplore.ieee.org/document/7123655/.

[42] Jinwoo Jeong *et al.* 64-channel double-layered sieve electrode with increased porosity for improved axon regeneration and high spatial resolution. In *2016 6th IEEE International Conference on Biomedical Robotics and Biomechatronics (BioRob)*, 1148–1153 (IEEE, Singapore, Singapore, 2016). URL http://ieeexplore.ieee.org/document/7523786/.

[43] MacEwan, M. R., Zellmer, E. R., Wheeler, J. J., Burton, H. & Moran, D. W. Regenerated Sciatic Nerve Axons Stimulated through a Chronically Implanted Macro-Sieve Electrode. *Frontiers in Neuroscience* **10** (2016). URL http://journal.frontiersin.org/article/10.3389/fnins.2016.00557/full.

[44] Musick, K. M. *et al.* Chronic multichannel neural recordings from soft regenerative microchannel electrodes during gait. *Scientific Reports* **5**, 14363 (2015). URL http://www.nature.com/articles/srep14363.

[45] Srinivasan, A. *et al.* A regenerative microchannel device for recording multiple single-unit action potentials in awake, ambulatory animals. *European Journal of Neuroscience* **43**, 474–485 (2016). URL http://doi.wiley.com/10.1111/ejn.13080.

[46] Robblee, L. S. Activated Ir: An Electrode Suitable for Reversible Charge Injection in Saline Solution. *Journal of The Electrochemical Society* **130**, 731 (1983). URL https://iopscience.iop.org/article/10.1149/1.2119793.

[47] Kergoat, L. *et al.* PEDOT:PSS electrodes for acute experimental evaluation of vagus nerve stimulation on rodents. In *2018 40th Annual International Conference of the IEEE Engineering in Medicine and Biology Society (EMBC)*, 4760–4763 (2018).

[48] Foremny, K. *et al.* Carbon-Nanotube-Coated Surface Electrodes for Cortical Recordings In Vivo. *Nanomaterials* **11**, 1029 (2021). URL https://www.mdpi.com/2079-4991/11/4/1029.

[49] Boehler, C., Oberueber, F., Stieglitz, T. & Asplund, M. Nanostructured platinum as an electrochemically and mechanically stable electrode coating. In *2017 39th Annual International Conference of the IEEE Engineering in Medicine and Biology Society (EMBC)*, 1058–1061 (IEEE, Seogwipo, 2017). URL https://ieeexplore.ieee.org/document/8037009/.

[50] Weiland, J. & Anderson, D. Chronic neural stimulation with thin-film, iridium oxide electrodes. *IEEE Transactions on Biomedical Engineering* **47**, 911–918 (2000). URL http://ieeexplore.ieee.org/document/846685/.

[51] Merrill, D. R., Bikson, M. & Jefferys, J. G. R. Electrical stimulation of excitable tissue: design of efficacious and safe protocols. *Journal of Neuroscience Methods* **141**, 171–198 (2005). URL http://www.sciencedirect.com/science/article/pii/S0165027004003826.

[52] Cogan, S. F. Neural Stimulation and Recording Electrodes. *Annual Review of Biomedical Engineering* **10**, 275–309 (2008). URL https://doi.org/10.1146/annurev.bioeng.10.061807.160518.

[53] Khodagholy, D. *et al.* NeuroGrid: recording action potentials from the surface of the brain. *Nature Neuroscience* **18**, 310–315 (2015). URL http://www.nature.com/articles/nn.3905.

[54] Lacour, S. P., Courtine, G. & Guck, J. Materials and technologies for soft implantable neuroprostheses. *Nature Reviews Materials* **1**, 16063 (2016). URL http://www.nature.com/articles/natrevmats201663.

[55] Khodagholy, D. *et al.* In vivo recordings of brain activity using organic transistors. *Nature Communications* **4**, 1575 (2013). URL http://www.nature.com/articles/ncomms2573.

[56] Minev, I. R. *et al.* Electronic dura mater for long-term multimodal neural interfaces. *Science* **347**, 159–163 (2015). URL http://www.sciencemag.org/cgi/doi/10.1126/science.1260318.

[57] Adly, N. *et al.* Printed microelectrode arrays on soft materials: from PDMS to hydrogels. *npj Flexible Electronics* **2**, 15 (2018). URL https://doi.org/10.1038/s41528-018-0027-z.

[58] Decataldo, F. *et al.* Stretchable Low Impedance Electrodes for Bioelectronic Recording from Small Peripheral Nerves. *Scientific Reports* **9**, 1–9 (2019). URL https://www.nature.com/articles/s41598-019-46967-2.

[59] Gray, D., Tien, J. & Chen, C. High-Conductivity Elastomeric Electronics. *Advanced Materials* **16**, 393–397 (2004). URL http://doi.wiley.com/10.1002/adma.200306107.

[60] Guo, L., Ma, M., Zhang, N., Langer, R. & Anderson, D. G. Stretchable Polymeric Multielectrode Array for Conformal Neural Interfacing. *Advanced Materials* **26**, 1427–1433 (2014). URL http://doi.wiley.com/10.1002/adma.201304140.

[61] Lacour, S. P., Chan, D., Wagner, S., Li, T. & Suo, Z. Mechanisms of reversible stretchability of thin metal films on elastomeric substrates. *Applied Physics Letters* **88**, 204103 (2006). URL http://aip.scitation.org/doi/10.1063/1.2201874.

[62] Hu, C. *et al.* Inkjet Printing of Nanoporous Gold Electrode Arrays on Cellulose Membranes for High-Sensitive Paper-Like Electrochemical Oxygen Sensors Using Ionic Liquid Electrolytes. *Analytical Chemistry* **84**, 3745–3750 (2012). URL https://pubs.acs.org/doi/10.1021/ac3003243.

[63] Khan, Y. *et al.* Inkjet-Printed Flexible Gold Electrode Arrays for Bioelectronic Interfaces. *Advanced Functional Materials* **26**, 1004–1013 (2016). URL http://onlinelibrary.wiley.com/doi/10.1002/adfm.201503316/abstract.

[64] Roberts, T. *et al.* Flexible Inkjet-Printed Multielectrode Arrays for Neuromuscular Cartography. *Advanced Healthcare Materials* **5**, 1462–1470 (2016). URL https://onlinelibrary.wiley.com/doi/10.1002/adhm.201600108.

[65] Schnitker, J. *et al.* Rapid Prototyping of Ultralow-Cost, Inkjet-Printed Carbon Microelectrodes for Flexible Bioelectronic Devices. *Advanced Biosystems* **2**, 1700136 (2018). URL https://onlinelibrary.wiley.com/doi/10.1002/adbi.201700136.

[66] Grob, L. *et al.* Inkjet-Printed and Electroplated 3D Electrodes for Recording Extracellular Signals in Cell Culture. *Sensors* **21**, 3981 (2021). URL https://www.mdpi.com/1424-8220/21/12/3981.

[67] Tybrandt, K. *et al.* High-Density Stretchable Electrode Grids for Chronic Neural Recording. *Advanced Materials* **30**, 1706520 (2018). URL https://onlinelibrary.wiley.com/doi/abs/10.1002/adma.201706520.

[68] Lim, C., Min, D.-H. & Lee, S.-B. Direct patterning of carbon nanotube network devices by selective vacuum filtration. *Applied Physics Letters* **91**, 243117 (2007). URL http://aip.scitation.org/doi/10.1063/1.2824575.

[69] Hanein, Y. Carbon nanotube integration into MEMS devices. *physica status solidi (b)* **247**, 2635–2640 (2010). URL http://doi.wiley.com/10.1002/pssb.201000109.

[70] Nie, B. *et al.* Flexible and Transparent Strain Sensors with Embedded Multiwalled Carbon Nanotubes Meshes. *ACS Applied Materials & Interfaces* **9**, 40681–40689 (2017). URL http://pubs.acs.org/doi/10.1021/acsami.7b12987.

[71] Kim, J. H. *et al.* Simple and cost-effective method of highly conductive and elastic carbon nanotube/polydimethylsiloxane composite for wearable electronics. *Scientific Reports* **8**, 1375 (2018). URL http://www.nature.com/articles/s41598-017-18209-w.

[72] Luo, B. *et al.* Printing Carbon Nanotube-Embedded Silicone Elastomers via Direct Writing. *ACS Applied Materials & Interfaces* **10**, 44796–44802 (2018). URL http://pubs.acs.org/doi/10.1021/acsami.8b18614.

[73] Gabay, T. *et al.* Electro-chemical and biological properties of carbon nanotube based multi-electrode arrays. *Nanotechnology* **18**, 035201 (2007). URL http://stacks.iop.org/0957-4484/18/i=3/a=035201?key=crossref.3acdea8b19cce5afc7fb95a83458fc9b.

[74] Hanein, Y. & Bareket-Keren, L. Carbon nanotube-based multi electrode arrays for neuronal interfacing: progress and prospects. *Frontiers in Neural Circuits* **6** (2013). URL https://www.frontiersin.org/articles/10.3389/fncir.2012.00122/full.

[75] Tybrandt, K. & Vörös, J. Fast and Efficient Fabrication of Intrinsically Stretchable Multilayer Circuit Boards by Wax Pattern Assisted Filtration. *Small* **12**, 180–184 (2016). URL https://onlinelibrary.wiley.com/doi/abs/10.1002/smll.201502849.

[76] Hoath, S. D. *Fundamentals of Inkjet Printing: The Science of Inkjet and Droplets* (Wiley-VCH Verlag GmbH & Co. KGaA, Weinheim, 2016).

[77] Yang, H. S., Kang, B. J. & Oh, J. H. Control of Evaporation Behavior of an Inkjet-Printed Dielectric Layer Using a Mixed-Solvent System. *Journal of Electronic Materials* **45**, 755–763 (2016). URL https://link.springer.com/article/10.1007/s11664-015-4196-4.

[78] Sowade, E., Blaudeck, T. & Baumann, R. R. Inkjet Printing of Colloidal Nanospheres: Engineering the Evaporation-Driven Self-Assembly Process to Form Defined Layer Morphologies. *Nanoscale Research Letters* **10**, 362 (2015). URL https://nanoscalereslett.springeropen.com/articles/10.1186/s11671-015-1065-2.

[79] Zips, S. Signal Propagation along Cardiac Bio-Cables Guided by 3D-Printed Microstructures 81.

[80] Hornbeck, L. J. Digital Light Processing1M for High-Brightness, High-Resolution Applications 14.

[81] Ripperger, S., Gösele, W. & Alt, C. Filtration, 1. Fundamentals. In Wiley-VCH Verlag GmbH & Co. KGaA (ed.) *Ullmann's Encyclopedia of Industrial Chemistry*, b02_10.pub2 (Wiley-VCH Verlag GmbH & Co. KGaA, Weinheim, Germany, 2009). URL https://onlinelibrary.wiley.com/doi/10.1002/14356007.b02_10.pub2.

[82] Hamann, C. & Vielstich, W. *Elektrochemie* (Wiley, 1997). URL https://books.google.at/books?id=ccNrRwAACAAJ.

[83] Merrill, D. R., Bikson, M. & Jefferys, J. G. Electrical stimulation of excitable tissue: design of efficacious and safe protocols. *Journal of Neuroscience Methods* **141**, 171–198 (2005). URL https://linkinghub.elsevier.com/retrieve/pii/S0165027004003826.

[84] Helmholtz, H. Studien über electrische Grenzschichten. *Annalen der Physik und Chemie* **243**, 337–382 (1879). URL https://onlinelibrary.wiley.com/doi/10.1002/andp.18792430702.

[85] Gouy, M. Sur la constitution de la charge électrique à la surface d'un électrolyte. *Journal de Physique Théorique et Appliquée* **9**, 457–468 (1910). URL http://www.edpsciences.org/10.1051/jphystap:019100090045700.

[86] Chapman, D. L. LI. *A contribution to the theory of electrocapillarity*. *The London, Edinburgh, and Dublin Philosophical Magazine and Journal of Science* **25**, 475–481 (1913). URL https://www.tandfonline.com/doi/full/10.1080/14786440408634187.

[87] Stern, O. Zur theorie der elektrolytischen doppelschicht. *Zeitschrift für Elektrochemie und angewandte physikalische Chemie* **30**, 508–516 (1924). URL https://onlinelibrary.wiley.com/doi/abs/10.1002/bbpc.192400182. https://onlinelibrary.wiley.com/doi/pdf/10.1002/bbpc.192400182.

[88] Jackson, W. F. & Duling, B. R. Toxic effects of silver-silver chloride electrodes on vascular smooth muscle. *Circulation Research* **53**, 105–108 (1983). URL https://www.ahajournals.org/doi/10.1161/01.RES.53.1.105.

[89] van Dongen, M. & Serdijn, W. *Design of Efficient and Safe Neural Stimulators: A Multidisciplinary Approach*. Analog Circuits and Signal Processing (Springer International Publishing, 2016). URL https://books.google.at/books?id=KRXbjgEACAAJ.

[90] Rattay, F. Analysis of models for extracellular fiber stimulation. *IEEE Transactions on Biomedical Engineering* **36**, 676–682 (1989).

[91] Voigt, M. B. & Kral, A. Cathodic-leading pulses are more effective than anodic-leading pulses in intracortical microstimulation of the auditory cortex. *Journal of Neural Engineering* **16**, 036002 (2019). URL https://iopscience.iop.org/article/10.1088/1741-2552/ab0944.

[92] Hamann, C. & Vielstich, W. *Elektrochemie* (Wiley, 1997). URL https://books.google.at/books?id=ccNrRwAACAAJ.

[93] Benoudjit, A., Bader, M. M. & Wan Salim, W. W. A. Study of electropolymerized PEDOT:PSS transducers for application as electrochemical sensors in aqueous media. *Sensing and Bio-Sensing Research* **17**, 18–24 (2018). URL https://linkinghub.elsevier.com/retrieve/pii/S2214180417301332.

[94] Kohl, P. A. Electrodeposition of Gold. In Schlesinger, M. & Paunovic, M. (eds.) *Modern Electroplating*, 115–130 (John Wiley & Sons, Inc., Hoboken, NJ, USA, 2011). URL https://onlinelibrary.wiley.com/doi/10.1002/9780470602638.ch4.

[95] Blaus, B. Blausen 0657 multipolarneuron (2014). URL https://commons.wikimedia.org/wiki/File:Blausen_0657_MultipolarNeuron.png. Blausen.com staff (2014). "Medical gallery of Blausen Medical 2014". WikiJournal of Medicine 1 (2). DOI:10.15347/wjm/2014.010. ISSN 2002-4436. The file is licenced under the Creative Commons Attribution 3.0 Unported licence.

[96] McNeal, D. R. Analysis of a Model for Excitation of Myelinated Nerve. *IEEE Transactions on Biomedical Engineering* **BME-23**, 329–337 (1976). URL http://ieeexplore.ieee.org/document/4121058/.

[97] Iijima, S. Helical microtubes of graphitic carbon. *Nature* **356**, 55–58 (1991). URL https://www.nature.com/articles/354056a0#citeas.

[98] Zhang, R. *et al.* Growth of Half-Meter Long Carbon Nanotubes Based on Schulz–Flory Distribution. *ACS Nano* **7**, 6156–6161 (2013). URL https://pubs.acs.org/doi/10.1021/nn401995z.

[99] Laird, E. A. *et al.* Quantum transport in carbon nanotubes. *Reviews of Modern Physics* **87**, 703–764 (2015). URL https://link.aps.org/doi/10.1103/RevModPhys.87.703.

[100] Yu, M.-F. *et al.* Strength and Breaking Mechanism of Multiwalled Carbon Nanotubes Under Tensile Load. *Science* **287**, 637–640 (2000). URL https://www.science.org/doi/10.1126/science.287.5453.637.

[101] Berber, S., Kwon, Y.-K. & Tománek, D. Unusually High Thermal Conductivity of Carbon Nanotubes. *Physical Review Letters* **84**, 4613–4616 (2000). URL https://link.aps.org/doi/10.1103/PhysRevLett.84.4613.

[102] Banerjee, S., Kahn, M. G. C. & Wong, S. S. Rational Chemical Strategies for Carbon Nanotube Functionalization. *Chemistry - A European Journal* **9**, 1898–1908 (2003). URL https://onlinelibrary.wiley.com/doi/10.1002/chem.200204618.

[103] Ji, J. *et al.* Significant Improvement of Mechanical Properties Observed in Highly Aligned Carbon-Nanotube-Reinforced Nanofibers. *The Journal of Physical Chemistry C* **113**, 4779–4785 (2009). URL https://pubs.acs.org/doi/10.1021/jp8077198.

[104] Krause, B. *et al.* Comparison of nanotubes produced by fixed bed and aerosol-CVD methods and their electrical percolation behaviour in melt mixed polyamide 6.6 composites. *Composites Science and Technology* **70**, 151–160 (2010). URL https://linkinghub.elsevier.com/retrieve/pii/S0266353809003558.

[105] Kreupl, F. The carbon-nanotube computer has arrived. *Nature* **501**, 495–496 (2013). URL http://www.nature.com/articles/501495a.

[106] Chen, J. *et al.* Electrochemical characterization of carbon nanotubes as electrode in electrochemical double-layer capacitors. *Carbon* **40**, 1193–1197 (2002). URL https://linkinghub.elsevier.com/retrieve/pii/S0008622301002664.

[107] Rose, T. & Robblee, L. Electrical stimulation with Pt electrodes. VIII. Electrochemically safe charge injection limits with 0.2 ms pulses (neuronal application). *IEEE Transactions on Biomedical Engineering* **37**, 1118–1120 (1990). URL http://ieeexplore.ieee.org/document/61038/.

[108] Wang, K., Fishman, H. A., Dai, H. & Harris, J. S. Neural Stimulation with a Carbon Nanotube Microelectrode Array. *Nano Letters* **6**, 2043–2048 (2006). URL https://pubs.acs.org/doi/10.1021/nl061241t.

[109] Vitale, F., Summerson, S. R., Aazhang, B., Kemere, C. & Pasquali, M. Neural Stimulation and Recording with Bidirectional, Soft Carbon Nanotube Fiber Microelectrodes. *ACS Nano* **9**, 4465–4474 (2015). URL http://pubs.acs.org/doi/10.1021/acsnano.5b01060.

[110] Mattson, M. P., Haddon, R. C. & Rao, A. M. Molecular Functionalization of Carbon Nanotubes and Use as Substrates for Neuronal Growth. *Journal of Molecular Neuroscience* **14**, 175–182 (2000). URL http://link.springer.com/10.1385/JMN:14:3:175.

[111] Eatemadi, A. *et al.* Carbon nanotubes: properties, synthesis, purification, and medical applications. *Nanoscale Research Letters* **9**, 393 (2014). URL https://nanoscalereslett.springeropen.com/articles/10.1186/1556-276X-9-393.

[112] Alshehri, R. *et al.* Carbon Nanotubes in Biomedical Applications: Factors, Mechanisms, and Remedies of Toxicity: Miniperspective. *Journal of Medicinal Chemistry* **59**, 8149–8167 (2016). URL https://pubs.acs.org/doi/10.1021/acs.jmedchem.5b01770.

[113] Simon, J., Flahaut, E. & Golzio, M. Overview of Carbon Nanotubes for Biomedical Applications. *Materials* **12**, 624 (2019). URL http://www.mdpi.com/1996-1944/12/4/624.

[114] Lamberti, M. *et al.* Carbon nanotubes: Properties, biomedical applications, advantages and risks in patients and occupationally-exposed workers. *International Journal of Immunopathology and Pharmacology* **28**, 4–13 (2015). URL http://journals.sagepub.com/doi/10.1177/0394632015572559.

[115] Fiorito, S., Serafino, A., Andreola, F. & Bernier, P. Effects of fullerenes and single-wall carbon nanotubes on murine and human macrophages. *Carbon* **44**, 1100–1105 (2006). URL https://www.sciencedirect.com/science/article/pii/S0008622305006871.

[116] Smart, S. K., Cassady, A. I., Lu, G. Q. & Martin, D. J. The biocompatibility of carbon nanotubes. *Carbon* **44**, 1034–1047 (2006). URL https://www.sciencedirect.com/science/article/pii/S000862230500607X.

[117] Green, R. A., Lovell, N. H., Wallace, G. G. & Poole-Warren, L. A. Conducting polymers for neural interfaces: Challenges in developing an effective long-term implant. *Biomaterials* **29**, 3393–3399 (2008). URL https://linkinghub.elsevier.com/retrieve/pii/S0142961208003220.

[118] Wilks, S. Poly(3,4-ethylene dioxythiophene) (PEDOT) as a micro-neural interface material for electrostimulation. *Frontiers in Neuroengineering* **2** (2009). URL http://journal.frontiersin.org/article/10.3389/neuro.16.007.2009/abstract.

[119] Cui, X. & Zhou, D. Poly (3,4-Ethylenedioxythiophene) for Chronic Neural Stimulation. *IEEE Transactions on Neural Systems and Rehabilitation Engineering* **15**, 502–508 (2007). URL http://ieeexplore.ieee.org/document/4359235/.

[120] Kirchmeyer, S. & Reuter, K. Scientific importance, properties and growing applications of poly(3,4-ethylenedioxythiophene). *Journal of Materials Chemistry* **15**, 2077 (2005). URL http://xlink.rsc.org/?DOI=b417803n.

[121] Wang, Y. *et al.* A highly stretchable, transparent, and conductive polymer. *Science Advances* **3**, e1602076 (2017). URL https://advances.sciencemag.org/content/3/3/e1602076.

[122] Dijk, G., Rutz, A. L. & Malliaras, G. G. Stability of PEDOT:PSS-Coated Gold Electrodes in Cell Culture Conditions. *Advanced Materials Technologies* **5**, 1900662 (2020). URL https://onlinelibrary.wiley.com/doi/abs/10.1002/admt.201900662.

[123] Luo, X., Weaver, C. L., Zhou, D. D., Greenberg, R. & Cui, X. T. Highly stable carbon nanotube doped poly(3,4-ethylenedioxythiophene) for chronic neural stimulation. *Biomaterials* **32**, 5551–5557 (2011). URL https://linkinghub.elsevier.com/retrieve/pii/S014296121100473X.

[124] Decataldo, F. *et al.* Stretchable Low Impedance Electrodes for Bioelectronic Recording from Small Peripheral Nerves. *Scientific Reports* **9**, 10598 (2019). URL http://www.nature.com/articles/s41598-019-46967-2.

[125] Wu, J. *et al.* Inkjet-printed microelectrodes on PDMS as biosensors for functionalized microfluidic systems. *Lab on a Chip* **15**, 690–695 (2015). URL http://xlink.rsc.org/?DOI=C4LC01121J.

[126] Kim, J. H. *et al.* Simple and cost-effective method of highly conductive and elastic carbon nanotube/polydimethylsiloxane composite for wearable electronics. *Scientific Reports* **8**, 1375 (2018). URL http://www.nature.com/articles/s41598-017-18209-w.

[127] Grob, L. R. Printed 3D electrodes for sensing and bioelectronics 142.

[128] Byun, I., Coleman, A. W. & Kim, B. Transfer of thin Au films to polydimethylsiloxane (PDMS) with reliable bonding using (3-mercaptopropyl)trimethoxysilane (MPTMS) as a molecular adhesive. *J. Micromech. Microeng.* 12 (2013).

[129] Adly, N. Printed microelectrode arrays on soft materials: from PDMS to hydrogels. *npj Flexible Electronics* 9 (2018).

[130] Minev, I. R., Chew, D. J., Delivopoulos, E., Fawcett, J. W. & Lacour, S. P. Evaluation of an elastomer based gold microelectrode array for neural recording applications. In *2011 5th International IEEE/EMBS Conference on Neural Engineering*, 482–485 (IEEE, Cancun, 2011). URL http://ieeexplore.ieee.org/document/5910591/.

[131] Liang Guo *et al.* A PDMS-Based Integrated Stretchable Microelectrode Array (isMEA) for Neural and Muscular Surface Interfacing. *IEEE Transactions on Biomedical Circuits and Systems* **7**, 1–10 (2013). URL http://ieeexplore.ieee.org/document/6197244/.

[132] Jackson, W. F. & Duling, B. R. Toxic effects of silver-silver chloride electrodes on vascular smooth muscle. *Circulation Research* **53**, 105–108 (1983).

[133] Selvakumaran, J., Hughes, M., Keddie, J. & Ewins, D. Assessing biocompatibility of materials for implantable microelectrodes using cytotoxicity and protein adsorption studies.

In *2nd Annual International IEEE-EMBS Special Topic Conference on Microtechnologies in Medicine and Biology. Proceedings (Cat. No.02EX578)*, 261–264 (IEEE, Madison, WI, USA, 2002). URL http://ieeexplore.ieee.org/document/1002326/.

[134] Choi, Y.-J. & Luo, T.-J. M. Electrochemical Properties of Silver Nanoparticle Doped Aminosilica Nanocomposite. *International Journal of Electrochemistry* **2011**, 1–6 (2011). URL http://www.hindawi.com/journals/ijelc/2011/404937/.

[135] Jiang, Z.-j., Liu, C.-y. & Li, Y.-j. Electrochemical Studies of Silver Nanoparticles Tethered on Silica Sphere. *Chemistry Letters* **33**, 498–499 (2004). URL http://www.journal.csj.jp/doi/10.1246/cl.2004.498.

[136] Wu, Q. *et al.* Investigation of the foil structure and corrosion mechanisms of modern Zwischgold using advanced analysis techniques. *Journal of Cultural Heritage* **31**, 122–132 (2018). URL https://linkinghub.elsevier.com/retrieve/pii/S1296207417305538.

[137] Hwang, J. C. M., Pan, J. D. & Balluffi, R. W. Measurement of grain-boundary diffusion at low temperature by the surface-accumulation method. II. Results for gold-silver system. *Journal of Applied Physics* **50**, 1349–1359 (1979). URL http://aip.scitation.org/doi/10.1063/1.326115.

[138] Kirsch, R. G., Poate, J. M. & Eibschutz, M. Interdiffusion mechanisms in Ag-Au thin-film couples. *Applied Physics Letters* **29**, 772–775 (1976). URL http://aip.scitation.org/doi/10.1063/1.88944.

[139] Sekine, T., Fukuda, K., Kumaki, D. & Tokito, S. Enhanced adhesion mechanisms between printed nano-silver electrodes and underlying polymer layers. *Nanotechnology* **26**, 321001 (2015). URL https://iopscience.iop.org/article/10.1088/0957-4484/26/32/321001.

[140] Clark, G. M. The multiple-channel cochlear implant: the interface between sound and the central nervous system for hearing, speech, and language in deaf people—a personal perspective. *Philosophical Transactions of the Royal Society B: Biological Sciences* **361**, 791–810 (2006). URL https://royalsocietypublishing.org/doi/10.1098/rstb.2005.1782.

[141] Bachmann, B. *et al.* All-inkjet-printed gold microelectrode arrays for extracellular recording of action potentials. *Flexible and Printed Electronics* **2**, 035003 (2017). URL https://iopscience.iop.org/article/10.1088/2058-8585/aa7928.

[142] Jehn, J. *et al.* Fully Inkjet-Printed Carbon Nanotube-PDMS-Based Strain Sensor: Temperature Response, Compressive and Tensile Bending Properties, and Fatigue Investigations. *IEEE Access* **9**, 72207–72216 (2021). URL https://ieeexplore.ieee.org/document/9427226/.

[143] Afanasenkau, D. *et al.* Rapid prototyping of soft bioelectronic implants for use as neuromuscular interfaces. *Nature Biomedical Engineering* (2020). URL http://www.nature.com/articles/s41551-020-00615-7.

[144] Vitale, F., Summerson, S. R., Aazhang, B., Kemere, C. & Pasquali, M. Neural Stimulation and Recording with Bidirectional, Soft Carbon Nanotube Fiber Microelectrodes. *ACS Nano* **9**, 4465–4474 (2015). URL https://pubs.acs.org/doi/10.1021/acsnano.5b01060.

[145] Yeh, S.-R. *et al.* Interfacing Neurons both Extracellularly and Intracellularly Using Carbon-Nanotube Probes with Long-Term Endurance. *Langmuir* **25**, 7718–7724 (2009). URL https://pubs.acs.org/doi/10.1021/la900264x.

[146] Hu, C.-C., Su, J.-H. & Wen, T.-C. Modification of multi-walled carbon nanotubes for electric double-layer capacitors: Tube opening and surface functionalization. *Journal of Physics and Chemistry of Solids* **68**, 2353–2362 (2007). URL https://linkinghub.elsevier.com/retrieve/pii/S0022369707003502.

[147] Delivopoulos, E., Chew, D. J., Minev, I. R., Fawcett, J. W. & Lacour, S. P. Concurrent recordings of bladder afferents from multiple nerves using a microfabricated PDMS microchannel electrode array. *Lab on a Chip* **12**, 2540 (2012). URL http://xlink.rsc.org/?DOI=c2lc21277c.

[148] Apollo, N. V. *et al.* Soft, Flexible Freestanding Neural Stimulation and Recording Electrodes Fabricated from Reduced Graphene Oxide. *Advanced Functional Materials* **25**, 3551–3559 (2015). URL https://onlinelibrary.wiley.com/doi/abs/10.1002/adfm.201500110.

[149] Barisci, J. N., Wallace, G. G. & Baughman, R. H. Electrochemical Characterization of Single-Walled Carbon Nanotube Electrodes. *Journal of The Electrochemical Society* **147**, 4580 (2000). URL https://iopscience.iop.org/article/10.1149/1.1394104.

[150] David-Pur, M., Bareket-Keren, L., Beit-Yaakov, G., Raz-Prag, D. & Hanein, Y. All-carbon-nanotube flexible multi-electrode array for neuronal recording and stimulation.

Biomedical Microdevices **16**, 43–53 (2014). URL http://link.springer.com/10.1007/s10544-013-9804-6.

[151] Zhang, H., Cao, G., Yang, Y. & Gu, Z. Comparison Between Electrochemical Properties of Aligned Carbon Nanotube Array and Entangled Carbon Nanotube Electrodes. *Journal of The Electrochemical Society* **155**, K19 (2008). URL https://iopscience.iop.org/article/10.1149/1.2811864.

[152] Shepherd, R. K., Clark, G. M. & Black, R. C. Chronic Electrical Stimulation of the Auditory Nerve in Cats: Physiological and Histopathological Results. *Acta Oto-Laryngologica* **95**, 19–31 (1983). URL http://www.tandfonline.com/doi/full/10.3109/00016488309105589.

[153] Cogan, S. F., Ludwig, K. A., Welle, C. G. & Takmakov, P. Tissue damage thresholds during therapeutic electrical stimulation. *Journal of Neural Engineering* **13**, 021001 (2016). URL http://stacks.iop.org/1741-2552/13/i=2/a=021001?key=crossref.3e2d5a1dec26603d79d19f1b446dc21e.

[154] Noller, C. M., Levine, Y. A., Urakov, T. M., Aronson, J. P. & Nash, M. S. Vagus Nerve Stimulation in Rodent Models: An Overview of Technical Considerations. *Frontiers in Neuroscience* **13**, 911 (2019). URL https://www.frontiersin.org/article/10.3389/fnins.2019.00911/full.

[155] Bhide, A. A., Tailor, V., Fernando, R., Khullar, V. & Digesu, G. A. Posterior tibial nerve stimulation for overactive bladder—techniques and efficacy. *International Urogynecology Journal* **31**, 865–870 (2020). URL http://link.springer.com/10.1007/s00192-019-04186-3.

[156] Förster, G. *et al.* Laryngeal pacing in minipigs: in vivo test of a new minimal invasive transcricoidal electrode insertion method for functional electrical stimulation of the PCA. *European Archives of Oto-Rhino-Laryngology* **270**, 225–231 (2013). URL http://link.springer.com/10.1007/s00405-012-2141-1.

[157] Zurita, F. *et al.* In vivo closed-loop control of a locust's leg using nerve stimulation. *Scientific Reports* **12**, 10864 (2022). URL https://www.nature.com/articles/s41598-022-13679-z.

[158] Athanasiadis, M., Pak, A., Afanasenkau, D. & Minev, I. R. Direct Writing of Elastic Fibers with Optical, Electrical, and Microfluidic Functionality. *Advanced Materials Technologies* 1800659 (2019). URL http://doi.wiley.com/10.1002/admt.201800659.

[159] deHeer, W. A. *et al.* Aligned Carbon Nanotube Films: Production and Optical and Electronic Properties. *Science* **268**, 845–847 (1995). URL https://www.sciencemag.org/lookup/doi/10.1126/science.268.5212.845.

[160] Remillard, E. M. *et al.* Electric-field alignment of aqueous multi-walled carbon nanotubes on microporous substrates. *Carbon* **100**, 578–589 (2016). URL https://linkinghub.elsevier.com/retrieve/pii/S0008622316300240.

[161] He, X. *et al.* Wafer-scale monodomain films of spontaneously aligned single-walled carbon nanotubes. *Nature Nanotechnology* **11**, 633–638 (2016). URL http://www.nature.com/articles/nnano.2016.44.

ACKNOWLEDGEMENT

I would like to thank everybody who supported me during the time of my thesis. Especially I would like to thank

- Prof. Dr. Bernhard Wolfrum for giving me the possibility to work in this field of research. For his continuous disposability and his great mentoring. I also thank him for organizing the joyful nonacademic activities.
- Dr. Philipp Rinklin for his unique assistance with all his expertise. For giving an engineer the point of view of a scientist. I also thank him for the numerous interesting and amusing conversations.
- Dr. Tetsuhiko Teshima for conducting with me the rat experiments.
- Fransico Zurita for conducting with me the leech experiments.
- Heike Url for her assistance in the lab and Anja Kenn for her administrative support.
- Susanne Schnell-Witteczek, Dr.-Ing. Bernhard Gleich, and Josef Hintermair for their guidance at the Munich Institute of Biomedical Engineering.
- The Neuroelectronics group for the enjoyable time we had together.
- My family and my friends for all their support until today and for always believing in me.